AN ISOGEOMETRIC BOUNDARY ELEMENT FORMULATION FOR 2D FRETTING FATIGUE PROBLEMS

FERNANDO MORAIS DE LOYOLA

TESE DE DOUTORADO EM CIÊNCIAS MECÂNICAS
DEPARTAMENTO DE ENGENHARIA MECÂNICA

FACULDADE DE TECNOLOGIA
UNIVERSIDADE DE BRASÍLIA

UNIVERSIDADE DE BRASÍLIA
FACULDADE DE TECNOLOGIA
DEPARTAMENTO DE ENGENHARIA MECÂNICA

AN ISOGEOMETRIC BOUNDARY ELEMENT FORMULATION FOR 2D FRETTING FATIGUE PROBLEMS

FERNANDO MORAIS DE LOYOLA

Orientador: Prof. Éder Lima de Albuquerque, DSc. (ENM/Universidade de Brasília)

TESE DE DOUTORADO EM CIÊNCIAS MECÂNICAS

PUBLICAÇÃO PPGENM-TD XXX/2022
BRASÍLIA-DF, 27 DE JULHO DE 2022.

UNIVERSIDADE DE BRASÍLIA
FACULDADE DE TECNOLOGIA
DEPARTAMENTO DE ENGENHARIA MECÂNICA

AN ISOGEOMETRIC BOUNDARY ELEMENT FORMULATION FOR 2D FRETTING FATIGUE PROBLEMS

FERNANDO MORAIS DE LOYOLA

TESE DE DOUTORADO ACADÊMICO SUBMETIDA AO DEPARTAMENTO DE ENGENHARIA MECÂNICA DA FACULDADE DE TECNOLOGIA DA UNIVERSIDADE DE BRASÍLIA, COMO PARTE DOS REQUISITOS NECESSÁRIOS PARA A OBTENÇÃO DO GRAU DE DOUTOR EM ENGENHARIA MECÂNICA.

APROVADA POR:

Prof. Éder Lima de Albuquerque, DSc. (Universidade de Brasília - UnB, Brasil)
Orientador

Prof. Thiago de Carvalho Rodrigues Doca, PhD. (Universidade de Brasília - UnB, Brasil)
Examinador Interno

Prof. Edson Denner Leonel, DSc. (Escola de Engenharia de São Carlos - EESC/USP, Brasil)
Examinador Externo

Prof. Lucas Silveira Campos, DSc. (Universidade Federal do Espírito Santo - UFES, Brasil)
Examinador Externo

BRASÍLIA, 27 DE JULHO DE 2022.

FICHA CATALOGRÁFICA

FERNANDO MORAIS DE LOYOLA
An Isogeometric Boundary Element formulation for 2D fretting fatigue problems
[Distrito Federal] 2022.
x, XXp., 201x297 mm (ENM/FT/UnB, Doutor, Engenharia Mecânica, 2022)
Tese de Doutorado - Universidade de Brasília
Faculdade de Tecnologia
Departamento de Engenharia Mecânica

1. Boundary Elements Method 2. Isogeometric analysis
3. Fretting fatigue 4. Life estimation

I. ENM/FT/UnB II. DM XXX/XXX

REFERÊNCIA BIBLIOGRÁFICA

FERNANDO MORAIS DE LOYOLA (2022) An Isogeometric Boundary Element formulation for 2D fretting fatigue problems. Tese de Doutorado em Ciências Mecânicas, Publicação DM-XXX/2022, Departamento de Engenharia Mecânica, Universidade de Brasília, Brasília, DF, XXp.

CESSÃO DE DIREITOS

Fernando Morais de Loyola
f.loyola91@gmail.com

Acknowledgements

First of all, I would like to acknowledge the institution that funded this work. This study was financed in part by the Coordenação de Aperfeiçoamento de Pessoal de Nível Superior - Brasil (CAPES) - Finance Code 001.

I am extremely grateful to Prof. Éder Albuquerque for the invaluable supervision and the friendship built over the years. I also thank Prof. Jon Trevelyan for his guidance and for his insights, which were essential for this thesis. The assistance provided by Prof. Thiago Doca was greatly appreciated as well.

I wish to show my appreciation to my friends Luis Carlos and Giuliano for the good times spent together in Durham and for the ideas exchanged during lunch. Thanks also to my friends from UnB - Afonso, Lúcio, Álvaro, and Emerson -, for the support and for the chats after classes.

Words cannot express how grateful I am to my loving wife Raquel, who has always been by my side, especially during the tough moments. Thank you for being so patient and understanding.

Many thanks to my brother Fábio, who encouraged me throughout this time.

Finalmente, gostaria de agradecer aos meus pais, Socorro e José Alberto, por sempre me apoiarem e me incentivarem. É graças a vocês que isso foi possível.

Resumo

Esta tese propõe uma formulação do método dos elementos de contorno isogeométricos (IGABEM) para a solução de problemas bidimensionais elastostáticos e de contato. A área de aplicação são os cálculos de campos de tensões e de deslocamentos. A diferença entre as formulações isogeométrica e lagrangiana é que enquanto esta utiliza funções polinomais, aquela faz uso de funções splines racionais não-uniformes (NURBS), T-splines ou similares. Visando a facilitar a incorporação da formulação isogeométrica a códigos BEM existentes, a decomposição de Bézier é utilizada. Desta forma, as funções NURBS são decompostas em outras mais simples, que lembram as polinomais de Lagrange. Para os problemas de contato, utiliza-se a formulação nó-a-nó, tradicionalmente adotada na literatura para a definição dos modos de contato. O tratamento das singularidades nas integrais é feita por meio da transformada de Telles e pela Técnica de Subtração da Singularidade (SST) para singularidades fracas e fortes, respectivamente. Já a colocação é feita de acordo com as coordenadas de Greville, por serem mais adequadas à formulação isogeométrica. O IGABEM possui resultados mais precisos em relação ao BEM padrão por modelar sem aproximações geometrias complexas, as quais são apenas aproximadas por funções polinomiais. Os resultados obtidos corroboram essa hipótese, já que o IGABEM é consistentemente mais preciso do que o BEM padrão considerando o mesmo número de graus de liberdade. São comparados os resultados obtidos e os presentes na literatura, mostrando boa concordância. O IGABEM necessita de mais tempo de processamento para rodar o mesmo problema, como era esperado devido às curvas NURBS serem mais caras computacionalmente do que os polinômios de Lagrange. O BEM também é comparado com NTS-FEM, STS-FEM e DMT-FEM para estimativa de vida à fadiga. Primeiramente, o histórico de tensões ao longo de um ciclo de carregamento é computado por cada um dos métodos. Em seguida, utiliza-se um método de plano crítico para obter a amplitude de tensão cisalhante e a máxima tensão normal. Finalmente, o critério de falha de Fatemi-Socie é utilizado para estimar a vida à fadiga.

Palavras-chave: Método dos Elementos de Contorno, Análise Isogeométrica, NURBS, Fadiga por fretting, Estimativa de vida

Abstract

This thesis presents an Isogeometric Boundary Elements formulation (IGABEM) for solving bidimensional elastostatics and contact problems. It is applied to the calculation of the stresses and displacements fields. The difference between isogeometric and lagrangian formulations is that while the latter uses polynomial functions, the former uses nonuniform rational B-splines (NURBS), T-splines or similar. Aiming to facilitate the implementation of the isogeometric formulation to existing BEM codes, the Bézier decomposition is used. In this way, NURBS are decomposed in simpler basis functions, which resembles lagrangian polynomials. For the contact problems, a node-to-node formulation is adopted, which is a traditional technique in the literature for defining the contact modes. When it comes to treating the singularities, Telles transformation and Singularity Subtraction Technique (SST) are used for weak and strong singularities, respectively. Collocation, in turn, is made according to Greville's abscissae, for they are a better fit to isogeometric. IGABEM has more acurate results when compared to standard BEM because the former is able to exactly describe complex geometries, which are only approximated by polynomial functions. The results corroborate this hypothesis, since IGABEM is consistently more accurate than standard BEM considering the same number of degrees of freedom. The obtained results are compared to those available in the literature, showing good agreement. IGABEM requires more processor time for running the same problem, as it was expected due to NURBS being more costly than Lagrangian polynomials. BEM is also compared to NTS-FEM, STS-FEM, and DMT-FEM for fatigue life estimation. Firstly, the stress history during a complete loading cycle is computed by each framework. Then, a critical plane approach is used to obtain the shear stress amplitude and the maximum normal stress. Lastly, the Fatemi-Socie criterion of failure is used for estimating fatigue life.

Keywords: Boundary Elements Method, Isogeometric analysis, NURBS, Fretting fatigue, Life estimation

Contents

List of Figures

List of Tables

List of Symbols

Γ	Boundary of a domain Ω
γ	Transversal strain
ξ	Coordinate in parameter space
ε	Strain tensor
δ	Kronecker's delta
Δ	Dirac's delta
Ω	Domain
σ	Cauchy stress tensor
τ	Shear stress
γ	Strain
λ	Lamé constant
ν	Poisson's ratio
μ	Modulus of rigidity
$\Phi(z)$	Muskhelishvili's potential
$\Phi'(z)$	Derivative of Muskhelishvili's potential
$\bar{\Phi}(z)$	Conjugate of Muskhelishvili's potential
a	Contact semi-width
b	Body forces
B	Control points
c	Stick zone semi-width
d	Degree of curve
e	Offset of the centre stick zone
E	Transformation matrix;Young's modulus

f	Friction coefficient
J	Jacobian; Bernstein basis
m	Number of knots
n	Normal; order
N	Basis function
p	Point within domain
p_0	Peak contact pressure
p_N	Contact pressure
Q	Tangential force
P	Normal force
t_t	Tangential traction
t_n	Normal traction
u_t	Tangential displacement
u_n	Normal displacement
N_f	Number of cycles to failure
$\sigma_{n,max}$	Maximum normal stress
τa	Shear stress amplitude
L	Critical distance
L_σ	Uniaxial critical distance
L_τ	Torsional critical distance
L_{eq}	Equivalent critical distance
N_{est}	Estimated number of cycles to failure

Abbreviations

BEM	Boundary Elements Method
FEM	Finite Elements Method
IGA	Isogeometric analysis
DOF	Degrees of freedom
ACA	Adaptive cross approximation
FMM	Fast multipole method
IGABEM	Isogeometric Boundary Elements Method
NURBS	Non-uniform Rational B-Spline
SWT	Smith-Watson-Topper criterion
CPM	Critical plane method
FS	Fatemi-Socie criterion
CAD	Computer-aided design
IGAFEM	Isogeometric Finite Elements Method
KTS	knot-to-surface
STS	surface-to-surface
CPU	Central processing unit

1 Introduction

1.1 General Considerations

Developing reliable and cost-effective models for analysing engineering problems is an area of great interest to researchers. It is also stimulated by companies, especially with the increasing complexity of mechanical, aerospace, and automotive industries, in which parts are required to be lightweight without compromising high performance. For this reason, studying failure prediction models is essential for creating safe and advanced structures. Several engineering problems involve contact of mechanical components; this phenomenon can be crucial for determining the characteristics and resistance of a given part.

Fretting fatigue is a phenomenon that occurs at the contact interface of a restrained structural component that is subjected to vibratory excitations or oscillatory tangential forces. This kind of damage process involves wear, corrosion and fatigue driven by both the micro-slip at the contact surface and cyclic fretting contact stresses [1]. The micro-slip generates surface damage at a microscopic level, creating cracks in the early life of a component. In the presence of cyclic remote stress, these cracks may propagate and eventually lead to catastrophic failure [2]. One major difference between fretting contact and sliding contact is that the applied tangential load on the former phenomenon is not enough to create a global relative motion of the surfaces. Thus, it is possible to identify two regions of the contact area - one with a relative motion (micro-slip) and the other with no relative motion (stick). The fretting of, e.g., steel or aluminium, can be divided into three stages. First, the wearing process removes the thin oxide layer which covers the surface. Then the oxide layer is degraded and the underlying metal begins to adhere, forming a cold weld. Additionally, the process of adhesion accumulates a portion of wear debris between the contact surfaces, which can increase the friction coefficient. Finally, as the fretting cycles continue, near-surface plastic deformation arises and leads to microcracks nucleation.

Some examples where the contact is present are gearing, transmission using pulleys [3–5], bolted

and fastened joints [6–8], dovetail joints [9–11], parts with relative movement like pistons [12–14], overhead transmission cables [15–18], and human prosthetic devices [19–21]. Figures 1.1a, 1.1b and 1.1 show some of the applications of fretting fatigue analysis.

a) An overhead power line.

b) A clamped power cable [22].

c) A fir-tree (or Christmas-tree) joint in a turbine. Modified from [23]

d) Bladed disk dovetail attachment region and its associated damage [24].

Figure 1.1 Applications.

Plain fatigue was originally studied by Wöhler [25, 26] who investigated railway axle failures. His studies in this area, which spanned over two decades, were the first systematic investigation of S-N curves, which later became known as Wöhler curves. Eden et al. [27] in their various experiments on rotating beams, reported an oxide originated by mechanical means. Then, Tomlinson [28], with his article entitled "The Rusting of Steel Surfaces in Contact", made experiments where a plane surface and a spherical surface were in relative motion. He observed a red iron oxide and used the term 'fretting corrosion' for the first time. Warlow-Davies [29] discussed fretting corrosion and the possibility of its effect on fatigue strength. In his studies with medium-carbon-steel and nickel-chromium-molybdenum

alloy steel, he showed a reduction of fatigue strength of 13% and 18% after severe fretting, respectively.

Later investigations by [30] showed that fretting and fatigue acting together could produce strength reducing factors (SRFs) of 2-5. In 1958, Fenner and Field [31] showed that the crack nucleation process is highly accelerated by fretting. In plain fatigue, the stage of crack nucleation would take most of the fatigue life (90%), while in fretting it would take only 5%.

Johnson [32] performed an experimental investigation of micro-displacement between elastically loaded bodies under tangential forces. He was initially unaware of articles by Cattaneo [33] and Mindlin [34], and gladly found out that his results fitted the predicted curves by Mindlin [34]. Waterhouse [35] studied the impact of the friction coefficient between contact surfaces, the effect of frequency cyclic stressing, and the required cycles for crack initiation and propagation. Later, Waterhouse also analysed Hertzian contact under partial slip [36].

Nowell and Hills also made various contributions to contact and fretting, which they compiled into two books [37, 38]. They cover contacts under partial slip, the influence of surface treatments on fretting fatigue, and analysis of crack initiation and propagation. Araújo [39] focused on the initiation and arrest of fretting fatigue cracks. He conducted several studies since.

All this research, combined with advances in numerical methods, has enabled the study of more complex fretting fatigue problems. Petiot et al. [40] used Finite Elements Method (FEM) for determining the stress field before utilising Dang [41] multiaxial fatigue criterion to predict crack nucleation. It describes the loading path using shear stress and hydrostatic tension. Then, the path is compared to a material line, determined via tension and bending tests. Based on [40], Szolwinski and Farris [1] modified the Smith-Watson-Topper criterion (SWT) to predict fatigue life in terms of number of cycles to failure. Araújo [39] used the Critical plane method (CPM) and compared SWT and Fatemi-Socie criterion (FS).

Determining the stress field evolution within a fretting cycle is essential to the evaluation of fatigue resistance. Analysis of stress and strain due to external loads or interference as in the case of contact can be carried out in several ways. On the one hand, analytical techniques and models are extremely important in this context, as they enable a prompt response to the magnitudes involved in the problem. On the other hand, they are limited to very specific situations and geometries. For more complex situations and the validation of analytical and numerical models, it is possible to carry out experimental tests. Although very important, they require complex equipment, incur in high cost of execution, and

do not easily reproduce loads and geometries of specific parts.

Numerical analysis is an important tool for complex problems and provides the advantage of neither being so costly as experimental tests nor so limited as analytical solutions. Several techniques are currently employed, among which stand out the FEM, Meshless methods, and the Boundary Elements Method (BEM). The numerical analysis approach's advantages are that there is no limitation neither on geometry nor on loads and the possibility of simulating components with any shape. Yet, application of these techniques is limited by the development of models and computational power requirements.

As previously mentioned, one of the most used methods for analysis of contact problems is the FEM, which is used in commercial software such as Ansys and Abaqus. It is a domain technique, i.e., the entire domain of the problem must be discretized, leading to a considerable requirement of available memory for processing. In contrast, BEM is a technique that is growing in popularity and use and provides specific advantages that can be decisive for this application. The main feature of BEM is that only the boundary of the problem needs to be discretised. Through Green's second identity, the order of the problem is reduced. When it comes to the isogeometric formulation, BEM is highly indicated precisely because it has only the discretized boundary, which greatly facilitates the application of this method in relation to FEM. Also, for contact problems, the formulation is advantageous as it relates to a surface (boundary), since the contact occurs on the contour. Surface forces are also naturally present in the formulation, facilitating the contact analysis. Yet, one main disadvantage of BEM is that, unlike finite elements, the matrix representing the resulting linear system is full and non-symmetric, therefore increasing the computational cost. This disadvantage can though be minimized by the use of so-called fast methods, such as Fast multipole method (FMM) [42–45], Adaptive cross approximation (ACA) [46–50] and kernel interpolation [44].

BEM is widely used for many applications in engineering such as: crack growth [51], fatigue [52], acoustics [53], and geotechnics [54, 55], just to mention a few. These are evidence of the method's versatility.

Since the concept of Isogeometric analysis (IGA) was introduced by [56], it has received attention from many researchers due to its capacity to improve the established analysis process. Among other contributions, IGA decreases the amount of user's work, as the most time-consuming step – mesh generation – is reduced or even eliminated. To evidence isogeometric analysis advantages over lagrangian, they are compared in this study.

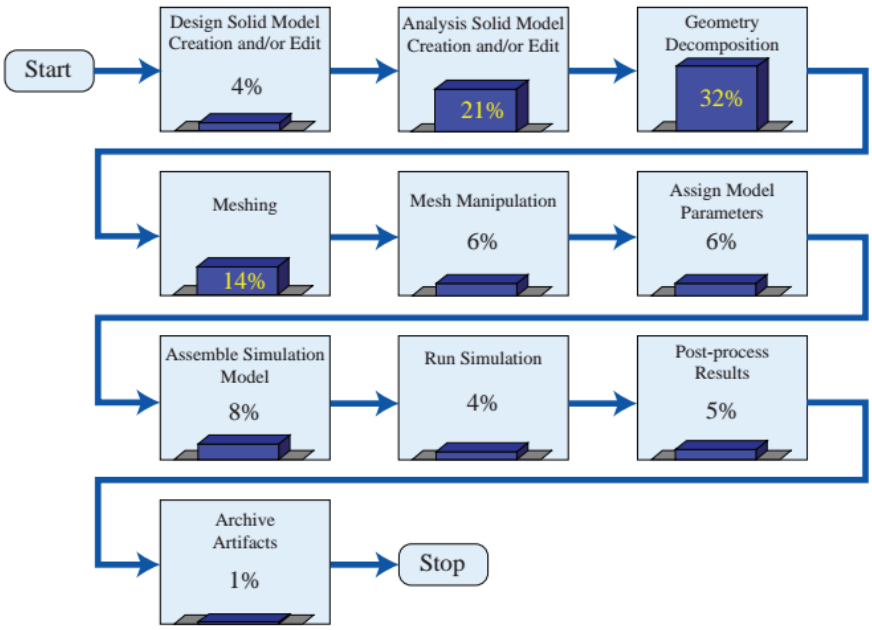

Figure 1.2 User's time consumption on each stage of the design process [57].

Four years after their introductory work, [57] published another book about IGA. Instead of using polynomial functions to discretise geometry and unknown fields, this novel method uses the same basis as Computer-aided design (CAD) software. CAD mostly uses Non-uniform Rational B-Spline (NURBS), which exactly describes the complex geometries that can only be approximated using polynomials. Although initially presented with FEM as in [57], Isogeometric Boundary Elements Method (IGABEM) for elastostatics was later developed in [58], and [59], with NURBS used to approximate the geometry along with the displacement and traction fields around the boundary. Works such as [60], and [61] already used B-splines as basis functions in BEM, however with no concern about integrating with CAD.

Take, for instance, the case of Sandia National Laboratories. Figure 1.2 shows a flowchart of the design process and the time consumed on each step from model creation on CAD software to the final results after analysis. It is noteworthy that three phases consume approximately 67% of the user's time: *creation and/or edit of analysis solid model, geometry decomposition*, and *meshing*. Working on these bottlenecks to enhance the process is the idea behind IGA in general and this thesis aims to apply it to contact mechanics.

Contact mechanics has been modelled using Isogeometric Finite Elements Method (IGAFEM) with different approaches. [62] , [63], and [64], use a knot-to-surface (KTS) or surface-to-surface (STS) approach. Other applications of IGA are shells [65–68].

More recent studies use IGABEM in acoustics [69], potential [70], structural optimization [71, 72], and reinforced structures [73]. [74] use IGABEM with Bézier decomposition for solving crack propagation problems. This study also uses IGABEM with Bézier decomposition to facilitate incorporating NURBS into existing boundary element codes for solving elastic and contact problems.

1.2 Motivation and objectives

As previously said, fretting fatigue is a failure process observed in many situations. As it is so ubiquitous, it represents a significant part of a country's gross national product Reed et al. [75]. Not only financial, but also social costs are involved with fretting. Jet turbines frequently use dovetail joints, which are subjected to fretting fatigue. Those engines are mainstream aviation propulsion for both civilian and military applications. According to an USAF research [76], fretting fatigue is one of the costliest sources of damage related to high cycle fatigue. Therefore, an efficient tool for analysing it is essential and deserves research and investigation.

Another interesting application are overhead cables. Power outage related to a broken cable is cause of both economic and social losses. For instance, on 30 April 2004, a broken line between Brasília and Marajoara (in Brazil's central area) resulted in a blackout that left about 636.700 inhabitants without electricity for 33 hours. Further studies revealed that the failure in a CELG 138 kV overhead line occurred in the fixation point of the clamp [77]. Adequate design of transmission equipment, cables, and other related structures play a major role in increasing the reliability of power delivery. Methods that facilitate the design process and increase its reliability and reduce the design time are always welcome.

The main objective of this thesis is the development and implementation of isogeometric boundary elements for elastostatics and fretting fatigue problems. A comparison between the proposed method and others is made as well. Regarding the novelty and main contributions of this study, the main points are:

- IGABEM was applied to contact of solids, but in a simpler problem [78]. They present an example with normal load only and with no friction. In the present thesis, a complete fretting simulation with shear and bulk loads is presented.

- Bézier extraction is used for representing NURBS. It facilitates incorporating NURBS to bound-

ary elements codes.

- BEM and IGABEM are compared for fretting problems.
- The stress history for a complete loading cycle is computed and used for shear stress amplitude and maximum normal stress determination.

1.3 Methodology

The first part of this work presents a formulation for isogeometric boundary elements, which is applied to elastostatics problems with analytical solutions. Then, IGABEM and BEM codes are implemented in Julia and Matlab, respectively. After validating both numerical methods with analytical solutions, the code is extended to contact and fretting situations.

For fretting problems, tractions, displacements, and stresses at internal points are computed using both codes and stored. Afterwards, the stress history is used as input into another Matlab code that, using CPM, obtains the shear stress amplitude and the maximum normal stress. Lastly, FS criterion is employed to estimate the fatigue life.

1.4 Outline

This study presents an isogeometric boundary element formulation for solving elastic and fretting fatigue problems. In order to decrease computational time and to make implementation easier in existing boundary element codes, NURBS are transformed into Bézier curves (Bézier decomposition). Thus, each Bézier curve can be viewed as a boundary element in a conventional boundary element implementation. The present work is divided as follows:

- Chapter 1 briefly describes the study, its objectives, and its motivation.
- Chapter 2 introduces concepts about elasticity.
- Chapter 3 focus on contact mechanics history and theory.
- Chapter 4 fretting fatigue and life estimation methods.
- Chapter 5 delineates the derivation of integral equation formulation.

- Chapter 6 presents the mathematical background of Bézier curves, B-splines and NURBS. It also explains the Bézier decomposition.
- Chapter 7 deals with the isogeometric analysis and its implementation in the boundary element context.
- Chapter 8 details the numerical modelling of contact problems using the isogeometric boundary element method.
- Chapter 9 shows the results and compares them with other methods.
- Chapter 10 presents the conclusion and final remarks of this study.

2 Elasticity Theory

Boundary Integral Equation (BIE) in elastostatics had its early days with [79], [80] and [81]. Though the fundamentals were developed, it was not until [82] and [83] that numerical formulations appeared. Noteworthy contributions such as linear variation over elements was made by [84] and [85], while isoparametric was presented by [86] and [87]. This chapter presents a brief description of necessary concepts used throughout this study.

2.1 Basic concepts

2.1.1 Stress

Consider an arbitrary shaped body, as in Fig. 2.1a, which is in equilibrium under external loads $P_1, P_2, ..., P_n$. Assuming the body is deformable, the forces are transmitted through its volume. If we take an internal point O, there is a resulting force δP, as the body is in equilibrium. Analysing a small area δA, it is reasonable to assume that δP is uniformly distributed over it.

In other words, stress is a measure of internal forces which acts within a body. They are a response to external loads applied to the body. Often, we write the force in terms of its normal and tangential components, δP_n and δP_s, respectively. Therefore, it is also possible to define the associated *normal stress* σ and the *shear stress* τ as:

$$\sigma = \lim_{\delta A \to 0} \left(\frac{\delta P_n}{\delta A} \right) = \frac{dP_n}{dA} \tag{2.1}$$

and

$$\tau = \lim_{\delta A \to 0} \left(\frac{\delta P_s}{\delta A} \right) = \frac{dP_s}{dA}. \tag{2.2}$$

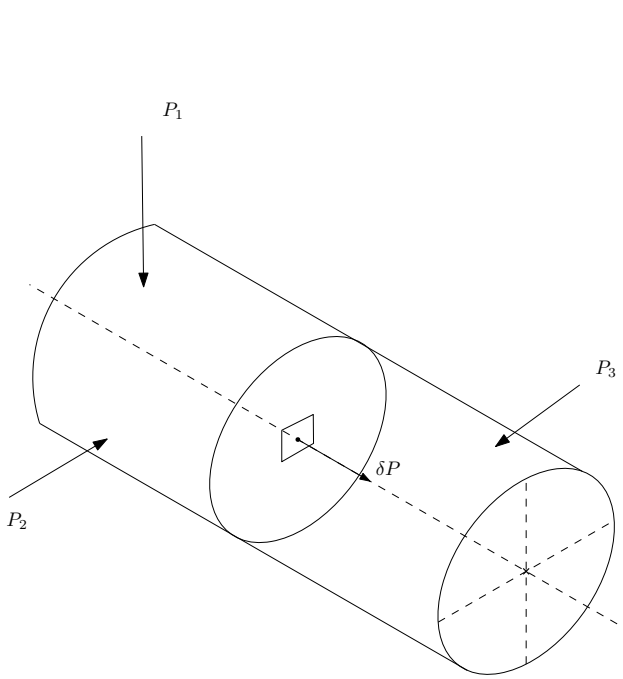

a) Internal forces at a point.

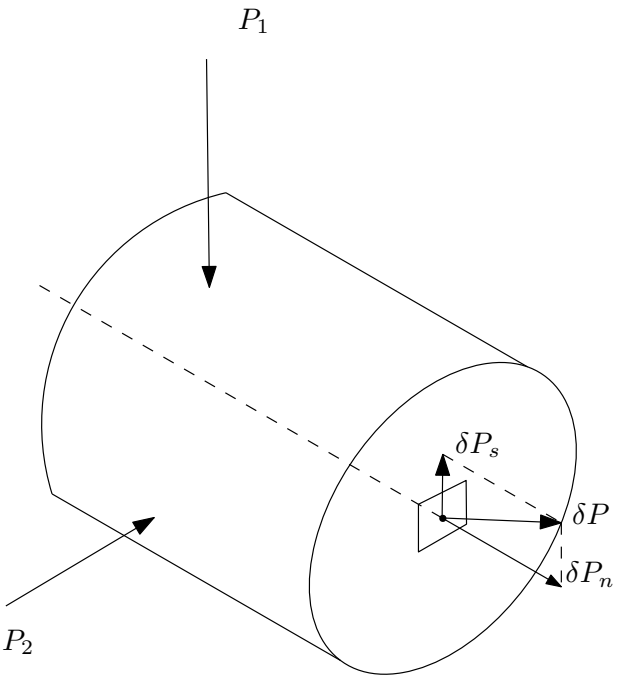

b) Internal forces at a point.

Figure 2.1 Internal forces at a point.

2.1.2 Equilibrium

Consider an infinitesimal cube of material of the body, as in Figure 2.2. It is possible to describe the state of stress at a point *O* by stress components formed on the sides of this cube.

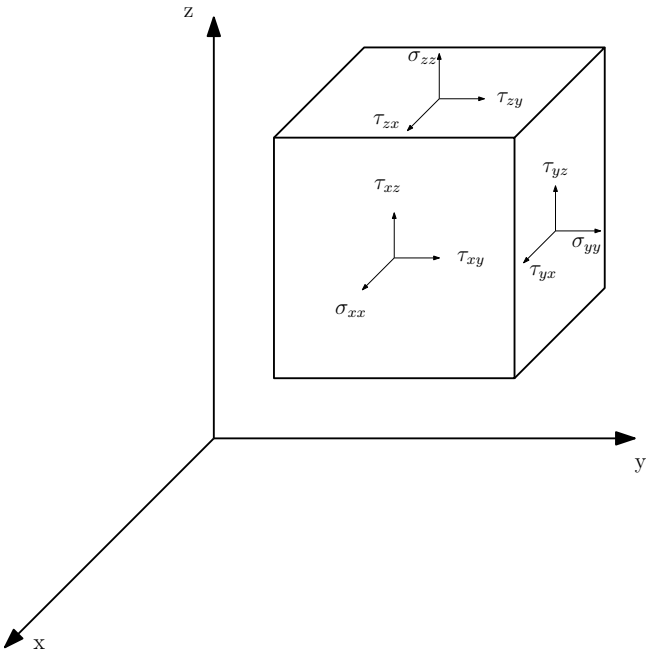

Figure 2.2 Stress in coordinate planes.

Total stress on each face of the planes has three components: one normal, and two tangential. Take,

for example, the face in yz plane. σ_{xx}, a component in the x direction, is a normal component. Both τ_{xy} and τ_{xz}, components in the y direction, are tangential components.

Stress is represented by nine quantities, with three components in each one of the three coordinate faces. Components σ_{xx}, σ_{yy} and σ_{zz} are normal stresses, while the remaining are tangential. Stresses are not as simple to describe as temperature, which is a scalar. They need a tensor in order to be represented, σ_{ij}, in which i and j may be x, y, z. The first index refers to the direction of the normal to the plane. The second describes the direction of the stress component.

Using equilibrium and taking moments with relation to the edges of cube, it is proved that:

$$\sigma_{ij} = \sigma_{ji} \tag{2.3}$$

which means that stress tensor is symmetric, i.e.:

$$\sigma_{ij} = \begin{bmatrix} \sigma_{xx} & \tau_{xy} & \tau_{xz} \\ \tau_{yx} & \sigma_{yy} & \tau_{yz} \\ \tau_{zx} & \tau_{zy} & \sigma_{zz} \end{bmatrix} = \begin{bmatrix} \sigma_{xx} & \tau_{yx} & \tau_{zx} \\ \tau_{xy} & \sigma_{yy} & \tau_{zy} \\ \tau_{xz} & \tau_{yz} & \sigma_{zz} \end{bmatrix}. \tag{2.4}$$

The equations of equilibrium for the three-dimensional system subjected to external forces and body forces b_x, b_y and b_z are given by:

$$\begin{aligned} \frac{\partial \sigma_{xx}}{\partial x} + \frac{\partial \tau_{xy}}{\partial y} + \frac{\partial \tau_{xz}}{\partial z} + b_x = 0, \\ \frac{\partial \tau_{yx}}{\partial x} + \frac{\partial \sigma_{yy}}{\partial y} + \frac{\partial \tau_{yz}}{\partial z} + b_y = 0, \\ \frac{\partial \tau_{zx}}{\partial x} + \frac{\partial \tau_{zy}}{\partial y} + \frac{\partial \sigma_{zz}}{\partial z} + b_z = 0, \end{aligned} \tag{2.5}$$

or using tensor notation for making it more compact:

$$\sigma_{ij,j} + b_i = 0, \tag{2.6}$$

where the subscript $_{,j}$ denotes differentiation with respect to x_j.

2.1.3 Deformation and Strain

A body under load experiments deformation, changing its geometry. Internal and external forces generate linear and angular displacements in a deformable body. In general, they are defined in terms of *strains*. Longitudinal (or normal) strains result from normal stresses and are related to changes in length. Normal strain ε of a material line element or fibre axially loaded is expressed as the change in length ΔL per unit of the original length L of the line element or fibres:

$$\varepsilon = \lim_{L \to 0} \frac{\Delta L}{L}. \tag{2.7}$$

Denoting displacements as $u_i = (u_x, u_y, u_z)$, the three normal strain components corresponding to the normal stress components are given by:

$$\begin{aligned} \varepsilon_{xx} &= \frac{\partial u_x}{\partial x}, \\ \varepsilon_{yy} &= \frac{\partial u_y}{\partial y}, \\ \varepsilon_{zz} &= \frac{\partial u_z}{\partial z}. \end{aligned} \tag{2.8}$$

There is also shear strain, which is a small distortion or change in angle between line segments in x and y directions, as in Figure 2.3:

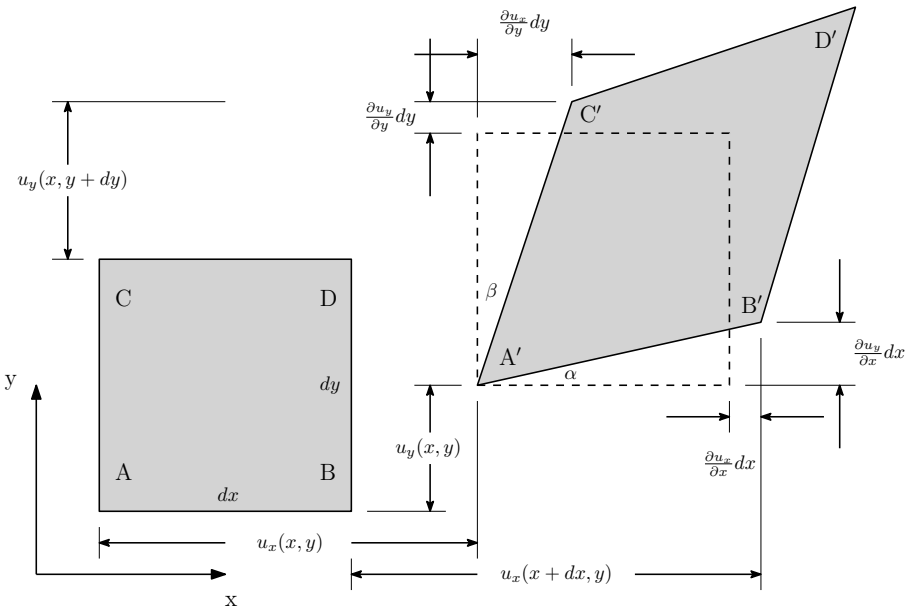

Figure 2.3 Shear strain.

They are mathematically defined as:

$$\begin{aligned}\gamma_{xy} &= \frac{1}{2}\left(\frac{\partial u_x}{\partial y} + \frac{\partial u_y}{\partial x}\right),\\ \gamma_{yz} &= \frac{1}{2}\left(\frac{\partial u_y}{\partial z} + \frac{\partial u_z}{\partial y}\right),\\ \gamma_{zx} &= \frac{1}{2}\left(\frac{\partial u_z}{\partial x} + \frac{\partial u_x}{\partial z}\right).\end{aligned} \tag{2.9}$$

Strain components can be represented in a matrix as follows:

$$\varepsilon_{ij} = \begin{bmatrix} \varepsilon_{xx} & \varepsilon_{xy} & \varepsilon_{xz} \\ \varepsilon_{yx} & \varepsilon_{yy} & \varepsilon_{yz} \\ \varepsilon_{zx} & \varepsilon_{zy} & \varepsilon_{zz} \end{bmatrix} = \begin{bmatrix} \varepsilon_{xx} & \frac{1}{2}\gamma_{xy} & \frac{1}{2}\gamma_{xz} \\ \frac{1}{2}\gamma_{yx} & \varepsilon_{yy} & \frac{1}{2}\gamma_{yz} \\ \frac{1}{2}\gamma_{zx} & \frac{1}{2}\gamma_{zy} & \varepsilon_{zz} \end{bmatrix}. \tag{2.10}$$

Both normal and shear stains can be expressed in index notation as:

$$\varepsilon_{ij} = \frac{1}{2}(u_{i,j} + u_{j,i}). \tag{2.11}$$

2.1.4 Compatibility

Compatibility conditions in linear elasticity are obtained by noting that the six strain-displacement relations ($\varepsilon_{xx}, \varepsilon_{yy}, \varepsilon_{zz}, \gamma_{xy}, \gamma_{xz}, \gamma_{yz}$) are functions of three unknown displacements. Therefore, by repeated differentiation of these relations, it is possible to remove displacements u_x and u_y given us the two-dimensional compatibility conditions:

$$\frac{\partial^2 \varepsilon_{xx}}{\partial y^2} - 2\frac{\partial^2 \gamma_{xy}}{\partial x \partial y} + \frac{\partial^2 \varepsilon_{yy}}{\partial x^2} = 0. \tag{2.12}$$

In two dimensions, there are three strain-displacement relations but only two displacement components, implying that strains are related. These relations between strains are known as compatibility conditions. It is an equation that must be satisfied by the strains at all material particles.

In the continuum description of a solid body we imagine the body to be composed of a set of infinitesimal volumes or material points. Each volume is assumed to be connected to its neighbors without any gaps or overlaps. Certain mathematical conditions have to be satisfied to ensure that gaps/overlaps do not develop when a continuum body is deformed. A body that deforms without developing any gaps/overlaps is called a compatible body. Compatibility conditions are mathematical

conditions that determine whether a particular deformation will leave a body in a compatible state.

2.1.5 Plane stress

A way to simplify the equilibrium Eqs. (2.5) is to use a two-dimensional approach of *plane stress* conditions. This case is applicable to thin plates, i.e., when the thickness of a solid is much smaller than the other dimensions. Considering that the thickness h is very small compared to the other two dimensions, the tractions are assumed to be symmetrically distributed with respect to the mid-plane of the body. In this stress state, we assume that stresses across the thickness are negligible, making σ_{zz}, τ_{xz} and τ_{yz} all zero. Another assumption is that the remaining components σ_{xx}, σ_{yy} and τ_{xy} are constant over the thickness. Equations (2.5) then become:

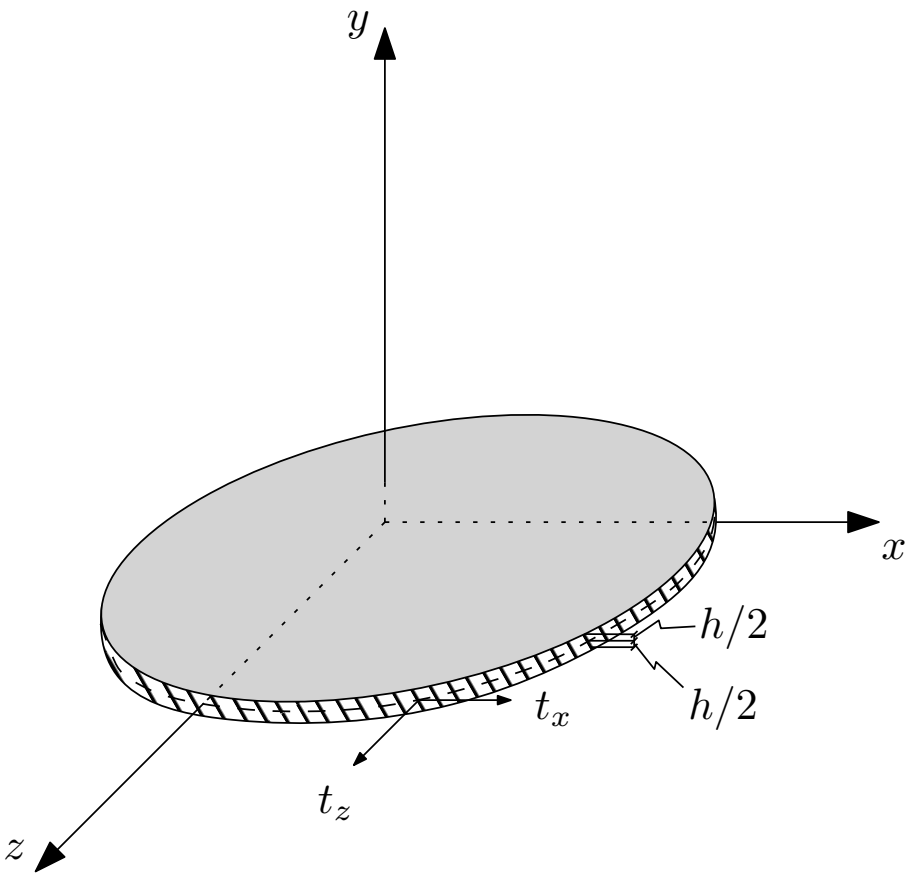

Figure 2.4 Thin elastic plate.

$$\begin{aligned} \frac{\partial \sigma_{xx}}{\partial x} + \frac{\partial \tau_{xy}}{\partial y} + b_x = 0, \\ \frac{\partial \tau_{yx}}{\partial x} + \frac{\partial \sigma_{yy}}{\partial y} + b_y = 0. \end{aligned} \tag{2.13}$$

2.1.6 Plane strain

Another possible way to simplify Eqs. (2.5) is to assume the *plane strain* conditions, which are applicable to thick bodies. This means that both geometry and loading do not vary significantly along the z direction. For these problems, it is enough to solve a cross-section along the z direction, given that the dependent variables are assumed to be function of x and y only. One consequence of this assumption is that displacement u_z in the z direction is equal to zero. This state of deformation appears in very long prismatic or cylindrical bodies, as in Fig. 2.5, in which a long dam is represented.

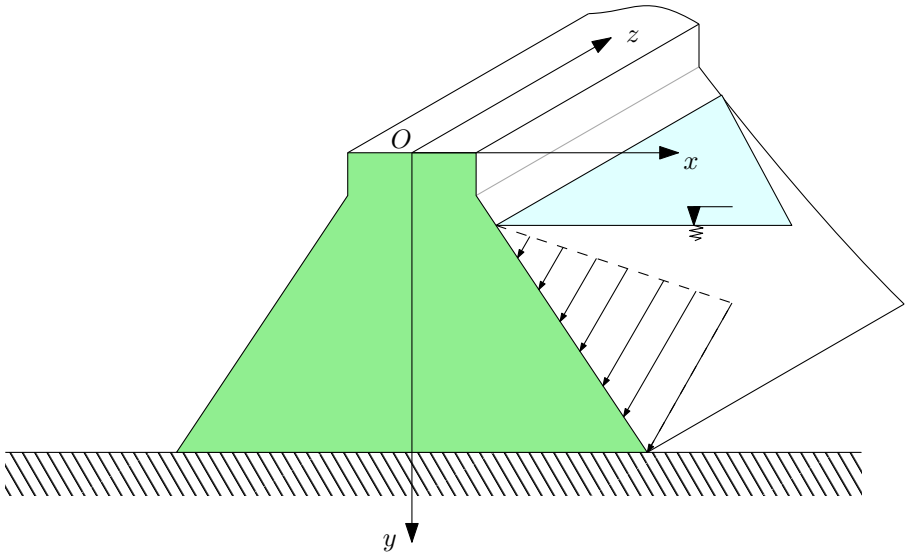

Figure 2.5 Cross-section of a long dam under plane strain [88].

$$\begin{aligned} \varepsilon_{xx} &= \frac{\partial u_x}{\partial x}, \\ \varepsilon_{yy} &= \frac{\partial u_y}{\partial y}, \\ \varepsilon_{zz} &= \frac{\partial u_z}{\partial z}. \end{aligned} \tag{2.14}$$

2.1.7 Hooke's law

It is known that every body under load will experiment deformation. In linear elastic materials, strain is directly related to stress acting in the body. This relation is given by Hooke's law, which correlates Cauchy's stress tensor and strain tensor. Considering a homogeneous isotropic material, generalized Hooke's law is written as:

$$\sigma_{ij} = \lambda \delta_{ij} u_{k,k} + G(u_{i,j} + u_{j,i}) \tag{2.15}$$

where λ is the *Lamé constant*, G is the shear modulus, which are defined in terms of Young's modulus E and Poisson's ratio ν:

$$\lambda = \frac{\nu E}{(1+\nu)(1-2\nu)}, \tag{2.16}$$

and

$$G = \frac{E}{2(1+\nu)}. \tag{2.17}$$

δ_{ij} is the *Kronecker delta*, with the following properties:

$$\delta_{ij} = \begin{cases} 0, \; if \; i \neq j \\ 1, \; if \; i = j \; . \end{cases} \tag{2.18}$$

3 Contact Mechanics

As previously said, contact and fretting are of high interest when designing several mechanical components, from bolted connections to jet turbines. Formal studies of tribology, although still in an embryo state, can be traced back to the 15th century, when Leonardo da Vinci investigated blocks being dragged along planes with different inclinations. His recordings in several notebooks - see Fig. 3.1 - are well-known among researchers [89]. Additionally, he studied the influence of contact pressure and contact area on friction.

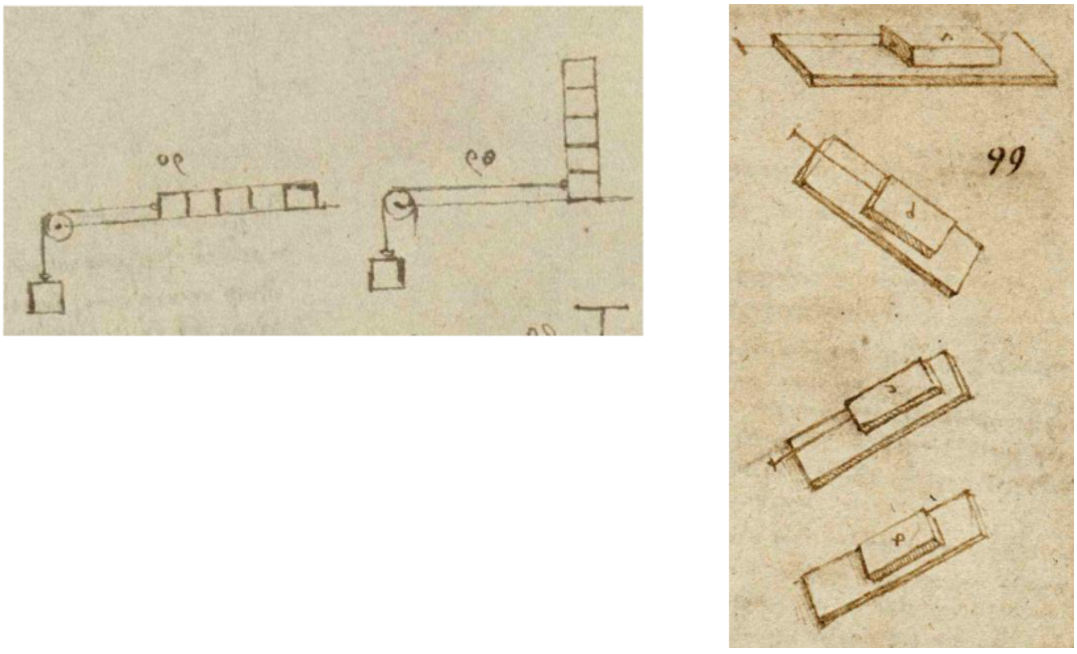

Figure 3.1 An excerpt from Leonardo da Vinci's notebook [89]. (a) Sketches illustrating the effect of contact pressure or contact area on friction. (b) Blocks sliding with different inclinations.

3.1 Initial considerations

[90] and [91] also developed their studies on friction. Those studies originated what today is widely known as Coulomb's law of friction, and which is used in the present work. Another major contributor

to contact formulations is [92], who developed analytical solutions for elastic bodies in contact, from elasticity and friction laws.

More recent references include [93], and [38]. While designing a structural component, the engineer should be aware to avoid yield and brittle fracture. Dealing with yield is easier, requiring the determination of stresses and designing the component to maintain stress below the yielding point. Design against brittle fracture is harder and requires not only the determination of the state of stress within an object, but also some speculation on the form, location, and origin of initial defects. After the nucleation, these flaws usually grow by fatigue due to normal use during service life and, if nothing is done, they may reach the critical threshold leading to catastrophic brittle failure.

It is worth mentioning that the fatigue life of a crack has two different phases: nucleation and propagation. According to [37], the relative proportion of the total life expended in each stage will vary tremendously. Among several factors, surface finish (ground, machined or cold-drawn, hot-rolled or as-forged) influences nucleation and propagation time. Welded structures or those made from casting will have some pre-existing defects and the entire life is expended in propagation.

Another form of crack initiation is where there is a connection between two components. Much more agressive than the crack initiation prevalent at a free surface, this is the phenomenon of fretting [37]. Fretting normally occurs whenever a junction between two components is subjected to some oscillating force, and this gives rise to some minute relative tangential displacement over at least part of the interface. It is fairly common in bolted or mechanically fastened joints, such as seen in Fig. 3.2.

Figure 3.2 A bolted connection [94].

As multi-body contact has several applications in practical situations, some previous works also used BEM for analysing contact problems. [95] and [96], who used BEM for solving 2D non-linear

frictional stress under proportional loading, [97], analysed a Cattaneo-Mindlin problem using BEM, and [98] presented a boundary integral formulation of frictionless contact problems based on an energetic approach. They all used standard polynomial BEM instead of IGABEM, one noticeable difference from the present study. There are some works that model fretting-wear problems using BEM, such as [99], [100], [101], and [102]. Also, [103], present a boundary element formulation for 3D fretting-wear, and [104], extend it for anisotropic problems. In these articles, the *Holm-Achard wear law* is used in addition to contact formulation. It can be seen from these results that the BEM is suitable to solving fretting-wear problems, as they present good agreement with the theoretical known solutions.

Breakage of conductive cables occurs mainly due to fatigue, as a consequence of wind forces, which cause vibration with high frequency and low amplitude. These vibrations are mainly present in long spans, for example over wide rivers. Although this is a computational study, it aims to compare the obtained results with the experimental results of [105], and [77]. These works used Aluminum Conductor Steel Reinforced (ACSR) conductors, which are a type of stranded conductors with outer-strands made of aluminium and the central strand is of steel for additional strength.

3.2 Contact modes

Figure 3.3 shows a classification of contact modes. The first illustration (Fig. 3.3 (a)) depicts a rigid cylinder with radius R, pressed against a half-plane. As bodies firstly touch each other, contact is made along a line and, with load increase, contact semi-width a rises. This kind of contact is referred to as "incomplete", because it is not geometrically fixed, it varies with load. Besides that, contact pressure is zero on its end. Figure 3.3 (b) illustrates a complete contact where the contact area is not influenced by load and contact pressure has a singularity because there is no common tangent between the bodies at the contact end. The next illustration (Fig. 3.3 (c)) is a mix of previous modes, as it has an edge with singularity and other in which the pressure goes to zero. Lastly, Fig. 3.3 (d) represents a conforming incomplete contact.

In the present study, contact zone behaviour is in accordance with classical computational mechanics works such as [106]. There is a correlation between contact pressure p_N and relative distance between the bodies, also known as gap v_N:

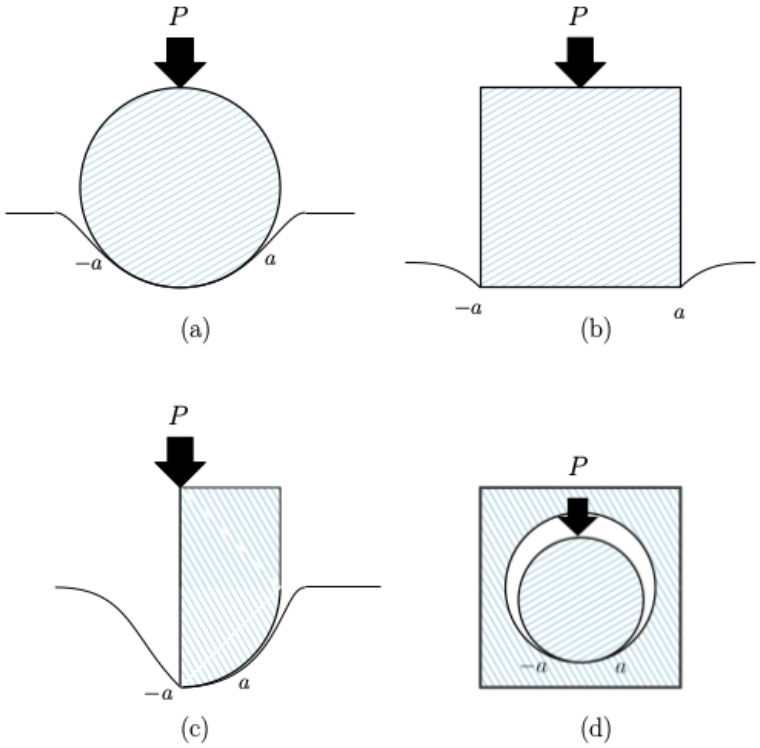

Figure 3.3 Contact modes: (a) Non-conforming incomplete; (b) Complete; (c) Incomplete with singularity; (d) Conforming and incomplete.

$$\begin{aligned} v_N &\geq 0, \\ p_N &\leq 0, \\ p_N v_N &= 0. \end{aligned} \tag{3.1}$$

These two exclusive status: gap or non-contact ($v_N > 0$ and $p_N = 0$) or contact ($v_N = 0$ and $p_N > 0$) are classically formulated by an impenetrability condition ($v_N \geq 0$), a compression condition ($p_N \leq 0$) and a complementary condition.

One important study is pressure on the surface of contact. Considering two elastically similar bodies in normal contact as in Fig. 3.4, as load is applied, contact pressure compresses both bodies and a parallel displacement to contact zone occurs. However, as they both have the same elastic properties, their particles will experience the same displacement in the x-direction, i.e., even with a non-zero friction coefficient f between the surfaces, there will be no shear stress.

If a tangential load is applied and it is enough to start the slip between the two bodies, shear stress

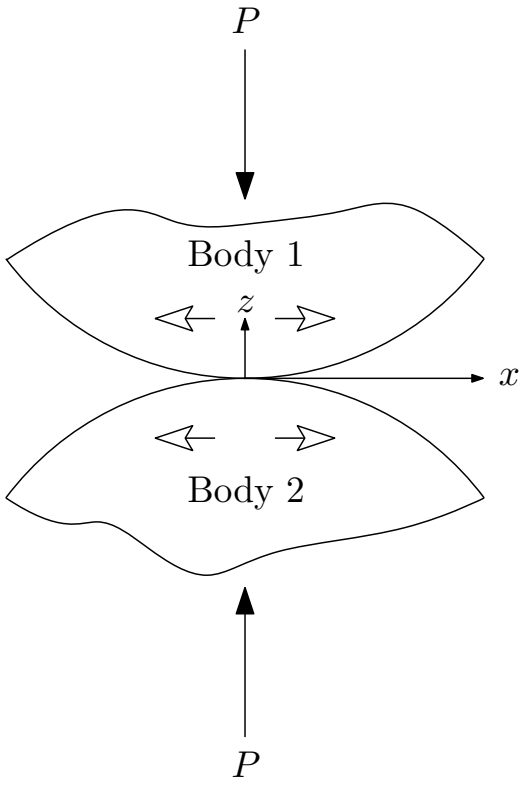

Figure 3.4 Normal contact between elastically similar bodies.

will appear. This stress will be the same over the entire contact and limited by friction coefficient f:

$$|q(x,y)| = -fp(x,y), \tag{3.2}$$

where $p(x,y)$ is the normal contact pressure and $q(x,y)$ is the shear stress distribution. The direction of shear tractions opposes relative motion of the surfaces:

$$sgn(q(x)) = -sgn\left(\frac{\partial g}{\partial t}\right), \tag{3.3}$$

where $g = u_1(x) - u_2(x)$ is the relative displacement of the contacting surfaces. Due to this shear stress, a normal displacement will arise between the bodies surfaces. However, as they are elastically similar, normal displacement will be the same, maintaining contact pressure the same as before. Fretting problems usually have a smaller Q, which is not enough to create a total slip condition, i.e.:

$$|Q| < -fP, \tag{3.4}$$

where P is the normal load. During fretting, the contact zone is divided in two parts, one stick and the other slip. Figure 3.5 illustrates this better.

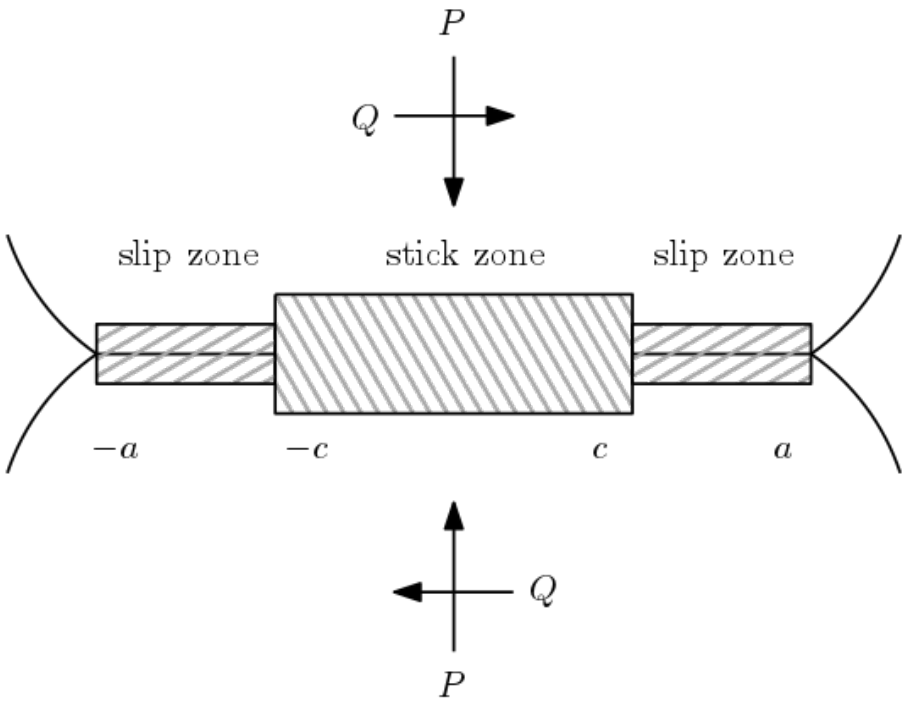

Figure 3.5 Contact zones.

Within slip zone, shear traction is given by Eq. (3.2) and normal pressure tends to zero as it goes to contact end. In stick zone, in turn, shear is given by Eq. (3.5):

$$|q(x,y)| < -fp(x,y). \tag{3.5}$$

3.2.1 Contact modes evaluation

When solving computational contact problems, it is usual to assume a probable contact region because of the changing zone, which changes with load. Internal nodes of these regions are often called as contact node-pairs. They can be one of three contact modes, depending on shear and normal tractions, t_t and t_n, and on shear and normal displacements, u_t and u_n, respectively.

Let a and b be a node-pair initially in separation with a gap between them. As the load increases, bodies 1 and 2 experiment deformation, reducing this gap and, at some time, this deformation will be equal to the gap and both bodies will be in contact at that point. If the load continues to increase even more, this node-pair will be part of the contact area. While modelling, contact modes can be thought as constraints that must be satisfied for each node-pair within the contact zone. They can be each one of the following three:

- **Separate** is when both nodes are within a positive and non-zero distance from each other.

- **Slip** is when there is no gap between nodes, there is no restriction in tangential direction and they are free to slide over each other.

- **Stick** represents when a pair of nodes are restricted in normal and tangential directions.

Table 3.1 gives values of how to represent the three modes of contact previously stated, where t_n and t_t are the normal and tangential tractions, and u_n and u_t are the normal and tangential displacements, respectively, expressed in local coordinates. The gap^{ab} is the distance between bodies a and b.

Table 3.1 Contact modes.

Separate	Slip	Stick
$t_t^a - t_t^b = 0$	$t_t^a - t_t^b = 0$	$t_t^a - t_t^b = 0$
$t_n^a - t_n^b = 0$	$t_n^a - t_n^b = 0$	$t_n^a - t_n^b = 0$
$t_t^a = 0$	$t_t^a \pm f t_n^a = 0$	$u_t^a - u_t^b = 0$
$t_n^a = 0$	$u_n^a - u_n^b = gap^{ab}$	$u_n^a - u_n^b = gap^{ab}$

It is important to bear in mind that a node-pair might change its contact mode from one iteration to the next.

3.2.2 Plane problem formulation

To obtain the sub-superficial stress, it is necessary to first determine shear stress field and pressure distribution over the contact area. For that, the integral equations relating pressure $p(x)$ and normal displacement $h(x)$ as in Figure 3.6 have to be solved, as well as shear stress distribution with relative tangential displacement $g(x)$. A more interested reader may look for [37] for details.

The normal load distribution over contact zone is given by:

$$\frac{1}{A}\frac{\partial h}{\partial x} = \frac{1}{\pi}\int_{-a}^{a}\frac{p(\xi)}{x-\xi}d\xi \tag{3.6}$$

And, for tangential load:

$$\frac{1}{A}\frac{\partial g}{\partial x} = \frac{1}{\pi}\int_{-a}^{a}\frac{q(\xi)}{x-\xi}d\xi \tag{3.7}$$

ξ is the load variable of integration and A is a measure of the compliance of the bodies:

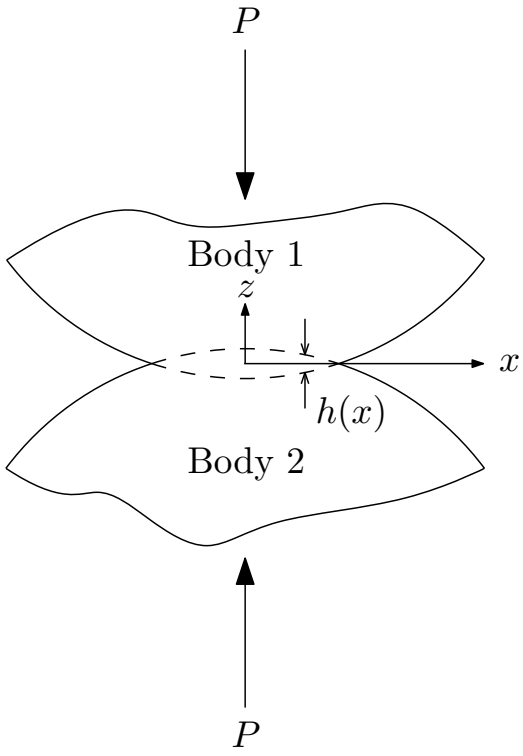

Figure 3.6 Contact between two elastically similar bodies.

$$A = 2\left(\frac{k+1}{4\mu}\right) \tag{3.8}$$

where $k = 3-4\nu$ in plane strain, ν is the Poisson's ratio and μ is the modulus of rigidity. It is important to mention that Dundurs' constant ([37]) is not taken into consideration in Eq. (3.6) because it will vanish as we are considering two bodies made from the same material.

3.3 Muskhelishvili's potential

According to [37], although a direct method of attack, based on integration of the solution for a line load is feasible, it is inefficient. A way to overcome this is using Muskhelishvili potentials, which uses complex numbers. During this study, we shall denote the complex representation of a coordinate by z as:

$$z = x + iy. \tag{3.9}$$

In Fig. 3.7, a semi-plane is under shear and normal tractions and the objective is to determine stress in an arbitrary point inside the domain. Using Eq. (3.9) to represent coordinates, Muskhelishvili's

potential is:

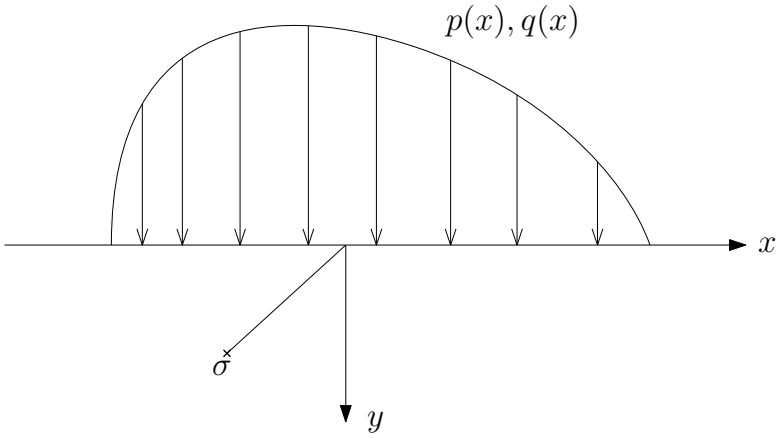

Figure 3.7 Semi-plane under arbitrary load.

$$\Phi(z) = \frac{1}{2\pi i} \int \frac{p(t) - iq(t)}{t - z} dt, \tag{3.10}$$

where $p(t)$ and $q(t)$ are arbitrary normal and shear loads, respectively. Considering slip condition, they are defined by Equation (3.2). Thus, Eq. (3.10) is written as:

$$\Phi(z) = \frac{1 - if}{2\pi i} \int \frac{p(t)}{t - z} dt. \tag{3.11}$$

The relationship between the potential $\Phi(z)$ and the stress components are:

$$\sigma_{xx} + \sigma_{yy} = 2(\Phi(z) + \overline{\Phi}(\overline{z})) \tag{3.12}$$

and

$$\sigma_{yy} - \sigma_{xx} + 2i\tau_{xy} = 2((\overline{z} - z)\Phi'(z) + \overline{\Phi}(z) - \Phi(z)). \tag{3.13}$$

where $\Phi'(z)$ is the derivative of pontential with respect to z, $\overline{\Phi}(z)$ is the conjugate of potential and $\overline{\Phi}(\overline{z})$ is the conjugate of pontential of conjugate of z. Thus, only $\Phi'(z)$, $\overline{\Phi}(z)$ and $\overline{\Phi}(\overline{z})$ need to be evaluated in order to obtain all stress components, which provides some economy in computational requirements.

3.4 Hertz's theory

A simple but important problem is the contact between two cylinders, pressed together with their axes parallel. [92] created the analytical solution for contact problems, while making some assumptions:

- Surfaces are non conforming and radii are much larger than contact width $(a << R)$;
- Loads are small; this enables the relative normal approach of particles within the contact to be approximated by a parabola.
- No shear traction must arise. Either the friction coefficient is zero $(f = 0)$ or both bodies have the same elastic constants.

For achieving solutions (also known as inversions), it is important to isolate $p(x)$. Before doing that, however, it is important to define a weight function $w(x)$ as, for this case (contact pressure is zero on both ends) $w(x) = \sqrt{a^2 - x^2}$. So, $p(x)$ is given by:

$$p(x) = -\frac{w(x)}{A\pi} \int_{-a}^{a} \frac{h'(\xi)}{w(\xi)(\xi - x)} d\xi + cw(x) \tag{3.14}$$

$$p(x) = -\frac{\sqrt{a^2 - x^2}}{A\pi} \int_{-a}^{a} \frac{k\xi}{\sqrt{a^2 - x^2}(\xi)(x - \xi)} d\xi \tag{3.15}$$

where k is the parabola curvature.

Evaluation of the integral results in:

$$p(x) = \frac{k}{A\pi}\sqrt{a^2 - x^2}\pi = \frac{k}{A}a\sqrt{1 - \left(\frac{x}{a}\right)^2}. \tag{3.16}$$

Equation (3.16) is of limited use, because in this form, the semi-width a is unknown. Assuring equilibrium between applied load P and contact pressure:

$$P = -\int_{-a}^{a} p(\xi) d\xi = \frac{\pi k a^2}{2A}. \tag{3.17}$$

Simplifying for an elastic semi-space results in:

$$p(x) = -p_0\sqrt{1-\left(\frac{x}{a}\right)^2}, \tag{3.18}$$

where p_0 is peak contact pressure, obtained from:

$$p_0 = \frac{2P}{\pi a}, \tag{3.19}$$

and a is semi-width, given by:

$$a^2 = \frac{2PA}{\pi k}. \tag{3.20}$$

3.4.1 Contact under partial slip

Until now, two different types of problems were formulated. The first and simpler one was where only normal force was applied, resulting in a null shear traction distribution. The other was where shear tractions were equal to the limit $q(x) = fp(x)$, so the shear force $Q = fP$ results in gross sliding all over the contact surface.

A brief explanation about commonly used friction laws is a useful way to start fretting studies. Coulomb friction is a usual name for the theory created by Amontons and Coulomb based on experimental investigation. Consider two rigid bodies experiencing gross sliding. The assumptions of this theory are:

- Frictional force Q, which opposes the relative motion between the two bodies, is proportional to the normal force P. $Q = fP$, where f is the friction coefficient.
- Frictional force Q is independent of the area of contact.
- Frictional force that arises during gross sliding is independent of the velocity of sliding.

In the previous section the Hertzian contact was presented, which is when two elastically-similar cylinders (or a cylinder and a flat surface) are pressed together under the action of a normal force P. Now consider a *subsequent* application of a monotonically increasing tangential force Q, taking care to set $Q < fP$. The aforementioned stick and slip regions will arise, but they are unknown *a priori*. As the shear distribution over the surface is given by:

$$q(x) = \frac{C}{\sqrt{a^2 - x^2}}, \tag{3.21}$$

where C is a constant. One can observe that $q(x)$ tends to infinity when $x \to \pm a$ and $p(x)$ vanishes. Hence, $q(x)/p(x) \to \infty$ and an infinite friction coefficient is required to avoid slip. Therefore, some slip will occur, even if the tangential load Q is small.

For analysing the partial slip case, assume that the slip takes place in two symmetrical regions $a > |x| \geq c$ on the edge of a central stick zone $|x| < c$. One can think of the shear tractions as a perturbation on the fully-sliding solution as:

$$q(x) = f p_0 \sqrt{1 - (x/a)^2} + q'(x), \tag{3.22}$$

where the perturbation $q'(x) = 0$ in the slip zones. For determining $q'(x)$ in the stick zone and its size c we start by recalling that there is no relative displacements within the stick zone. Full description of the process can be found in [38] and the ratio between stick and contact zones is c/a:

$$\frac{c}{a} = \sqrt{1 - \frac{Q}{fP}}. \tag{3.23}$$

The distribution of shear tractions for different values of Q/fP is shown in Figure 3.8. It is clear from it that the central stick zone increases when Q/fP decreases. Also, when $Q/fP = 1$ there is no stick zone, i.e., gross sliding occurs between the surfaces.

According to [38], surface tractions can be thought of as a superposition of three elliptical distrubutions:

1. A distribution of normal pressure of peak magnitude p_0 acting between $x = -a$ and $x = a$.

2. A distribution of shear traction of peak magnitude $f p_0$ acting between $x = \pm a$.

3. A second shear traction distribution of peak magnitude $-f p_0 c/a$ between $x = \pm c$.

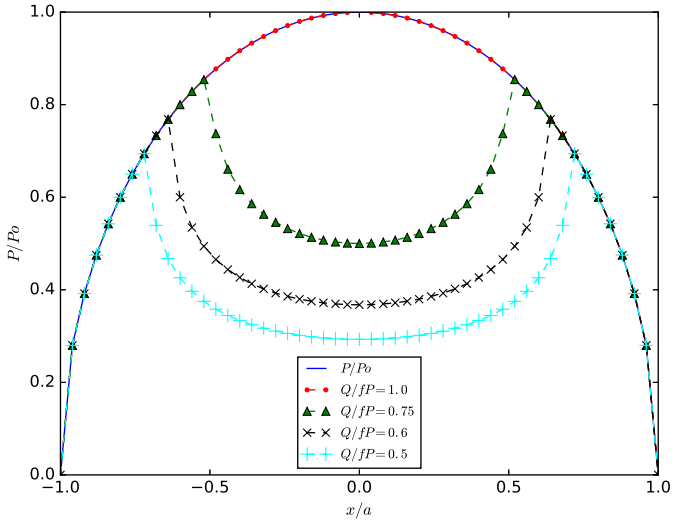

Figure 3.8 Shear traction distributions for different values of Q.

3.4.2 Load variation

Problems analysed until now have been all for a monotonically applied tangential force. In fretting fatigue, though, that is not the case - there is a cyclic variation of a tangential force between constant limits ($\pm Q_{max}$) as in Fig. 3.9. Previous equations were written considering the tangential load in its maximum value Q_{max} (or $-Q_{max}$), which is respresented by point A (or E) in Fig. 3.9.

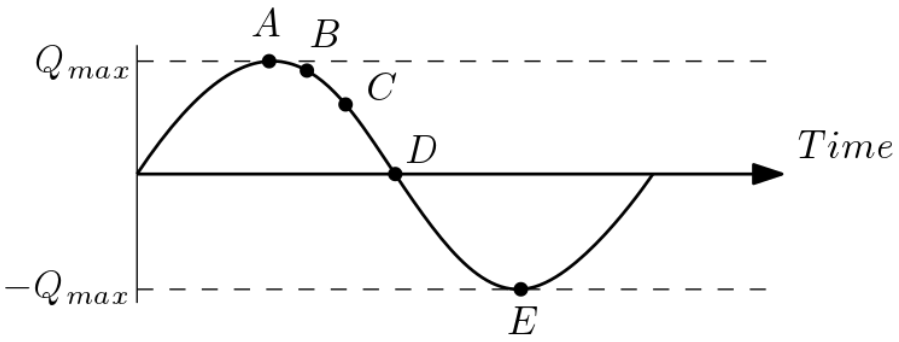

Figure 3.9 Tangential load history during fretting.

Let us consider two cylinders in contact with each other as in the previous section. The tangential load Q starts to increase monotonically from 0 to Q_{max}, reaching point A. Shear tractions are described by Equation (3.22) where the stick zone, c, is given by:

$$\frac{c}{a} = \sqrt{1 - \frac{Q_{max}}{fP}}. \tag{3.24}$$

Proceeding to point B in loading history, the tangential load has been reduced *infinitesimally* from Q_{max}. Due to this, shear tractions and tangential displacements also decrease. This means that the rate of change of relative displacement $\frac{\partial g}{\partial t}$ is opposite in sign to that in increasing load period.

Therefore, the requirement for the shear tractions in the slip zone to oppose relative motion is violated, creating an instant of complete stick all over the contact region as in Fig. 3.10. A further reduction in Q will lead to reverse slip at the edges of the contact (point C). So, in the new slip regions ($c' < |x| \leq a$) the shear tractions will be $-fp_0\sqrt{1-(x/a)^2}$ instead of $fp_0\sqrt{1-(x/a)^2}$. A further corrective traction distribution should be applied to the new stick zone $|x| < c'$.

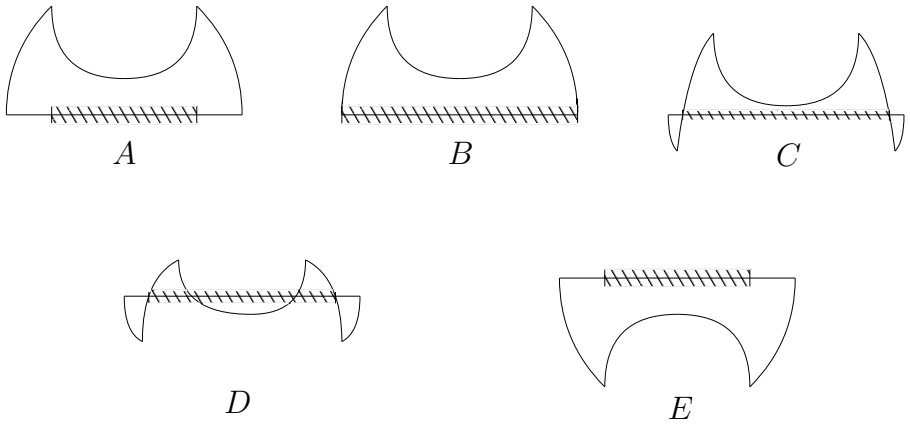

Figure 3.10 Shear tractions during loading cycle of Fig. 3.9.

By analogy, the new corrective shear distribution is:

$$q''(x) = +2fp_0\frac{c'}{a}\sqrt{1-(x/c')^2}. \tag{3.25}$$

The factor two arises due to the need to cancel the relative displacements occurring when slip zone tractions change by $2fp_0\sqrt{1-(x/a)^2}$, unlike $fp_0\sqrt{1-(x/a)^2}$ for the monotonically increasing case. Table 3.2 presents four terms that when summed together are the total shear traction:

Table 3.2 Four terms contributing to shear over each zone.

$q(x)$	**Zone of application**
$fp_0\sqrt{1-(x/a)^2}$	$\lvert x\rvert \le a$
$-fp_0\left(\frac{c}{a}\right)\sqrt{1-(x/c)^2}$	$\lvert x\rvert \le c$
$-2fp_0\sqrt{1-(x/a)^2}$	$\lvert x\rvert \le c$
$2fp_0\left(\frac{c'}{a}\right)\sqrt{1-(x/c')^2}$	$\lvert x\rvert \le c'$

After summing the terms, net shear tractions are:

Table 3.3 Shear traction distributions for each zone for the history loading.

$q(x)/fp_0$	**Zone of application**
$-\sqrt{1-\left(\frac{x}{a}\right)^2}$	$c' < \lvert x\rvert \le a$
$-\sqrt{1-\left(\frac{x}{a}\right)^2}+2\frac{c'}{a}\sqrt{1-\left(\frac{x}{c'}\right)^2}$	$c < \lvert x\rvert \le c'$
$-\sqrt{1-\left(\frac{x}{a}\right)^2}+2\frac{c'}{a}\sqrt{1-\left(\frac{x}{c'}\right)^2}-\frac{c}{a}\sqrt{1-\left(\frac{x}{c}\right)^2}$	$\lvert x\rvert \le c$

As seen in [38], using equilibrium for calculating the position of the new stick zone yields:

$$\frac{c'}{a} = \sqrt{1-\frac{Q_{max}-Q(t)}{2fP}}. \tag{3.26}$$

An interesting fact happens when tangential load reaches point D in Fig. 3.9: even though there is no tangential force anymore, some non-zero but self-equilibrating shear tractions persist. From this, we conclude that the traction distribution depends on the history of loading. Therefore, it is not possible to use superposition for determining the stress state. Figure 3.11 depicts the history of shear tractions for an example case.

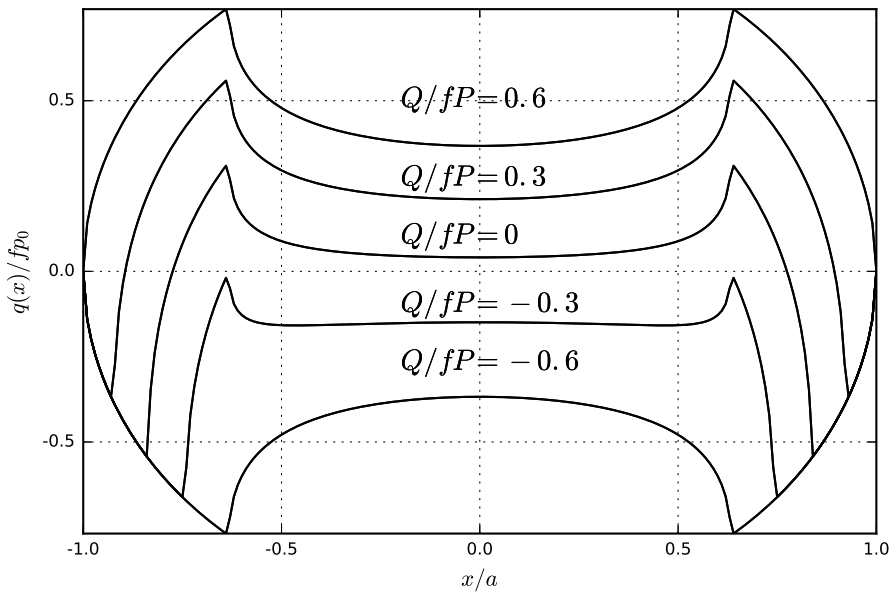

Figure 3.11 Shear traction distributions during cycling of a tangential load.

3.4.3 Effect of bulk stress

Often fretting fatigue involves more than just the aforementioned normal and tangential loads. For better understanding, imagine a turbine engine where the stresses arise due to the centrifugal load in addition to the loading imposed by the blades. Figure 3.12 shows a tipical setting for experiment where the speciment is subjected to an oscillating bulk stress σ. As the specimen is extended to the right-hand side direction, the pads move with it and are retained by the springs, originating a tangential fretting force Q, applied to the contact in phase with the bulk load. After carefully analysing the figure one can see that the specimen, which is under a bulk stress, experiences a bulk strain ε, whereas the pads do not. This creates another term in the tangential direction so the resulting shear tractions will be different from the case without bulk stress. Unlike our previous situations, the stick zone will not be centrally located. Then, the stick zone can be assumed to extend from $x = e - c$ to $x = e + c$ where e is the offset of the centre stick zone with relation to the centre of the contact, given by Eq. (3.27):

$$\frac{e}{a} = \frac{\sigma_b}{4fp_0}. \tag{3.27}$$

Equation (3.27) holds for the maximum absolute value of the tangential load and the stick zone becomes $|x - e| \leq c$. For different values of Q, during loading or unloading, equation is used and stick zone becomes $|x - e'| \leq c$, as in Eq. (3.28):

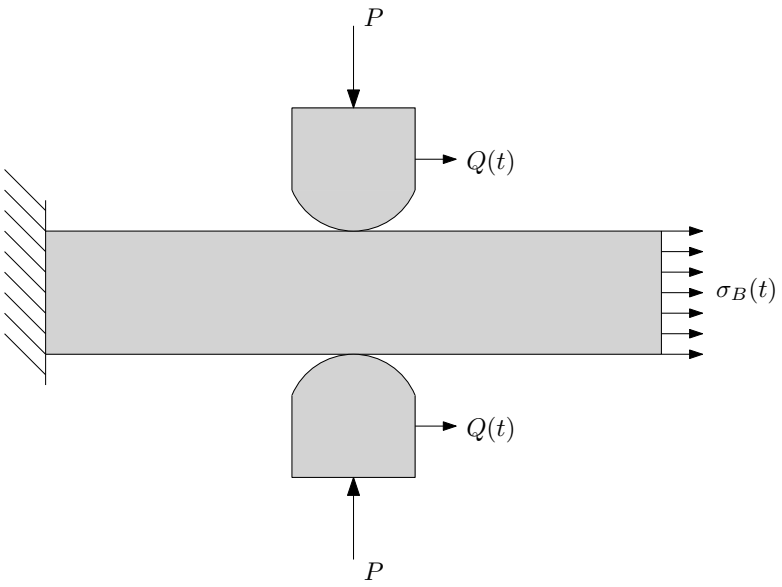

Figure 3.12 Typical setting of a fretting fatigue experiment.

$$\frac{e'(t)}{a} = \frac{\sigma_b - \sigma_b(t)}{8fp_0}. \tag{3.28}$$

It is worth mentioning that the above solution is true only when $e + c \leq a$:

$$\frac{\sigma}{fp_0} \leq 4(1 - \sqrt{1 - Q/fP}). \tag{3.29}$$

If the bulk stress is larger, reverse slip arises at one edge of the contact. Figure 3.13 shows shear tractions with a bulk stress and a shifted stick zone.

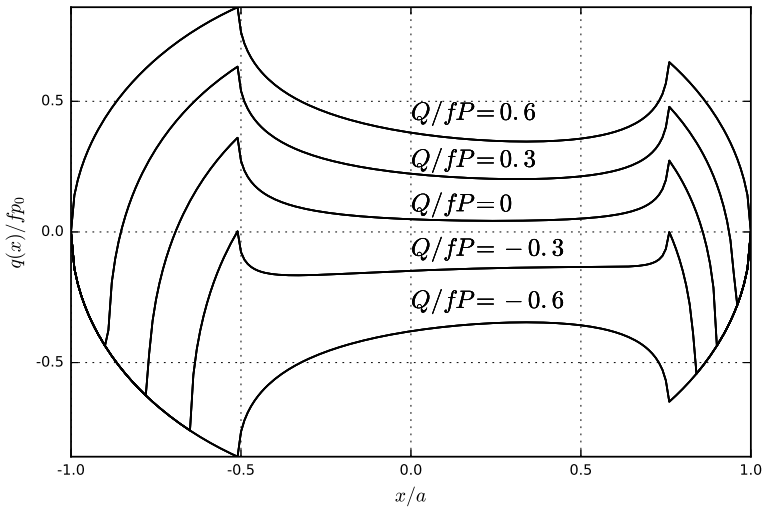

Figure 3.13 Cyclic load with bulk stress in phase tangential load.

4 Fretting fatigue and life estimation

As previously said, fretting is a phenomemon that originates from the surface microslip associated with small-scale oscillatory motion. Wear, corrosion and fatigue all contribute to fretting, which is a crack nucleation mechanism. Comparing plain and fretting fatigue is important to see how the latter influences the life of a given component. Figure 4.1 illustrates the life of AlSi9Cu2Mg aluminum alloy for both plain and fretting fatigue according to [107] experimental data. Interestingly, the stress level required to reach the endurance level is smaller in fretting fatigue.

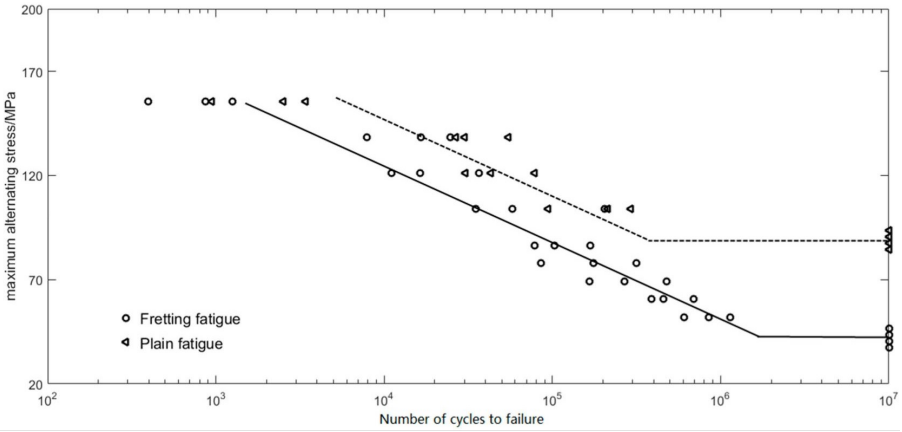

Figure 4.1 S-N curves comparing plain and fretting fatigue for AlSi9Cu2Mg aluminum alloy [107].

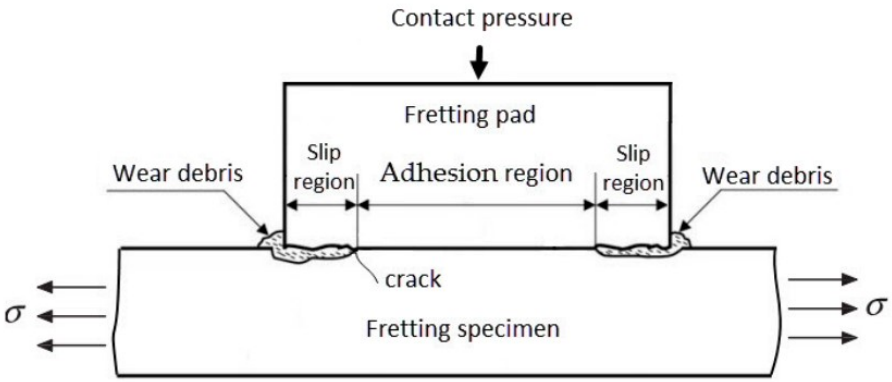

Figure 4.2 Schematic view of the contact region [107].

Also, according to [108], states of stress and strain are more severe in fretting fatigue when

compared to plain fatigue, resulting in an accelerated crack nucleation in the former. Also, experimental studies have shown that the crack usually initiates at the trailing edge of the contact. Fig. 4.2 shows that wear debris accumulates near the edges of the contact. This can change the friction coefficient, causing severe abrasion and further accelerating the failure process.

Fatigue can be divided into three steps: crack nucleation, crack propagation, and failure. They are detailed next.

4.1 Fretting

4.1.1 Crack nucleation

According to Hills and Nowell [37], crack initiation must be viewed as a continuous process rather than a discrete event and it occurs due to gradual damage accumulation. This phenomenon happens on a microscopic scale, within grains of the material. In fretting fatigue, the stress concentration due to contact is so severe that often originates several micro cracks. These are nucleated at the contact edge where the stresses are more concentrated, at the surface of the component. In aircraft industry, this stage represents most of the component's life, as they are replaced when a crack is detected.

4.1.2 Crack propagation

It is not straightforward to differentiate crack nucleation from crack propagation. Hills and Nowell [37] states that crack propagation definition depends on what level of crack detection equipment is available. If there is no crack above detection size, then the nucleation phase is still ongoing. Once the crack is detected, it is considered to be in propagation stage. Another approach defines propagation as the period of component life where the crack behaviour can be described by fracture mechanics. Even though several micro cracks may be nucleated, not all of them reach propagation phase. There is the phenomenon of crack arrest, first reported by [109]. A crack propagates when the stresses opening it are higher than the fatigue limit.

If the crack continues to grow, it may eventually reach a critical size and its propagation can be predicted using the stress intensity factor K - [110].

4.1.3 Fracture

When the intensity factor reaches the fracture toughness, K_c, catastrophic failure occurs. This K_c value is a material constant and does not depend on the geometry [111]. The crack propagation and the fractures zone are noticeable even with naked eye. The latter has a polished appearance and presents Wallner lines, whereas the former has a rough matte surface.

Figure 4.3 Fatigue failure of a rail [112].

4.2 Fatigue life

There are two main categories to approaching fatigue life. The total-life approach and the defect-tolerant approach. This study focus on the former. In the late 1800s, Wöhler [25, 26] studies originated the S-N curve (known as Wöhler diagram). It relates the stress amplitude applied to a specimen with the number of cycles for failure. Most experimental investigations of fatigue use this curve, which can be obtained by some different tests (push-pull, rotating-bending, torsion).

When it comes to fatigue life, ferrous and non-ferrous materials present different behaviours. Fig. shows the relationship between stress, σ, and the number of cycles to failure, N_f, for steel specimens. An abrupt change can be seen in the S-N curve slope, which is often referred to as "knee point". The stress amplitude at this point is the fatigue limit because even after a high number of cycles, the specimen will not fail. Non-ferrous metals, on the other hand, do not have a defined fatigue limit. Fig.

4.4 shows an aluminium alloy S-N curve, in which the fatigue limit continues to decrease. For this reason, fatigue limit for non-ferrous metal is assumed as the stress amplitude for $N_f = 10^7$.

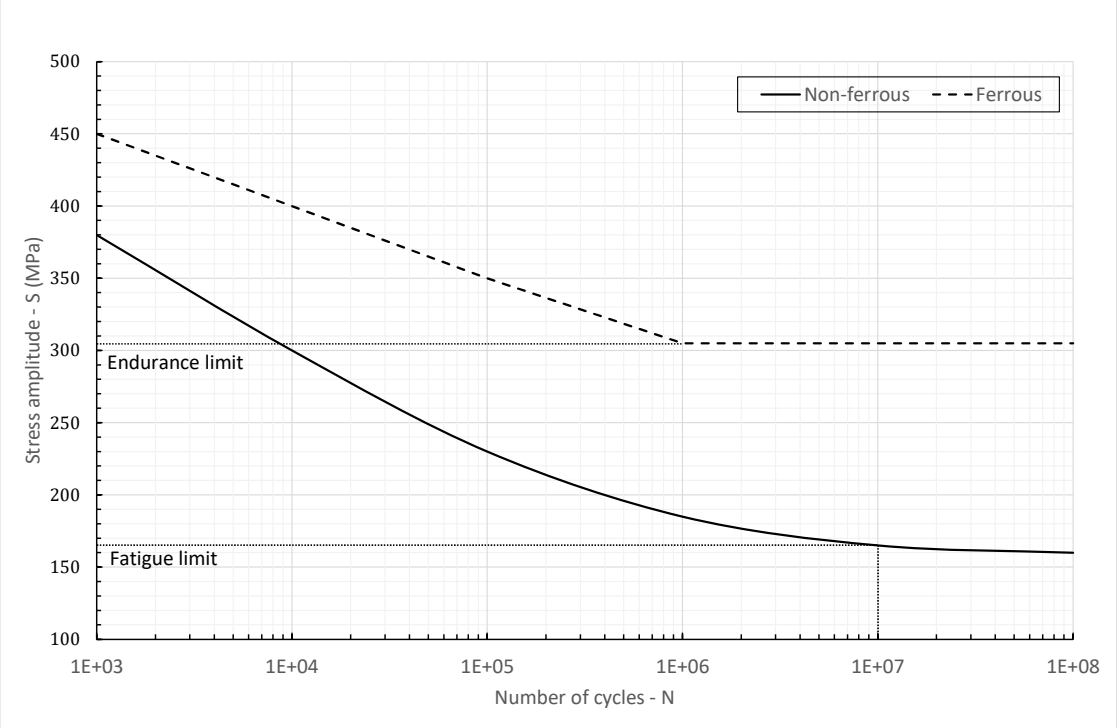

Figure 4.4 S-N curves of ferrous and non-ferrous metals.

4.2.1 Multiaxial

Crack nucleation in fretting fatigue occurs in a region under multiaxial stress state.

There are three main approaches to predict fatigue life of material submitted to multiaxial loading: the critical plane, the invariant tensor and the energetic approach.

Non-local approaches such as the Theory of Critical Distances (TCD) have been widely used recently. The Modified Wöhler Curve Method, Smith-Watson-Topper and Fatemi-Socie are examples of TCD.

Critical plane

The CPM is based on experimental data that crack nucleation preferentially starts on planes under high shear stress. Mean normal stresses are also considered, as they are expected to open crack faces,

resulting in easier crack growth. One of CPM's main advantages is that it not only predicts fatigue life but also gives information on the orientation and location of the fatigue fracture plane. [113], [114], [115].

Defining shear stress amplitude τ_a, however, is not a simple task for multiaxial stress situation. The problem lies in how to define an amplitude for a time varying shear stress vector in a material plane δ passing through point O. Plane orientation is described by the spherical coordinates ϕ and θ. Using Cauchy's theorem, vector $\mathbf{t}(t)$ is function of normal vector $\mathbf{n}$ and the stress tensor $\mathbf{T}(t)$.

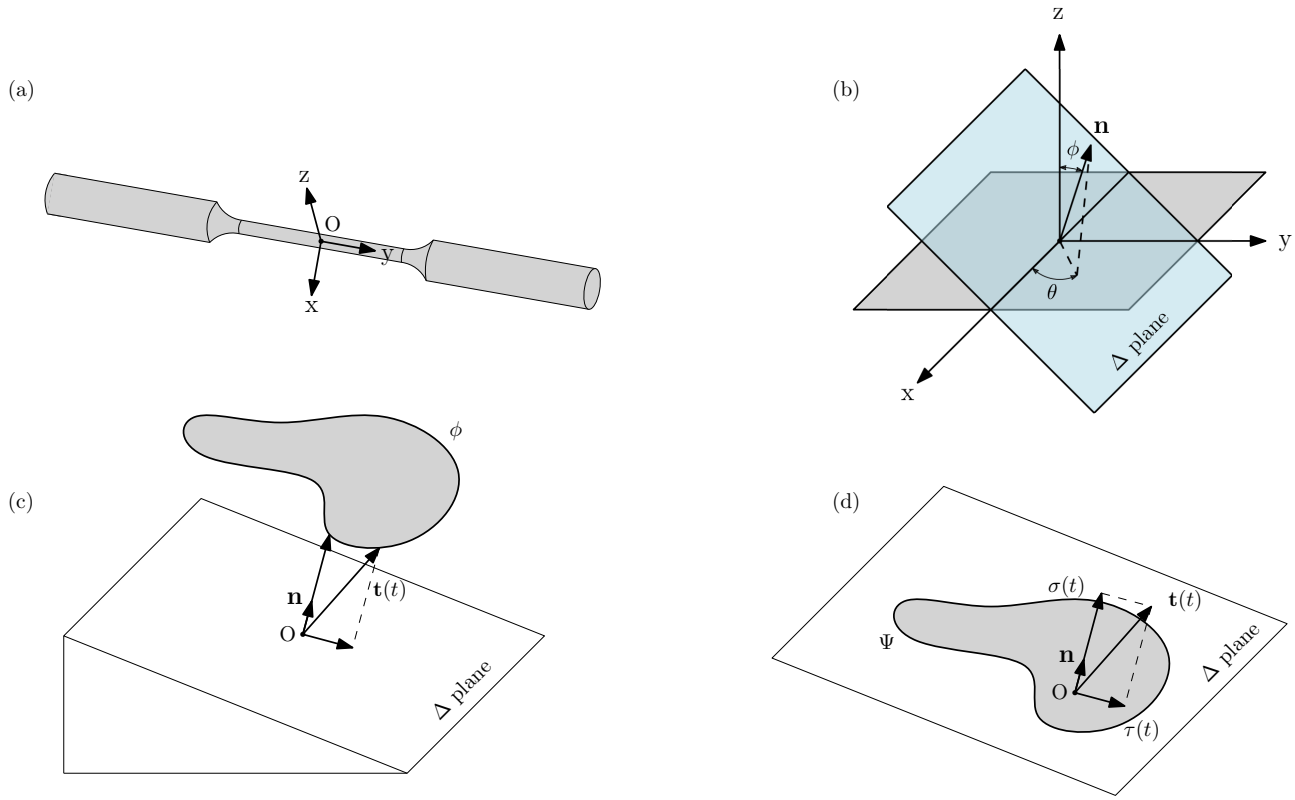

Figure 4.5 (a) Multiaxial loading. (b) Spherical coordinates. (c) Material point O. (d) Stress components in a material plane δ [114].

Normal stress Most multiaxial models use normal and shear stresses acting on material plane. Normal component can be characterised by maximum value, $\sigma_{n,max}$, minimum value $\sigma_{n,min}$, amplitude σ_a, or mean value σ_{mean} (Tab. 4.1).

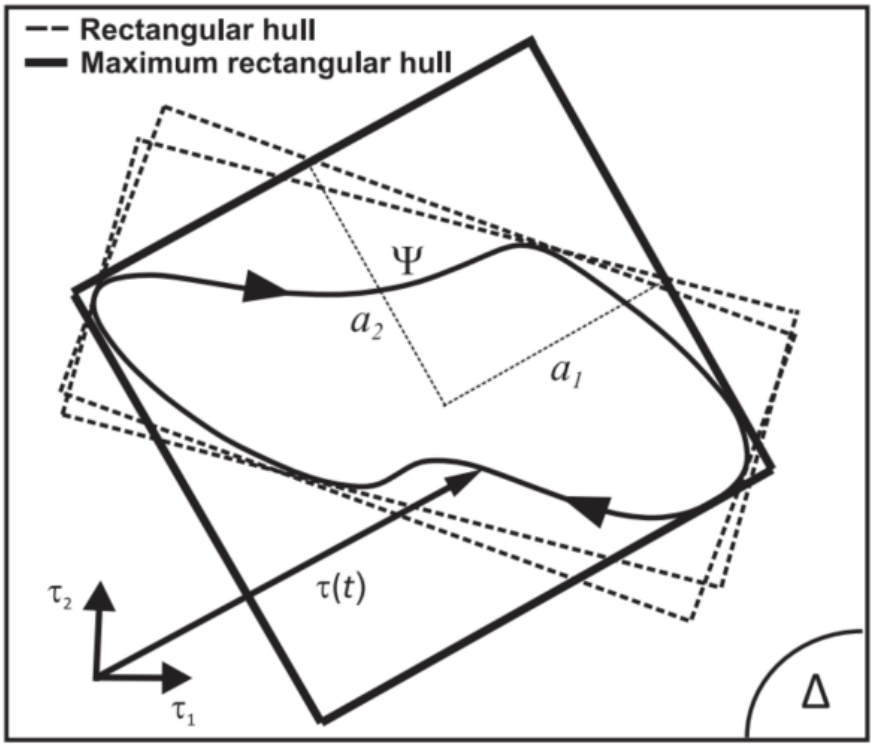

Figure 4.6 MRH [114].

Table 4.1 Constant cyclic loading - definitions.

Stress amplitude	$\sigma_a = \frac{\sigma_{max}-\sigma_{min}}{2}$
Mean stress	$\sigma_m = \frac{\sigma_{max}+\sigma_{min}}{2}$
Stress variation	$\Delta\sigma = \sigma_{max} - \sigma_{min}$
Load ratio	$R = \frac{\sigma_{max}}{\sigma_{min}}$

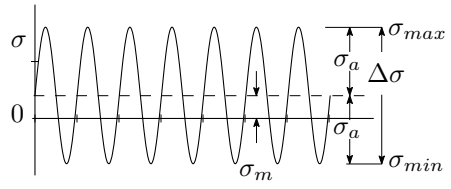

Shear stress Many techniques are available for computing the equivalent shear stress amplitude, but the most used was proposed by Dang [41] and Papadopoulos [116]. In this method, τ_a is defined as the radius of the minimum circle circumscribing (MCC) the shear stress vector path Ψ. Detailed references are found in [41, 116, 117].

In this work, Maximum Rectangular Hull (MRH) was chosen for computing shear stress amplitude. Araújo et al. [114] made a time comparison between MCC and MRH methods and the former was approximately 5x slower to compute. An overview of the MRH method is given next.

Shear stress amplitude is given by the Maximum Rectangular Hull of the shear stress vector path Ψ in a material plane Δ. The main idea is to generate rectangular hulls circumscribing the vector path using a rotation ϕ. Every rectangular hull can be defined by its half sides a_1 and a_2.

$$a_i(\phi) = \frac{1}{2}[\max \tau_i(\phi,t) - min\tau_i(\phi,t)] \tag{4.1}$$

and

$$\tau_a(\phi) = \max \sqrt{a_1^2(\phi) + a_2^2(\phi)}. \tag{4.2}$$

4.2.2 Fatemi-Socie

Althought there are others criteria such as Modified Wöhler Curve Method [118], Smith-Watson-Topper [119], the Fatemi-Socie criterion was chosen based on previous works. Doca et al. [120] used the Fatemi-Socie criterion for estimating fatigue life and obtained good results.

Fatemi and Socie [121] proposed a modification to Brown and Miller's approach to predict multiaxial fatigue life. They take into consideration the maximum shear strain amplitude (τ_a) and the maximum normal stress ($\sigma_{n,max}$) on the maximum shear strain amplitude plane. Their justification is that they observed fatigue cracks initiate on the maximum shear strain planes in different loading situations.

$$\gamma_{max}\left(1 + k\frac{\sigma_{n,max}}{\sigma_y}\right) = constant \tag{4.3}$$

where the constant is known as the FS parameter. Considering an elastic regime, it can be rewritten as:

$$FS = \frac{\tau_a}{G}\left(1 + k\frac{\sigma_{n,max}}{\sigma_y}\right) \tag{4.4}$$

where G is the shear modulus, σ_y is the yield stress and k is a constant obtained from uniaxial and torsional fatigue tests.

4.2.3 Life estimation

Fatigue life predictions are based on stress equivalent/stress invariants, integral or critical plane. The latter has advantages and sometimes the critical plane is assumed to be the one under the greatest shear stress amplitude. A drawback is that defining an amplitude for a multiaxial stresses state is not straightforward.Araújo et al. [114] proposed a method for computing τ_a called the Maximum

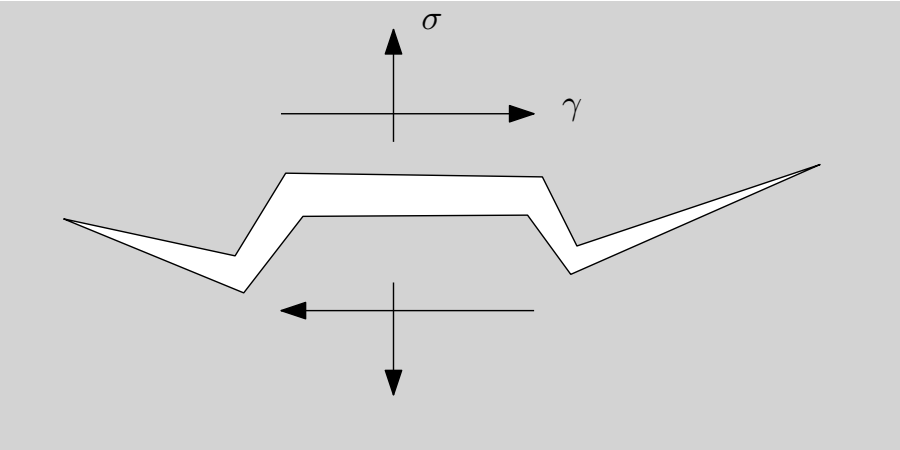

Figure 4.7 Fatemi and Socie failure model.

Rectangular Hull (MRH), so the shear stress amplitude τ_a and the maximum normal stress $\sigma_{n,max}$ can be computed.

$$FS = A\left[N_{est}\right]^b, \tag{4.5}$$

where N_{est} is the estimated number of cycles to failure.

For obtaining A and b parameters, V-notched specimens under elastic strains are tested for fatigue life. Hence, a relationship between experimental lives and the effective stress can be determined via the S-N curve. Both parameters can be obtained from fully reversed uniaxial loading (A_σ and b_σ) and another from fully reversed torsional loading (A_τ and b_τ). After, a numerical method is applied to identify the distance (L) in which the effective stress occurs. The final results are two modified $L-Nf$ curves.

$$L_\sigma = A_\sigma [N_f]^{b_\sigma}, \tag{4.6}$$

and

$$L_\tau = A_\tau [N_f]^{b_\tau}. \tag{4.7}$$

Lastly, an equivalent critical distance, L_{eq}, can be obtained from the combination of both loads as

$$L_{eq} = w_\sigma L_\sigma + w_\tau L_\tau. \tag{4.8}$$

Finally, the estimated number of cycles is

$$N_{est} = e^{\frac{\ln \frac{FS}{A}}{b}}. \tag{4.9}$$

4.3 Fretting fatigue problem setup

One of the problems that are going to be presented in the results chapter is the modelling of a fretting fatigue experiment. It is a symmetrical problem in the y-axis and the upper part is shown in Fig. 4.8.

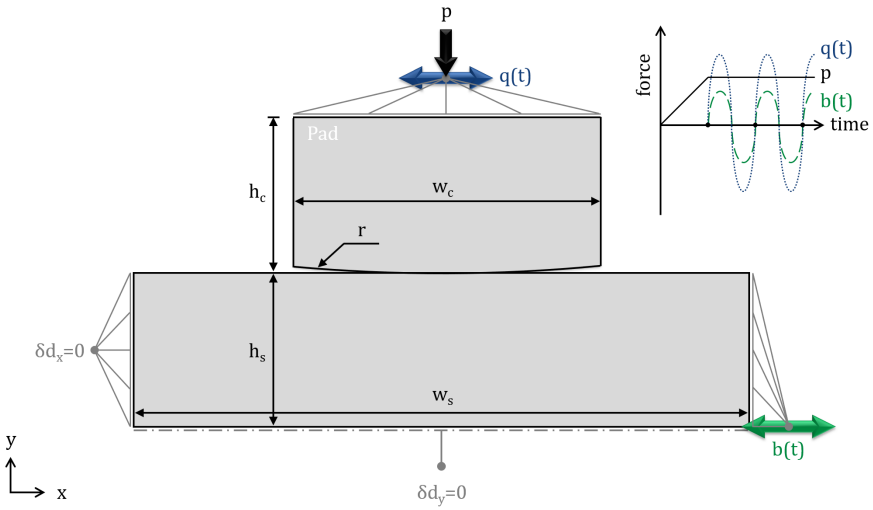

Figure 4.8 Two-dimensioanl schematic representation of the fretting fatigue problem [120].

The dimensions of the cylindrical pad are: width (w_c) of 13 mm, height (h_c) of 6.5 mm, and radius (r) of 70 mm. The specimen's dimensions are width (w_s) of 13 mm, and height (h_s) of 6.5 mm. Both are 13 mm thick. The specimen is fixed in its left side (x-direction) and on its bottom (y-direction due to symmetry). Three loads are applied in a quasi-static condition. Firstly, a compression load (p) is applied to establish the initial contact interface. Then, a shear load ($q(t)$), and a bulk load ($b(t)$) are incrementally applied in-phase in a sinusoidal function. Two different materials are modelled with this setup: Al7050-T7451 [122] and a Ti-6Al-4V [123]. Properties and loads are shown in Tab 4.2.

Table 4.2 Properties and loading conditions for the chosen material configurations [120].

	Al7050-T7451	Ti-6Al-4V
Elastic modulus, E(GPa)	73.4	120.0
Shear modulus, G(GPa)	26.9	46.5
Poisson's coefficient, ν	0.33	0.29
Yield stress, σ_y(MPa)	453.8	910.2
Normal stress sensitivity coefficient, k	1.00	1.00
Uniaxial strength parameter, A_σ	0.2041	0.1438
Torsional strength parameter, A_τ	0.1784	0.1033
Uniaxial coefficient, b_σ	-0.00314	-0.00281
Torsional coefficient, b_τ	0.06359	0.03812
Friction coefficient, μ	0.60	0.50
Constant normal force, p(N)	5800	10910
Mean shear force, q_m(N)	0	0
Shear force amplitude, q_a(N)	2300	2346
Mean bulk force, b_m(N)	0	585
Bulk force amplitude, b_a(N)	741	585

5 Integral Equation Formulation

Early works on integral equations as [124] on potential problems and [79] on elastic problems are essential BEM. Numerous studies have been conducted since then. For example,Muskhelishvili [81] and Mikhlin [125] contributed to the elasticity theory. [83] applied integral equations to solve problems in two-dimensional elasticity, while [82] extended it to three-dimensional elasticity. The term BEM first appeared in [126]. The following sections describe the BEM and its mathematical formulations. More details can be found in [127] and [88].

5.1 Elasticity

There are many methods to derive the BEM formulations such as the reciprocal theorem, the weighted residuals method, among others. In this work, the reciprocal theorem is used. An elasticity problem may be represented as in Figure 5.1. It can have two different types of boundary conditions, i.e., in Γ_u displacements are known and in Γ_t, tractions are known.

$$\int_{\Gamma} t_i d\Gamma + \int_{\Omega} b_i d\Omega = 0 \tag{5.1}$$

where t_i are tractions and b_i are body forces. Equation (5.1) have both volume and boundary integrals, but we aim to reach an expression with boundary integral only. Therefore, it is possible to make use of Green's theorem, which transforms a volume integral into a boundary one. Applying the theorem:

$$\int_{\Omega} g_{i,i} d\Omega = \int_{\Gamma} g_i n_i d\Gamma \tag{5.2}$$

Also, using Cauchy's stress tensor, which relates a unit-length vector n_i to the stress vector t_i across an imaginary surface perpendicular to n_i:

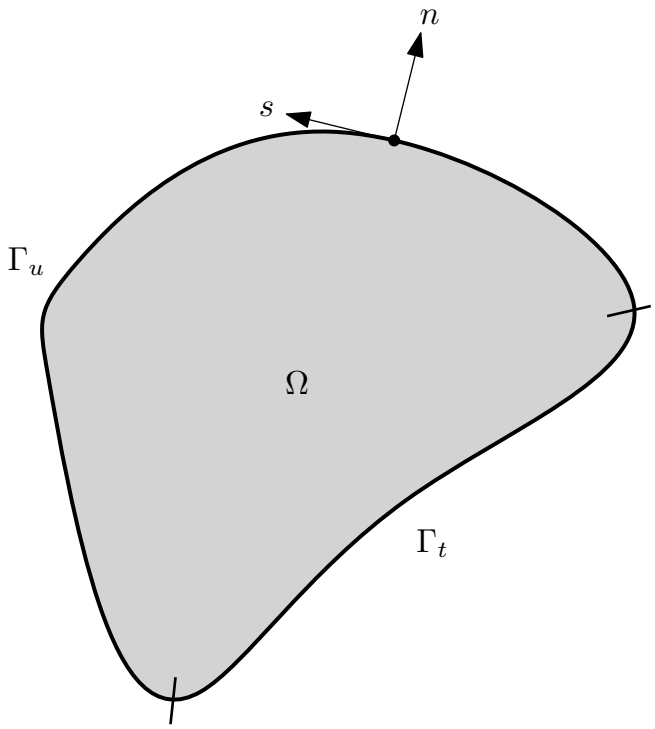

Figure 5.1 Definition of domain.

$$t_i = \sigma_{ij} n_i \tag{5.3}$$

where $\sigma_{ij} n_i$ are the components of the stress tensor.

The static equilibrium equation can now be written more conveniently as:

$$\int_\Omega \sigma_{ij,j} d\Omega + \int_\Omega b_i d\Omega = 0. \tag{5.4}$$

5.1.1 Maxwell-Betti reciprocal work theorem

As previously stated, the Maxwell-Betti reciprocal work theorem is used for deriving the boundary element formulation for elastostatics in the present work. Betti's theorem is based on the virtual work principle and it states as follows:

> The work done by a set of force acting through the displacements produced by a second set of forces, is the same as done by the second set of forces when acting through the displacements produced by the first set of forces.

In other words, given a body with two different stress-strain states, (σ_{ij}, ε_{ij}) and (σ^*_{ij}, ε^*_{ij}) is mathematically defined as:

$$\int_{\Omega} \sigma_{ij} \varepsilon^*_{ij} d\Omega = \int_{\Omega} \sigma^*_{ij} \varepsilon_{ij} d\Omega. \tag{5.5}$$

Equation (5.5) can be rewritten using deformation-displacement:

$$\varepsilon_{ij} = \frac{1}{2}(u_{i,j} + u_{j,i}) \tag{5.6}$$

as

$$\frac{1}{2}\int_{\Omega} \sigma_{ij}(u_{i,j} + u_{j,i})^* d\Omega = \frac{1}{2}\int_{\Omega} \sigma^*_{ij}(u_{i,j} + u_{j,i}) d\Omega. \tag{5.7}$$

Due to the symmetry of stress tensor, we end with:

$$\int_{\Omega} \sigma_{ij} u^*_{i,j} d\Omega = \int_{\Omega} \sigma^*_{ij} u_{i,j} d\Omega. \tag{5.8}$$

Using the product rule for derivatives

$$(\sigma_{ij} u_i)_{,j} = (\sigma_{ij})_{,j} u_i + \sigma_{ij} (u_i)_{,j} \tag{5.9}$$

the left-hand side of Eq. (5.8) becomes:

$$\int_{\Omega} \sigma_{ij} u^*_{i,j} d\Omega = \int_{\Omega} (\sigma_{ij} u^*_i)_{,j} - \sigma_{ij,j} u^*_i d\Omega. \tag{5.10}$$

Representing the second term of the right-hand side of Eq. (5.10) as a body force, as in Eq. (5.4):

$$\int_{\Omega} \sigma_{ij} u^*_{i,j} d\Omega = \int_{\Omega} (\sigma_{ij} u^*_i)_{,j} d\Omega + \int_{\Omega} b_i u^*_i d\Omega. \tag{5.11}$$

After this, it is possible to apply the divergence theorem to the first right-hand side integral:

$$\int_{\Omega} \sigma_{ij} u^*_{i,j} d\Omega = \int_{\Gamma} (\sigma_{ij} u^*_i) n_j d\Gamma + \int_{\Omega} b_i u^*_i d\Omega. \tag{5.12}$$

The final form of Maxwell-Betti reciprocal work theorem after doing the previous manipulation on both sides:

$$\int_{\Gamma}(\sigma_{ij}u_i^*)n_j d\Gamma + \int_{\Omega} b_i u_i^* d\Omega = \int_{\Gamma}(\sigma_{ij}^* u_i)n_j d\Gamma + \int_{\Omega} b_i^* u_i d\Omega. \tag{5.13}$$

and applying Cauchy's transformation given in Eq. (5.3):

$$\int_{\Gamma} t_i u_i^* d\Gamma + \int_{\Omega} b_i u_i^* d\Omega = \int_{\Gamma} t_i^* u_i d\Gamma + \int_{\Omega} b_i^* u_i d\Omega. \tag{5.14}$$

5.2 Boundary integral equation

Although Eq. (5.14) contains a domain integral, it can be transformed into a boundary integral. Let system (1) be a problem to be solved and system (2), represented by the superscript * be an arbitrary stress state used to facilitate the problem's solution. Consider an infinite elastic medium in which a unit point load e_j is applied at a point X' (system (2)), producing displacements at other points. This point load is represented by Dirac's delta that considers a body force b_i. So, applying Dirac's delta properties to the last right-hand side of Eq. (5.14), results in:

$$b_i^* = \Delta(X - X')e_i \tag{5.15}$$

where the unit vector component e_i corresponds to a unit positive force in the i direction applied at X'. Also, $X, X' \in \Omega$.

$$\int_{\Omega} b_i^* u_i \Omega = \int_{\Omega} \Delta(X - X')e_i u_i d\Omega = u_i(X')e_i. \tag{5.16}$$

Meanwhile, considering variables from system $*$ as the responses to the unit point load:

$$u_i^* = U_{ij}(X', X)e_j \tag{5.17}$$

$$t_i^* = T_{ij}(X', X)e_j \tag{5.18}$$

where Q is a point over the boundary, p is a point within the domain and U_{ij} and T_{ij} are the fundamental solutions. After substituting these terms in Eq. (5.14), the Somigliana identity for displacements is obtained:

$$u_i(X') + \int_\Gamma T_{ij}(X',x)u_j(x)d\Gamma = \int_\Gamma U_{ij}(X',x)t_j(x)d\Gamma$$

where $x \in \Gamma$.

This previous equation relates displacements at an internal point X' with displacement and traction values over the boundary. Afterwards, in Section 5.3, fundamental solutions are found.

5.3 Fundamental solutions

It is now possible to obtain Navier's equation (which are the equilibrium equations written in terms of displacements) for a unit point force applied to the body at a point X':

$$\mu u^*_{i,jj} + \frac{\mu}{1-2\nu}u^*_{j,ji} + \Delta(X-X')e_i = 0. \tag{5.19}$$

Solutions of governing equations such as 5.19 are known as *fundamental solutions* and there are a few ways to obtain a solution. Galerkin vector is often used as in [128]. A particular one of Eq. (5.19) is known as Kelvin's fundamental solution. Displacements are expressed in terms of the Galerkin vector:

$$u^*_i = G_{i,kk} - \frac{1}{2(1-\nu)}G_{k,ik}. \tag{5.20}$$

Displacement and traction fundamental solutions for 2D plane strain are given next and a detailed explanation for obtaining them can be found in [88, 128, 129].

$$U_{ij}(X',x) = \frac{1}{8\pi\mu(1-\nu)}\left\{(3-4\nu)\ln(1/r)\delta_{ij} + r_{,i}r_{,j}\right\} \tag{5.21}$$

and

$$T_{ij}(X',x) = \frac{-1}{4\pi(1-\nu)r}\left\{[(1-2\nu)\delta_{ij} + 2r_{,i}r_{,j}]\frac{\partial r}{\partial n} - (1-2\nu)(r_{,i}n_j - r_j n_i)\right\}. \tag{5.22}$$

In Eqs. (5.21) to (5.22), δ_{ij} is Kronecker's delta, $r(X',x)$ is the distance between source X' and field x points, given by:

$$r = |x' - x| \tag{5.23}$$

$$r_{,i} = \frac{\partial r}{\partial x_i}. \tag{5.24}$$

Recalling Eq. (5.2):

$$u_i(X') + \int_\Gamma T_{ij}(X',x)u_j(x)d\Gamma = \int_\Gamma U_{ij}(X',x)t_j(x)d\Gamma$$

and it contains only boundary terms, except for the first one on the left-hand side $u_i(X')$, which is an internal point. It is possible to manipulate Eq. (5.3), so that all terms will be over the boundary, in the following way. Firstly, point X' is transferred to the boundary, yielding $r \equiv 0$ and creating a singularity. Then, integration is carried out around a circle of radius ε, while making $\varepsilon \to 0$. This procedure must be done to deal with the singularity, dividing the domain in two parts - one contains a singularity, the other does not. As seen in Figure 5.2, a semicircle is centred at point x'.

$$\int_\Gamma T_{ij}(X',x)u_j(x)d\Gamma = \lim_{\varepsilon\to 0}\int_{\Gamma-\Gamma_\varepsilon} T_{ij}(x',x)u_j(x)d\Gamma + \lim_{\varepsilon\to 0}\int_{\Gamma_\varepsilon} T_{ij}(x',x)u_j(x)d\Gamma. \tag{5.25}$$

in which both limiting expressions on the right-hand side contain a strongly singular integrand of order $\mathscr{O}(r^{-1})$ in two-dimensions and $\mathscr{O}(r^{-2})$ in three-dimensions. Hence, for treating these singularities, the first integrand is evaluated in the Cauchy principle value sense, whereas the second is regularized by the first term of a Taylor series expansion of the displacements about the source point x', resulting in:

$$\lim_{\varepsilon\to 0}\int_{\Gamma_\varepsilon} T_{ij}(x',x)u_j(x)d\Gamma = \lim_{\varepsilon\to 0}\left\{\int_{\Gamma_\varepsilon} T_{ij}(x',x)\cancelto{0}{[u_j(x)-u_j(x')]}d\Gamma\right\} + u_j(x')\lim_{\varepsilon\to 0}\left\{\int_{\Gamma_\varepsilon} T_{ij}(x',x)d\Gamma\right\} \tag{5.26}$$

where the first integral on the right-hand side vanishes due to the requirement of displacement continuity. Hence, the second integral gives rise to a jump term in the displacements:

$$u_j(x')\lim_{\varepsilon\to 0}\int_{\Gamma_\varepsilon} T_{ij}(x',x)d\Gamma = \alpha_{ij}(x')u_j(x') \tag{5.27}$$

Equation (5.25) can now be written as

$$\int_\Gamma T_{ij}(x',x)u_j(x)d\Gamma = \fint_\Gamma T_{ij}(x',x)u_j(x)d\Gamma + \alpha_{ij}(x')u_j(x') \tag{5.28}$$

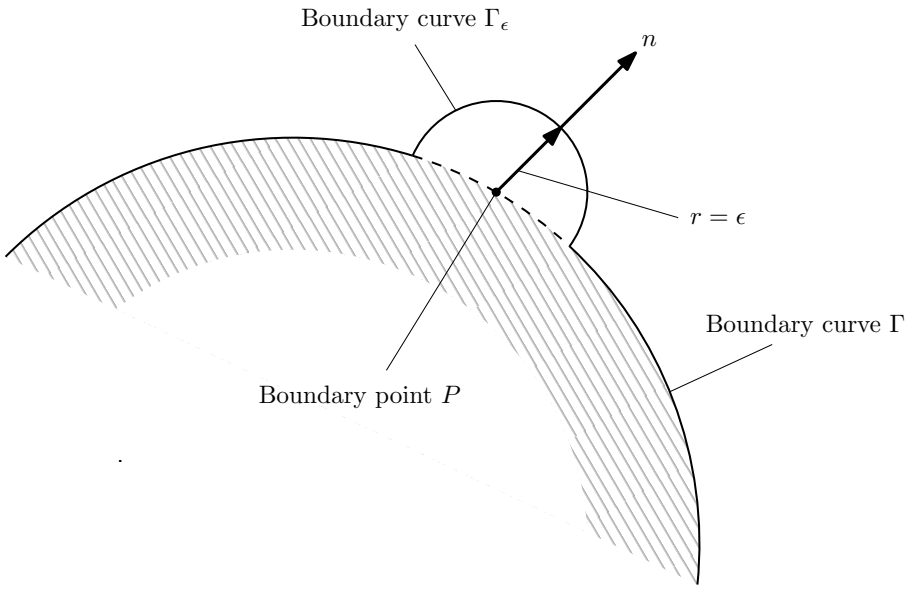

Figure 5.2 Semicircle around point P for treating the singularity.

Therefore, the displacement boundary integral equation (DBIE) can be written as:

$$C_{ij}(x')u_j(x') + \oint_\Gamma T_{ij}(x',x)u_j(x)d\Gamma = \int_\Gamma U_{ij}(x',x)t_j(x)d\Gamma + \int_\Omega U_{ij}(x',X)b_j(X)d\Gamma \tag{5.29}$$

where C_{ij} represents the jump term arising from the integration of the strongly singular kernel. It depends on the geometry and for smooth boundaries, $C_{ij} = \delta_{ij}/2$. Details on how to compute it can be found in [130].

5.4 Numerical discretisation

It is only possible to solve Eq. (5.29) analytically for simple problems, so another approach is needed if a practical problem with a complex geometry has to be modeled. The Boundary Element Method (BEM) is a numerical technique which enables the solution of boundary integral equations through a discretisation. Before introducing the concept of isogeometric BEM, it is important to show the lagrangian formulation, also used in this study for comparison. In this case, shape functions are Lagrangian polynomials and elements can be constant, linear, quadratic etc. In the next subsections, the lagrangian (conventional) formulation is presented.

5.4.1 Lagrangian formulation

First of all, the boundary is divided into elements, so that in the absence of body forces the equation becomes:

$$C_{ij}(x')u_j(x') + \sum_{n=1}^{N_e} \int_{\Gamma_n} T_{ij}(x',x)u_j(x)d\Gamma = \sum_{n=1}^{N_e} \int_{\Gamma_n} U_{ij}(x',x)t_j(x)d\Gamma \tag{5.30}$$

where $\Gamma = \sum_{n=1}^{N} \Gamma_n$.

In the lagrangian formulation, geometry x_j, unknown displacements field $u_j(x)$ and tractions field $t_j(x)$ are approximated using interpolation functions, in the following manner:

$$\begin{aligned} x_j &= \sum_{\alpha=1}^{m} N_\alpha(\xi)x_j^\alpha \\ u_j &= \sum_{\alpha=1}^{m} N_\alpha(\xi)u_j^\alpha \\ t_j &= \sum_{\alpha=1}^{m} N_\alpha(\xi)t_j^\alpha \end{aligned} \tag{5.31}$$

where N_α are the shape functions, which are polynomials of degree $m-1$. x_j^α, u_j^α and t_j^α are the values of the functions at node α. In order to make the numerical integration easier (using Gauss-Legendre), those functions are defined in terms of a dimensionless parametric coordinate system for each element $\xi \in [-1,1]$, as in Fig. 5.3:

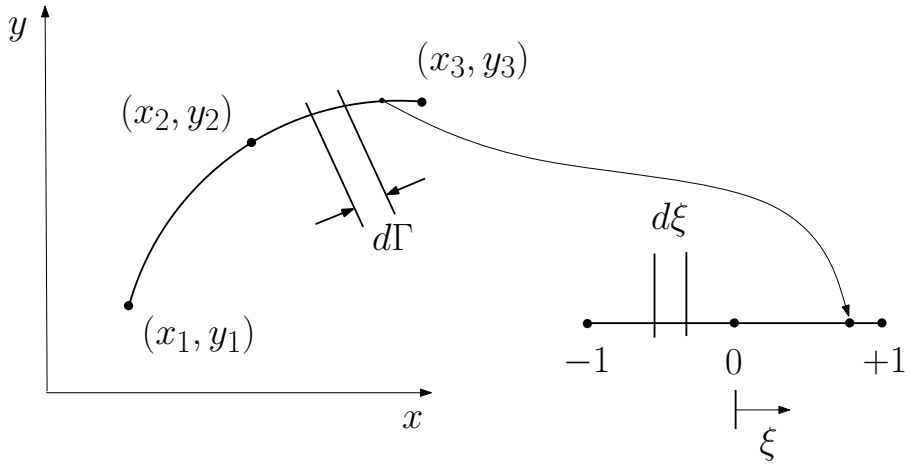

Figure 5.3 Local parametric coordinate ξ.

When using quadratic continuous elements for discretizing, geometry is approximated by a quad-

ratic function on each element. Three nodes are necessary for each element. For quadratic elements, as the ones that are used in the present work ($m = 3$), shape functions become:

$$N_1 = \frac{1}{2}\xi\,(\xi - 1) \tag{5.32}$$

$$N_2 = 1 - \xi^2 \tag{5.33}$$

$$N_3 = \frac{1}{2}\xi\,(\xi + 1) \tag{5.34}$$

The general form for defining shape functions derived from Lagrangian polynomials for degree $(m-1)$ is:

$$N_\alpha(\xi) = \prod_{i=0,\ i\neq\alpha}^{m} \frac{\xi - \xi_i}{\xi_\alpha - \xi_i} \tag{5.35}$$

Some interesting properties of the Lagrangian shape functions can be seen in books such as [128]. An important one, for example, is that the sum of the shape functions is equal to unity at a given node $\sum_\alpha^m N_\alpha = 1$.

Displacement and traction are approximated in the following way:

$$\mathbf{u} = \left\{ \begin{array}{c} u_1 \\ u_2 \\ u_3 \end{array} \right\} = \left[\begin{array}{cccccc} N_1 & 0 & N_2 & 0 & N_3 & 0 \\ 0 & N_1 & 0 & N_2 & 0 & N_3 \end{array} \right] \left\{ \begin{array}{c} u_1^1 \\ u_2^1 \\ u_1^2 \\ u_2^2 \\ u_1^3 \\ u_2^3 \end{array} \right\} = \mathbf{N}\mathbf{u}^n \tag{5.36}$$

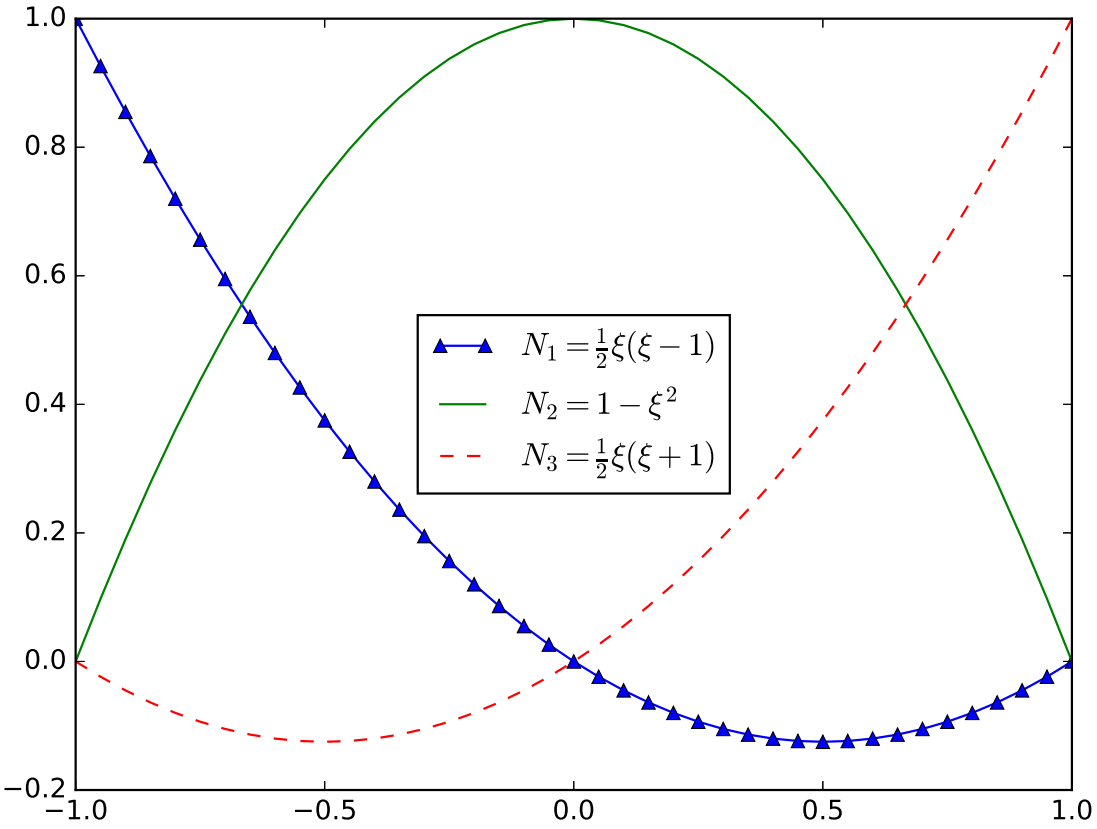

Figure 5.4 Shape functions for continuos quadratic elements.

$$\mathbf{t} = \begin{Bmatrix} t_1 \\ t_2 \\ t_3 \end{Bmatrix} = \begin{bmatrix} N_1 & 0 & N_2 & 0 & N_3 & 0 \\ 0 & N_1 & 0 & N_2 & 0 & N_3 \end{bmatrix} \begin{Bmatrix} t_1^1 \\ t_2^1 \\ t_1^2 \\ t_2^2 \\ t_1^3 \\ t_2^3 \end{Bmatrix} = \mathbf{N}\mathbf{t}^{(n)} \tag{5.37}$$

where u_i^n and t_i^n are nodal values of displacement and traction, respectively and N^i are shape functions, which are defined in Eq. (5.34) and illustrated in Fig. 5.4.

Geometry is approximated by shape functions as well:

$$\begin{Bmatrix} x_1 \\ x_2 \\ x_3 \end{Bmatrix} = \begin{bmatrix} N_1 & 0 & N_2 & 0 & N_3 & 0 \\ 0 & N_1 & 0 & N_2 & 0 & N_3 \end{bmatrix} \begin{Bmatrix} x_1^1 \\ x_2^1 \\ x_1^2 \\ x_2^2 \\ x_1^3 \\ x_2^3 \end{Bmatrix} \tag{5.38}$$

In standard boundary element, if we divide boundary Γ in N_e elements, a discretized version can be obtained:

$$C_{ij}(x')u_j(x') + \sum_{j=1}^{Ne} \int_{-1}^{1} T_{ik}^* u_i \, d\Gamma_j = \sum_{j=1}^{Ne} \int_{-1}^{1} U_{ik}^* t_j \, d\Gamma_j \tag{5.39}$$

Equation (5.39) is then applied to each node of the element, resulting in a linear algebraic equation system:

$$\mathbf{Hu} = \mathbf{Gt} \tag{5.40}$$

where **H** and **G** have values of fundamental solutions T_{ij} and U_{ij}, **t** and **u** contain traction and displacements, respectively. When dealing with a problem, often some traction and some displacement are unknowns, and by using some algebra, it is possible to isolate these unknowns in a vector **x**. Hence, Eq. (5.40) becomes:

$$\mathbf{Ax} = \mathbf{b} \tag{5.41}$$

and only one solution is possible.

5.5 Stress at internal points

For an isotropic medium internal stresses can be computed by differentiating the displacements at internal points and introducing the corresponding strains into the stress-strain relationships, i.e.:

$$\sigma_{ij} = \frac{2\mu\nu}{1-2\nu}\delta_{ij}u_{i,i} + \mu(u_{i,j} + u_{j,i}) \tag{5.42}$$

All derivatives are taken at the internal point under consideration, which is the point of application of the fundamental solution. Taking the corresponding derivatives of the fundamental solution the above equation can be written, in a compact form, as:

$$\sigma_{ij} = \int_{\Gamma} D_{kij} p_k d\Gamma - \int_{\Gamma} S_{kij} u_k d\Gamma + \int_{\Omega} D_{kij} b_k d\Omega \tag{5.43}$$

where

$$D_{kij} = \frac{1}{r^{\alpha}} \left\{ (1-2\nu) \left\{ \delta_{ki} r_{,j} + \delta_{kj} r_{,i} - \delta_{ij} r_{,k} \right\} + \beta r_{,i} r_{,j} r_{,k} \right\} \frac{1}{4\alpha\pi(1-\nu)} \tag{5.44}$$

$$\begin{aligned} S_{kij} = & \frac{2\nu}{r^{\beta}} \beta r_n (1-2\nu)\delta_{ij} r_{,k} + \nu(\delta_{ik} r_{,j} + \delta_{jk} r_{,i}) - \gamma r_{,i} r_{,j} r_{,k} + \\ & \beta\nu(n_i r_{,j} r_{,k} + n_j r_{,i} r_{,k}) + (1-2\nu)(\beta n_k r_{,i} r_{,j} + n_j \delta_{ik} + n_i \delta_{jk}) \\ & - (1-4\nu) n_k \delta_{ij} \frac{1}{4\alpha\pi(1-\nu)} \end{aligned} \tag{5.45}$$

5.6 Stress on the boundary

Although there are some ways for obtaining boundary stresses, the one used in this work is by recovering boundary tractions and displacements from BEM solution and then tangential strains are calculated using differentiation of shape functions. After applying Hooke's law and Cauchy's formula, the stresses are finally obtained.

5.6.1 Two-dimensional

First of all, a local coordinate system is defined such that e_1 is a normal unit vector and e_2 is a tangent unit vector as in and the vectors in this system can be represented as 5.5.

$$x = x_1 \mathbf{e}_1 + x_2 \mathbf{e}_2. \tag{5.46}$$

The local unit tangential vector can be obtained by

$$\mathbf{e}_1 = \mathbf{n}, \tag{5.47}$$

$$\mathbf{e}_2 = \frac{\mathbf{m}}{|\mathbf{m}|}, \tag{5.48}$$

where $\mathbf{n}$ is the normal and $\mathbf{m}$ is the tangential vector:

$$\mathbf{m} = \frac{dx(\xi)}{d\xi}. \tag{5.49}$$

The transformation matrix A for the quantities from the global to the local coordinate system is:

$$A = \begin{bmatrix} \mathbf{e}_1 \\ \mathbf{e}_2 \end{bmatrix} = \begin{bmatrix} n_1 & n_2 \\ -n_2 & n_1 \end{bmatrix} \tag{5.50}$$

We then denote displacements, tractions, strains and stresses in the local coordinates as $\hat{u}_j$, $\hat{t}_j$, $\hat{\varepsilon}_{ij}$ and $\hat{\sigma}_{ij}$, respectively. The stress tensor in the local coordinate system is

$$\hat{\sigma}_{11} = \hat{t_1} \tag{5.51}$$

$$\hat{\sigma}_{12} = \hat{t_2} \tag{5.52}$$

$$\hat{\sigma}_{22} = \frac{E}{1-\nu^2}\hat{\varepsilon}_{22} + \frac{\nu}{1-\nu}t_1 \tag{5.53}$$

where the strain is given by

$$\hat{\varepsilon}_{22} = \hat{u}_{2,2} = \frac{\partial \hat{u_2}}{\partial \xi}\frac{\partial \xi}{\partial \hat{x}_2} = A_{2j}\frac{\partial u_j}{\partial \xi}\frac{\partial \xi}{\partial \hat{x}_2} \tag{5.54}$$

and

$$\frac{\partial \xi}{\partial \hat{x}_2} = \frac{1}{|\mathbf{m}|}. \tag{5.55}$$

Finally, the stress in global Cartesian coordinate system is:

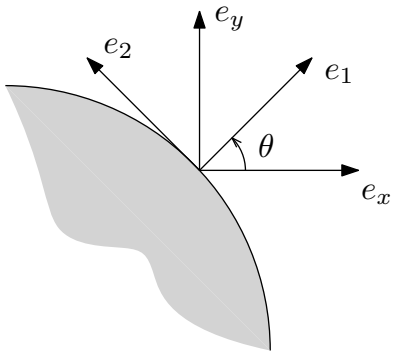

Figure 5.5 Local coordinate system.

$$\sigma_{ij} = \mathbf{A}_{ki}\mathbf{A}_{nj}\hat{\sigma}_{kn}. \tag{5.56}$$

6 NURBS - Non Uniform Rational B-Splines

Standard BEM analysis uses polynomials as basis functions, while Isogeometric Boundary Element Method (IGABEM) uses NURBS, as previously stated. Among advantages of using NURBS, is integrating with Computer Aided Design (CAD) programs, the majority of which also use NURBS. A detailed reference for understanding B-splines and NURBS is [131]. Further, works as [58] and [59] are pioneers regarding isogeometric boundary element analysis in two-dimensional elasticity. The following sections describe the basic theory for using B-splines and NURBS.

6.1 Bézier curves

Bézier curves are used in a wide variety of graphing software since they were created by Pierre Bézier in 1962, while he was working for Renault. A Bézier curve is defined as:

$$\mathbf{C}(\xi) = \sum_{i=0}^{n} B_{i,p}(\xi)\mathbf{P}_i, \ 0 \leq \xi \leq 1 \tag{6.1}$$

where $\mathbf{P}_i$ are control points and $B_{i,p}(\xi)$ are the Bernstein basis, defined as:

$$B_{i,p}(\xi) = \binom{p}{i}\xi(1-\xi)^{p-i}, \tag{6.2}$$

and $\binom{p}{i} = \frac{i!}{p!(p-i)!}$. A Bézier curve of degree p can be written as a linear combination of $p+1$ Bernstein basis.

Let $\mathbf{B}(\xi) = \{B_{i,p}(\xi)\}_{i=1}^{p+1}$ be a set of Bernstein basis functions and $\mathbf{P} = \{\mathbf{P}_i\}_{i=1}^{p+1}$ its corresponding set of control points, which are defined as $\mathbf{P}_i \in \mathbb{R}^d$ where $d = 2,3$ for two and three-dimensional problems, respectively. $\mathbf{P}$ is defined as a matrix of dimensions $(p+1) \times d$:

$$\mathbf{P} = \begin{bmatrix} P_1^1 & P_1^2 & \dots & P_1^d \\ P_2^1 & P_2^2 & \dots & P_2^d \\ \vdots & \vdots & \dots & \vdots \\ P_{p+1}^1 & P_{p+1}^2 & \dots & P_{p+1}^d \end{bmatrix} \tag{6.3}$$

An example is in Fig. 6.1, with the set of control points defined in Eq. (6.4). One can note that, as there are four control points (and therefore $p+1=4$), the degree of this curve is $p=3$.

$$\mathbf{P} = \begin{bmatrix} 1.0 & 5.0 \\ 5.0 & 4.0 \\ 2.0 & 1.0 \\ 7.0 & -1.0 \end{bmatrix} \tag{6.4}$$

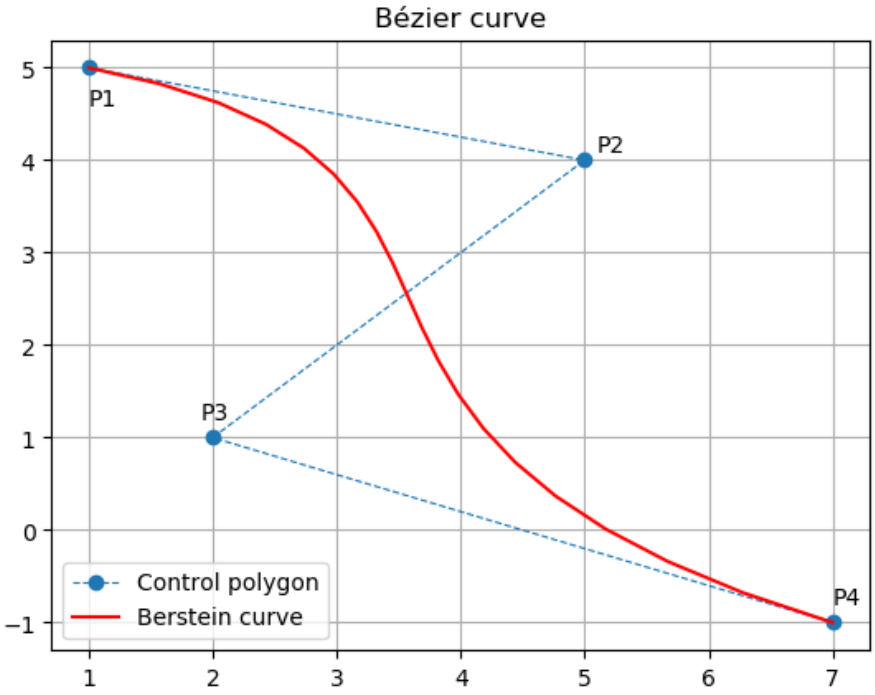

Figure 6.1 A cubic Bézier curve.

6.2 B-Splines

Defining a knot vector is an important step for understanding B-splines and NURBS. Let $\Xi = \{\xi_0, \xi, \cdots, \xi_{n+p}\}$ be a non-decreasing sequence of coordinates defined in the parameter space, i.e.,

$\xi_i \leq \xi_{i+1}$, where ξ_i is called *knot*, Ξ is the *knot vector* and n is the number of basis functions. B-spline basis functions of degree p are recursively defined using Cox-de Boor recursive formula, starting with basis of order $p = 0$:

$$N_{i,0}(\xi) = \begin{cases} 1, & \text{if } \xi_i \leq \xi < \xi_{i+1} \\ 0, & \text{otherwise} \end{cases}, \tag{6.5}$$

and for higher p degrees as:

$$N_{i,p}(\xi) = \frac{\xi - \xi_i}{\xi_{i+p} - \xi_i} N_{i,p-1}(\xi) + \frac{\xi_{i+p+1} - \xi}{\xi_{i+p+1} - \xi_{i+1}} N_{i+1,p-1}(\xi) \tag{6.6}$$

Using the previously defined basis functions, a B-spline curve $\mathbf{C}(\xi)$ is defined as:

$$\mathbf{C}(\xi) = \sum_{i=1}^{n} N_{i,p}(\xi)\mathbf{P}_i \tag{6.7}$$

where $N_{i,p}$ is the i-th basis function of degree p and $\mathbf{P}_i$ are the control points.

The number of non-zero spans in Ξ defines the number of segments of the B-spline. Each segment is influenced by $p+1$ control points. Thus, when ξ enters in a new span, a new control point is activated, while an old is deactivated. The number of knots $m+1$, the number of control points $n+1$, and the degree of the curve p, are related as $m = n + p + 1$.

6.3 NURBS

In this part, NURBS and their benefits over B-splines are presented. B-splines can be thought of as a special case of NURBS, when the latter has all weights equal to one. Probably the most evident gain of using NURBS instead of B-splines is exactly modeling circles or ellipsoids, which can only be approximated by the latter. In order to create a NURBS from a set of control points $\mathbf{P}$ using NURBS, we use:

$$\mathbf{C}(\xi) = \sum_{i=1}^{n} R_{i,p}(\xi)\mathbf{P}_i, \tag{6.8}$$

where $R_{i,p}$ are defined as:

$$R_{i,p}(\xi) = \frac{N_{i,p}(\xi)w_i}{W(\xi)} \tag{6.9}$$

where $W(\xi) = \sum_{j=1}^{n} N_{j,p}(\xi)w_j$.

Not only NURBS basis functions are important for IGABEM implementation, but also their derivatives, as they are required for approximating unknown fields. The derivative of Eq. (6.9) is defined as:

$$\frac{dR_{i,p}(\xi)}{d\xi} = w_i \frac{W(\xi)N'_{i,p} - W'(\xi)N_{i,p}(\xi)}{W(\xi)^2}, \tag{6.10}$$

where

$$W(\xi) = \sum_{j=1}^{n} N_{j,p}(\xi)w_j, \tag{6.11}$$

$$N'_{i,p} \equiv \frac{dN_{i,p}}{d\xi}, \tag{6.12}$$

and

$$W'(\xi) = \sum_{j=1}^{n} N'_{i,p}(\xi)w_i. \tag{6.13}$$

6.3.1 NURBS derivative

A derivative of a B-spline basis function, as in Eq. (6.6), can be calculated as:

$$\frac{\partial N_{i,k}(t)}{\partial t} = \frac{k}{t_{i+k} - t_i} N_{i,k-1}(t) - \frac{k}{t_{i+k+1} - t_{i+1}} N_{i+,k-1}(t). \tag{6.14}$$

Substituting Eq. (6.14) in Eq. (6.7), the result is:

$$\frac{\partial P(t)}{\partial t} = \sum_{i=0}^{n-1} N_{i+1,k-1}(t)Q_i, \tag{6.15}$$

where Q_i is defined as:

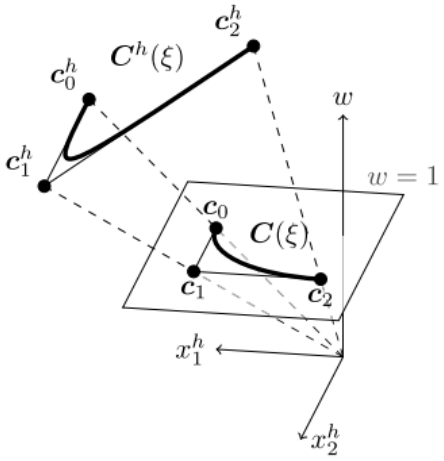

a) Perspective mapping of a quadratic B-spline $\mathbf{C}^h(\xi)$ curve in homogenuous form $\mathbb{R}^3$ to a circular arc $C(\xi)$ in model space $\mathbb{R}^2$ [132].

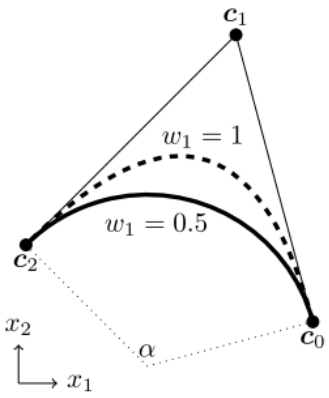

b) Effect of modified weights w_i in model space: a B-spline curve (dashed) where all weights are 1 and a NURBS curve (solid) with $w_1 = \cos(\alpha/2)$ to define a circular arc with opening angle $\alpha = 120^\circ$ [132].

Figure 6.2 Homogenuous coordinates.

$$Q_i = \sum_{i=0}^{n-1} \frac{k}{t_{i+k+1} - t_{i+1}} (P_{i+1} - P_i). \tag{6.16}$$

It is clear that a derivative of a k-order B-spline is also a B-spline, though with order $k-1$ with new control points Q_i. This is a useful feature, enabling the approach used in a curve to be also used in its derivative.

Homogeneous coordinates is the most convenient way of representing a NURBS curve and it can be seen in Figs. 6.2a and 6.2b. This coordinate system is created by adding an extra dimension to control points, called weights:

$$\mathbf{P}^h = [P_x w \; P_y w \; w] \tag{6.17}$$

where $\mathbf{P}^h$ is the control point represented in homogeneous coordinates.

6.3.2 Knot insertion

A characteristic that stands out when dealing with NURBS is the possibility of inserting knots in a knot vector without changing the original geometry. For each inserted knot, a new control point must also be created. When adding a new knot $\bar{t}$ to the knot vector, the following control point is generated:

$$\bar{B}_i = \begin{cases} B_1 & \text{if } i = 1, \\ \alpha B_i + (1-\alpha) B_{i-1} & \text{if } 1 \leq i \leq m, \\ B_n & \text{if } i = m, \end{cases} \tag{6.18}$$

where

$$\alpha = \begin{cases} 1 & \text{if } i = 1, \\ \frac{\bar{t} - t_i}{t_{i+p} - \varepsilon_i} & \text{if } 1 \leq i \leq m, \\ 0 & \text{if } i = m. \end{cases} \tag{6.19}$$

Nodal value may be inserted multiple times, but the continuity of basis functions is reduced by one for each repeated knot. However, when defining the new control point as in Eqs. (6.18) and (6.19) the continuity of the curve is kept. This process is used for Bézier extraction, which is described in the following section.

6.3.3 Bézier decomposition/extraction

Bézier extraction is an approach defined in [133] which facilitates implementing IGA in an existing FEM or BEM code. Although being used here with NURBS, it can also be used with T-splines [134]. The main idea of Bézier decomposition is to perform repeated knot insertion on all interior knots of a knot vector until they have a multiplicity of p [133]. The so-called Bézier extraction operator maps the Bernstein basis functions onto a B-spline. For each inserted knot, the continuity of basis function is reduced while the curve itself remains unchanged. The resulting basis is decomposed in a set of Bézier elements in which every element corresponds to a knot span in the original knot vector.

The original knot vector Ξ and its set of control points $\mathbf{P} = \{\mathbf{P_i}\}_{i=1}^{n}$ are modified by inserting $\{\bar{\xi}_1, \bar{\xi}_2, \ldots, \bar{\xi}_m\}$. Then the number of knots is now $n+m+p+1$ and the number of control points becomes $n+m$. For each newly inserted knot $\bar{\xi}_j$, we define α_i^j in order to compute the Bézier extraction operator $\mathbf{C}_j$:

$$\mathbf{C}_j = \begin{bmatrix} \alpha_1 & 1-\alpha_2 & 0 & \cdots & & & 0 \\ 0 & \alpha_2 & 1-\alpha_3 & 0 & \cdots & & 0 \\ 0 & 0 & \alpha_3 & 1-\alpha_4 & 0 & \cdots & 0 \\ \vdots & & & & & & \vdots \\ 0 & & \cdots & & & \alpha_{(n+j-1)} & 1-\alpha_{(n+j)} \end{bmatrix}. \tag{6.20}$$

Assuming $\bar{\mathbf{P}}_1 = \mathbf{P}$, new control points corresponding to the inserted knots are:

$$\bar{\mathbf{P}}_{j+1} = \mathbf{C}_j^T \bar{\mathbf{P}}_j \tag{6.21}$$

Hence, the final set of control points $\mathbf{P}^b$ is:

$$\mathbf{P}^b = \mathbf{C}^T \mathbf{P} \tag{6.22}$$

Knot insertion does not cause geometric nor parametric change to a curve, so:

$$\mathbf{C}(\xi) = \mathbf{P}^T N(\xi) = (\mathbf{P}^b)^T B(\xi) = (\mathbf{C}^T \mathbf{P})^T = \mathbf{P}^T \mathbf{C} B(\xi) \tag{6.23}$$

where $B(\xi)$ is the set of Bernstein polynomials basis functions defined by the final knot vector Ξ^b. So, this new operator $\mathbf{C}$ can be used to relate B-splines $N(\xi)$ and Bernstein $B(\xi)$ basis functions:

$$\mathbf{N}(\xi) = \mathbf{C}\mathbf{B}(\xi). \tag{6.24}$$

It is worth mentioning that the required input for computing $\mathbf{C}$ is only the knot vector, so it neither depends on control points nor basis functions.

For a better understanding of the process, Figs. 6.3a to 6.3d show every newly added control point due to a knot insertion in the knot vector and its respective change in basis functions.

The first knot vector is $\Xi_1 = \{0,0,0,\frac{1}{4},\frac{1}{2},\frac{3}{4},1,1,1\}$ and its corresponding set of control points as can be seen in Tab. 6.1. Knots $\Xi' = \{\frac{1}{4},\frac{1}{2},\frac{3}{4}\}$ are added one at a time, reaching the final knot vector $\Xi_4 = \{0,0,0,\frac{1}{4},\frac{1}{4},\frac{1}{2},\frac{1}{2},\frac{3}{4},\frac{3}{4},1,1,1\}$.

As previously mentioned, a B-spline is a special case of NURBS when all weights are equal to the unity. If that is not the case, one has to take into consideration the weights when performing the Bézier

a) 6 control points.

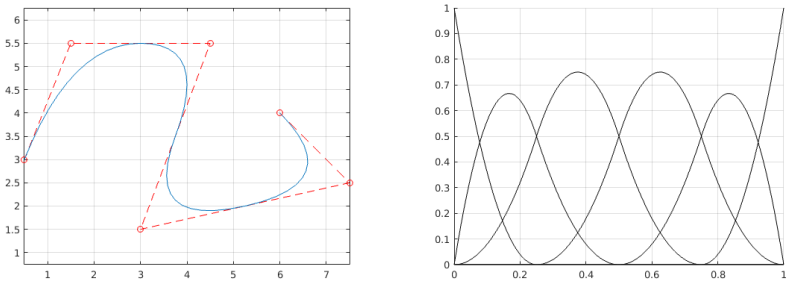

b) 7 control points.

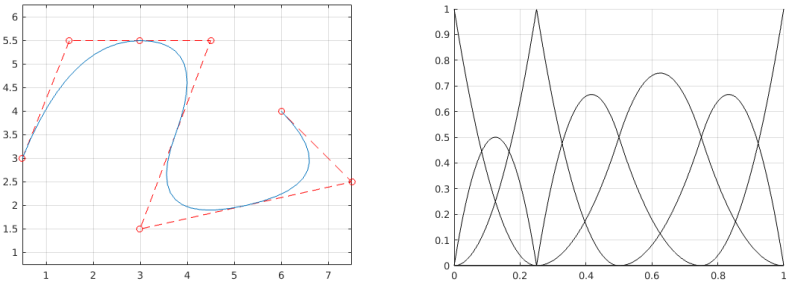

c) 8 control points.

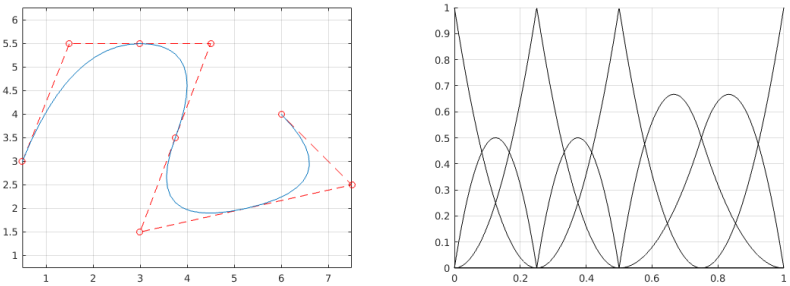

d) 9 control points.

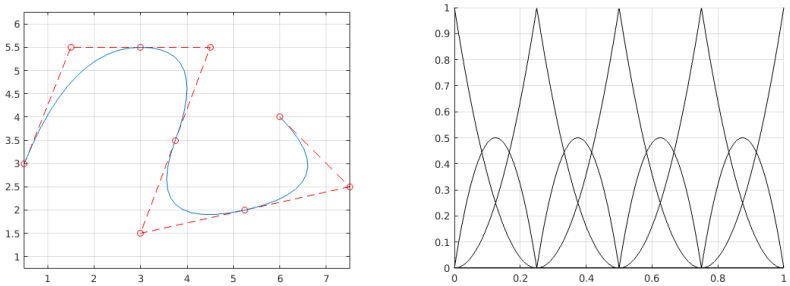

Figure 6.3 Bézier extraction process: second order curves (left) and NURBS basis functions (right) for various number of control points.

Table 6.1 Coordinates and weights of the first set of control points.

Control Point	x	y	w
1	0.5	3.0	1.0
2	1.5	5.5	1.0
3	4.5	5.5	1.0
4	3.0	1.5	1.0
5	7.5	2.5	1.0
6	6.0	4.0	1.0

Table 6.2 New control points.

Control Point	x	y	w
7	3.0	5.5	1.0
8	3.75	3.5	1.0
9	5.25	2.0	1.0

extraction. This can be done by substituting Eq. (6.24) in Eq. (6.9):

$$R(\xi) = \frac{1}{w^T \mathbf{C} B(\xi)} \mathbf{W} \mathbf{C} B(\xi) \tag{6.25}$$

where $\mathbf{W}$ is the diagonal matrix of weights as defined in [133]. Hence, the NURBS curve can be represented in terms of Bézier element as:

$$C(\xi) = \mathbf{P}^T R(\xi) \tag{6.26}$$

$$= \frac{1}{w^T \mathbf{C} B(\xi)} \mathbf{P}^T \mathbf{W} \mathbf{C} B(\xi) \tag{6.27}$$

$$= \frac{1}{w^T \mathbf{C} B(\xi)} (\mathbf{C}^T \mathbf{W} \mathbf{P})^T B(\xi) \tag{6.28}$$

7 Isogeometric analysis with BEM

7.1 Introduction

Isogeometric analysis is a fairly new concept introduced by [56]. The novelty is to use the same basis as CAD, such as NURBS, to perform analysis. NURBS are smooth and, according to [133], using a smooth basis in analysis has shown computational advantages over standard finite elements in many areas. Using the aforementioned Bézier extraction operator, the isogeometric analysis can be incorporated into existing FEM or BEM codes.

7.2 Integral formulation

Now we focus on the isogeometric formulation and its differences from conventional BEM. Approaches for collocation and integration are presented as well. As previously mentioned, the main difference between IGABEM and the conventional BEM is that the former uses NURBS basis functions to approximate the geometry and unknown boundary fields. In IGABEM, the definition of element is not as straightforward as in the conventional formulation. Due to that, after discretizing the boundary, physical domain is mapped to a parameter element $[\xi_i, \xi_j]$ which is the interval between two consecutive unique knots. Then, the parameter element is linearly mapped to parent element $[-1, 1]$.

Writing geometry and unknown fields in the isoparametric fashion, it is possible to approximate them as:

$$\mathbf{x}^e(\xi) = \sum_{i=1}^{p+1} R_{i,p}(\xi)\mathbf{x}_c^e \tag{7.1}$$

$$\mathbf{u}^e(\xi) = \sum_{i=1}^{p+1} R_{i,p}(\xi)\mathbf{u}_c^e \tag{7.2}$$

$$\mathbf{t}^e(\xi) = \sum_{i=1}^{p+1} R_{i,p}(\xi)\mathbf{t}_c^e \tag{7.3}$$

where $\mathbf{x}_c^e$ is the coordinate of a control point and $\mathbf{u}_c^e$ and $\mathbf{t}_c^e$ are displacements and tractions coefficients at a control point c for the Bézier curve e, respectively. Attention is needed because those values do not have a physical meaning as the control point might lie outside of the boundary. In order to recover displacements and tractions associated with collocation points over the boundary we can do the following:

$$\mathbf{u} = \mathbf{E}\mathbf{u_c} \tag{7.4}$$

$$\mathbf{t} = \mathbf{E}\mathbf{t_c} \tag{7.5}$$

where $\mathbf{E}$ is a transformation matrix defined in [60], [61].

Hence, Eq. (5.40) can be rewritten as:

$$\mathbf{H}\mathbf{u_c} = \mathbf{G}\mathbf{t_c} \tag{7.6}$$

and then applying the transformation matrix yields:

$$\mathbf{H}\mathbf{E}^{-1}\mathbf{u} = \mathbf{G}\mathbf{E}^{-1}\mathbf{t} \tag{7.7}$$

7.3 Integration

As seen in [59], a key feature of any BEM implementation is the evaluation of the boundary integrals containing the kernels over element domains. It is well-known that both regular and singular integrands are found depending on the position of the collocation point relative to the field element. Essentially, the evaluation of BEM integrals is split into three different types described as:

1. Regular integration: the collocation point lies in an element different from the field element.

2. Nearly singular integration: the collocation point lies in an element not on but near the field element.

3. Singular integration: the collocation point lies in the field element and can be one of two types:

Strongly singular integral: T_{ij} kernel, $\mathscr{O}(1/r)$ in 2D.

Weakly singular integral: U_{ij} kernel, $\mathscr{O}(ln(1/r))$ in 2D.

This work deals with both regular and nearly singular integral in the same way, treating weak singularities with [135] scheme and strong ones with [136] Singularity Subtraction Technique (SST).

7.3.1 Weakly singular integrals

Fundamental solutions used for solving problems are singular when the source point is located within the influence domain. Because of this, the integral is singular and needs a treatment that varies with the kind of problem. When dealing with elasticity, a usual way to treat it is using rigid-body motion. Firstly, all non-singular integrals are solved for a collocation point and then rigid-body motion is applied to solve the remaining integrals. When using standard BEM with polynomials basis functions, the number of singular integrals and rigid-body motions is the same. This is true because for each collocation point and the corresponding singular element, only one basis function is non-zero, which means only one singular integral on each element. In IGABEM this is not true, because several NURBS basis functions are different from zero on collocation points. For each collocation point, k singular integrals need special treatment.

A well established method for weakly singular treatment is the one created by [135]. It consists of co-ordinate transformation based on a third degree polynomial.

$$\hat{\xi} = \frac{(\gamma-\gamma')^3+\gamma'(\gamma'^2+3)}{1+3\gamma'^2} \tag{7.8}$$

$$\xi' = \sqrt[3]{\hat{\xi}'(\hat{\xi}'^2-1)+|\hat{\xi}'^2-1|}+\sqrt[3]{\hat{\xi}'(\hat{\xi}'^2-1)+|\hat{\xi}'^2-1|+\hat{\xi}'} \tag{7.9}$$

where $\hat{\xi}'$ denotes the location of the singularity in the parent space ($\hat{\xi}' \in [-1,1]$) and γ represents the new integration variable. Hence, a jacobian of this transformation is given by:

$$d\hat{\xi} = \frac{3(\gamma-\gamma')^2}{1+3\gamma'^2}d\gamma. \tag{7.10}$$

7.3.2 Strongly singular integrals

There are some techniques to evaluate strongly singular integrals. This work uses a direct evaluation method for strongly singular integrals. As in [137], the method is semi-analytical in the sense that all singular integrations are performed analytically and the limiting process is performed exactly. Therefore, numerical integration has only to deal with regular integrals. For two-dimensional BEM, this technique is applied to an integral over a boundary element in its normalized coordinates:

$$\int_{\Gamma} K_{ij} d\Gamma = \int_{-1}^{1} T_{ij}(p,Q)\phi_a(\xi) J_n(\xi) d\xi \tag{7.11}$$

where ϕ_a is an interpolating function related to node a and J_n is the jacobian. The first step is to use a Laurent series expansion centred at η:

$$K_{ij}(\xi,\eta) = \frac{\mathbf{F}_{-1}(\eta)}{\rho} + \frac{\mathbf{F}_{-2}(\eta)}{\rho^2} + O(1) \tag{7.12}$$

where $\rho = \xi - \eta$ is the image of radius and η is the position of the source point. The final expression for an element containing the singular point is [137]:

$$\begin{aligned}\int_{\Gamma} K_{ij} d\Gamma = \int_{\Gamma} \left[K_{ij} - \left(\frac{\mathbf{F}_{-1}(\eta)}{\rho} + \frac{\mathbf{F}_{-2}(\eta)}{\rho^2} \right) \right] d\Gamma + \mathbf{F}_{-1} \log \left| \frac{1-\eta}{-1-\eta} \right| + \\ \mathbf{F}_{-2} \left(-\frac{1}{1-\eta} + \frac{1}{-1-\eta} \right)\end{aligned} \tag{7.13}$$

Adding and subtracting the first two terms of the series expansion in Eqs. (7.12) and (7.11), promoting a regular integrand and making integration straightforward. The general application of this method requires only knowing the terms of expansion F_{-1} and F_{-2}.

As in [138], for tractions in two-dimensional elastic problems:

$$F_{-1} = -\frac{1-2\nu}{4\pi(1-\nu)} [n_\alpha(p) t_\beta(p) - n_\beta(p) t_\alpha(p)] \phi_a(\eta) \tag{7.14}$$

$$F_{-2} = 0. \tag{7.15}$$

7.4 Collocation points

In conventional BEM, it is usual to collocate at the nodes. This is not possible in IGABEM, though, given that the equivalent of nodes would be control points and, as already mentioned, may not lie over the boundary. In order to overcome this, some collocation strategies are available. Among them, probably the Greville abscissae is the most used as seen in [59], [69]. In this study, we choose to use a modified version of Greville abscissae, as in [48]. Collocation points in parameter space are given by:

$$\xi_i' = \frac{\xi_{i+1} + \xi_{i+2} + \cdots + \xi_{i+p}}{p}. \tag{7.16}$$

The modification previously stated is in the first and last collocation points, which are offset to the inner part of the element and now respectively defined as (Figure 7.1):

$$\xi_1' = \xi_1 + \beta(\xi_2 - \xi_1) \tag{7.17}$$

$$\xi_n' = \xi_n + \beta(\xi_n - \xi_{n-1}) \tag{7.18}$$

where β is a shift coefficient defined in [139] and adopted as $\beta = 0.5$.

Note that only the first and last collocation points in 7.1 are different between them, while all others coincide. This is to avoid collocating twice at the same coordinate when considering an edge, which can be prejudicial to the integration.

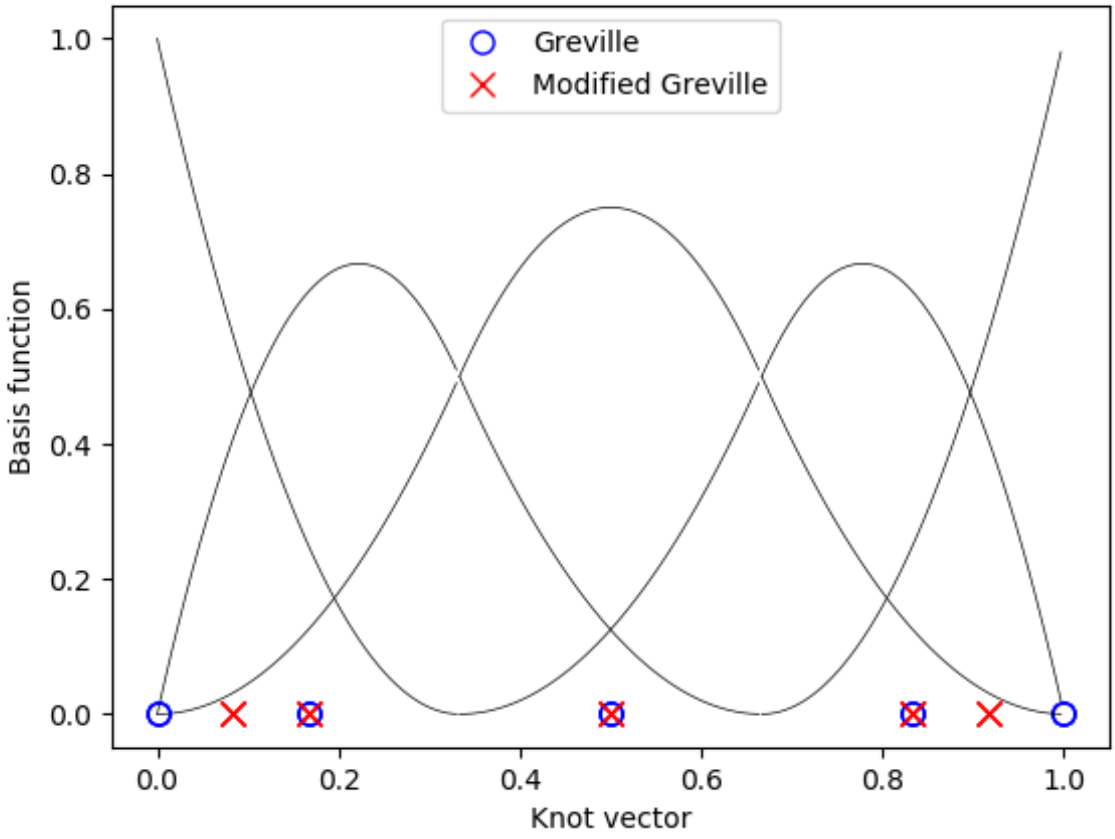

Figure 7.1 Modified Greville's abscissae.

8 Numerical modelling

Using the present formulation, problems with any number of two-dimensional bodies in contact can be analysed. In this work, however, let us consider two homogeneous isotropic linearly elastic bodies (say A and B) initially in a separate state (Fig. 8.1). Then, they come closer to each other, until there is a contact between them. It is possible to define two regions for each body, one that can be in contact $\Gamma_c^{A,B}$ and other that cannot $\Gamma_{nc}^{A,B}$. Their deformations can be described by two coupled integral equations, one for each body. As a numerical solution is desired, it makes sense to present the equations after discretization:

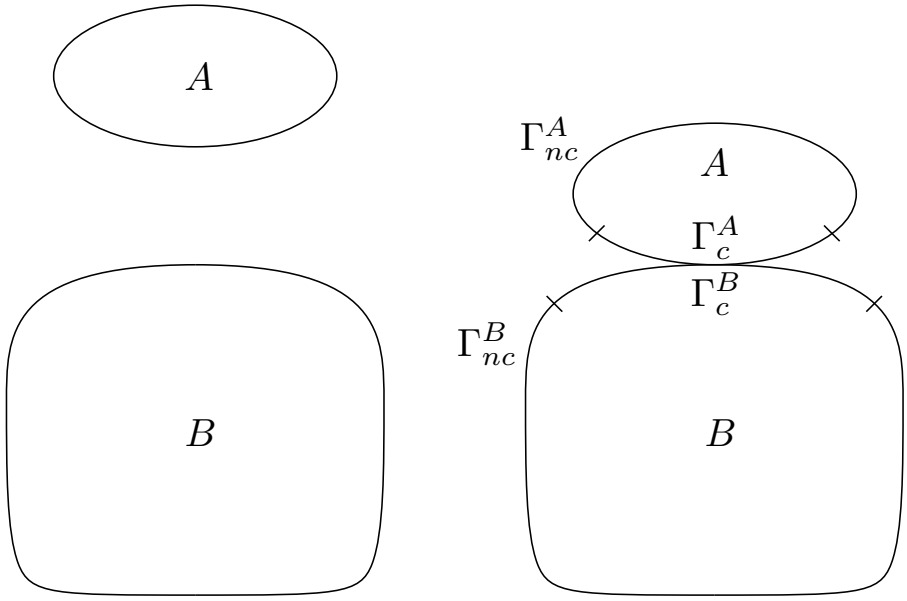

Figure 8.1 Contact and non-contact zones.

$$c_{ij}^{A} u_j^{A} + \sum_{n=1}^{NA} H_{ij}^{A} u_j^{A} = \sum_{n=1}^{NA} G_{ij}^{A} t_j^{A} \tag{8.1}$$

and similarly for body B:

$$c_{ij}^{B} u_j^{B} + \sum_{n=1}^{NB} H_{ij}^{B} u_j^{B} = \sum_{n=1}^{NB} G_{ij}^{B} t_j^{B} \tag{8.2}$$

where NA and NB are the number of nodes of bodies A and B, respectively.

Therefore, two sets of linear equations are obtained. In a matrix form, they become:

$$[H]^{\gamma}\{u\}^{\gamma} = [G]^{\gamma}\{t\}^{\gamma}\ ,\ \gamma = A,B \tag{8.3}$$

As noted by [95], for linear problems, once this system of equations has been solved, the final solution for displacements and tractions everywhere on the boundaries can be obtained. This is not the case for this study, as we are dealing with a non-linear problem. This non-linearity comes from the fact that the extend of contact region is not known *a priori* and it must be determined as part of the solution. In order to overcome this, the same approach used in [140], [141], [97] is used. It consists of an iterative method known as generalized Newton's method. The system of equations in Eq. (8.3) can be rearranged to the form:

$$\mathbf{Ax} = \mathbf{b} \tag{8.4}$$

8.1 Numerical implementation

This section presents the approaches used for modelling and solving the problem, such as constraint equations and how to consider different modes of contact. In addition, the algorithm for solving the non-linear system is also shown. In order to make the whole process clear, a flowchart depicts the main steps of the code (Fig. 8.2).

Since the contact zone of bodies A and B share nodes, they must be coupled in eq. (8.3). At this point, though, the contact width is unknown, resulting in an unbalanced system with more variables than equations. For the non-contact region, a mixed matrix containing both displacements and tractions is obtained:

$$\begin{bmatrix} \mathbf{A}_{nc}^1 & 0 & \mathbf{H}_c^1 & 0 & -\mathbf{G}_c^1 & 0 \\ 0 & \mathbf{A}_{nc}^2 & 0 & \mathbf{H}_c^2 & 0 & -\mathbf{G}_c^2 \\ 0 & 0 & \mathbf{C}_u^1 & \mathbf{C}_u^2 & \mathbf{C}_t^1 & \mathbf{C}_t^2 \end{bmatrix} \begin{Bmatrix} \mathbf{x}_{nc}^1 \\ \mathbf{x}_{nc}^2 \\ \mathbf{u}_c^1 \\ \mathbf{u}_c^2 \\ \mathbf{t}_c^1 \\ \mathbf{t}_c^2 \end{Bmatrix} = \begin{Bmatrix} \mathbf{b}^1 \\ \mathbf{b}^2 \\ \mathbf{v}^{1,2} \end{Bmatrix}. \tag{8.5}$$

The third row in matrix in Eq. (8.5) represents the contact contraints. These constraints $C_u^{1,2}$ and $C_t^{1,2}$ are respectively, displacement and traction constraints for each node-pair. They can be one of the following three:

Slip:

$$\mathbf{c}_u = \begin{bmatrix} 0 & 0 & 0 & 0 \\ 0 & 0 & 0 & 0 \\ E_l^a & 0 & E_l^b & 0 \\ 0 & 0 & 0 & 0 \end{bmatrix} \begin{Bmatrix} u_t^a \\ u_n^a \\ u_t^b \\ u_n^b \end{Bmatrix}$$

$$\mathbf{c}_t = \begin{bmatrix} E_l^a & 0 & -E_l^b & 0 \\ \pm(f \times E_l^a) & E_l^a & 0 & 0 \\ 0 & 0 & 0 & 0 \\ 0 & 0 & \pm(f \times E_l^b) & E_l^b \end{bmatrix} \begin{Bmatrix} t_t^a \\ t_n^a \\ t_t^b \\ t_n^b \end{Bmatrix}$$

Stick:

$$\mathbf{c}_u = \begin{bmatrix} 0 & 0 & 0 & 0 \\ 0 & 0 & 0 & 0 \\ E_l^a & 0 & E_l^b & 0 \\ 0 & E_l^a & 0 & E_l^b \end{bmatrix} \begin{Bmatrix} u_t^a \\ u_n^a \\ u_t^b \\ u_n^b \end{Bmatrix}$$

$$\mathbf{c}_t = \begin{bmatrix} E_l^a & 0 & -E_l^b & 0 \\ 0 & E_l^a & 0 & -E_l^b \\ 0 & 0 & 0 & 0 \\ 0 & 0 & 0 & 0 \end{bmatrix} \begin{Bmatrix} t_t^a \\ t_n^a \\ t_t^b \\ t_n^b \end{Bmatrix}$$

Separate:

$$\mathbf{c}_u = \begin{bmatrix} 0 & 0 & 0 & 0 \\ 0 & 0 & 0 & 0 \\ 0 & 0 & 0 & 0 \\ 0 & 0 & 0 & 0 \end{bmatrix} \begin{Bmatrix} u_t^a \\ u_n^a \\ u_t^b \\ u_n^b \end{Bmatrix}$$

$$\mathbf{c}_t = \begin{bmatrix} E_l^a & 0 & 0 & 0 \\ 0 & E_l^a & 0 & 0 \\ 0 & 0 & E_l^b & 0 \\ 0 & 0 & 0 & E_l^b \end{bmatrix} \begin{Bmatrix} t_t^a \\ t_n^a \\ t_t^b \\ t_n^b \end{Bmatrix}$$

where E_l are the entries of matrix E corresponding to the local segment (curves of the contact surfaces).

8.1.1 Non-linear equation solution

As Eq. (8.5) is non-linear, generalized Newton-Raphson's method was used as in [142]. It is an iterative technique that requires an initial guess $\mathbf{x}_{k-1}$ to find an approximated solution of $\mathbf{x}$ as follows. Given an initial value for the vector (say $\mathbf{x}_0$), we need to find a $\Delta\mathbf{x}_0$ such that $\mathbf{f}(\mathbf{x}_0 + \Delta\mathbf{x}_0) = 0$. Using the first-order Taylor series, it can be approximated as:

$$\mathbf{f}(\mathbf{x}_0 + \Delta\mathbf{x}_0) \approx \mathbf{f}(\mathbf{x}_0) + \mathbf{J}_0\Delta\mathbf{x}_0 \tag{8.6}$$

where $\mathbf{J}$ is the $n \times n$ Jacobian. We are looking for $\mathbf{f}(\mathbf{x}_0 + \Delta\mathbf{x}_0) = 0$, so the increment $\Delta\mathbf{x_0}$ is computed as:

$$\Delta\mathbf{x}_0 \approx -[\mathbf{J}]^{-1}\mathbf{f}(\mathbf{x}_0). \tag{8.7}$$

Vector $\mathbf{x}$ is updated as:

$$\mathbf{x_k} = \mathbf{x_{k-1}} + \Delta\mathbf{x_{k-1}} \tag{8.8}$$

$$\mathbf{x}_k = \mathbf{x}_{k-1} - \mathbf{JR} \tag{8.9}$$

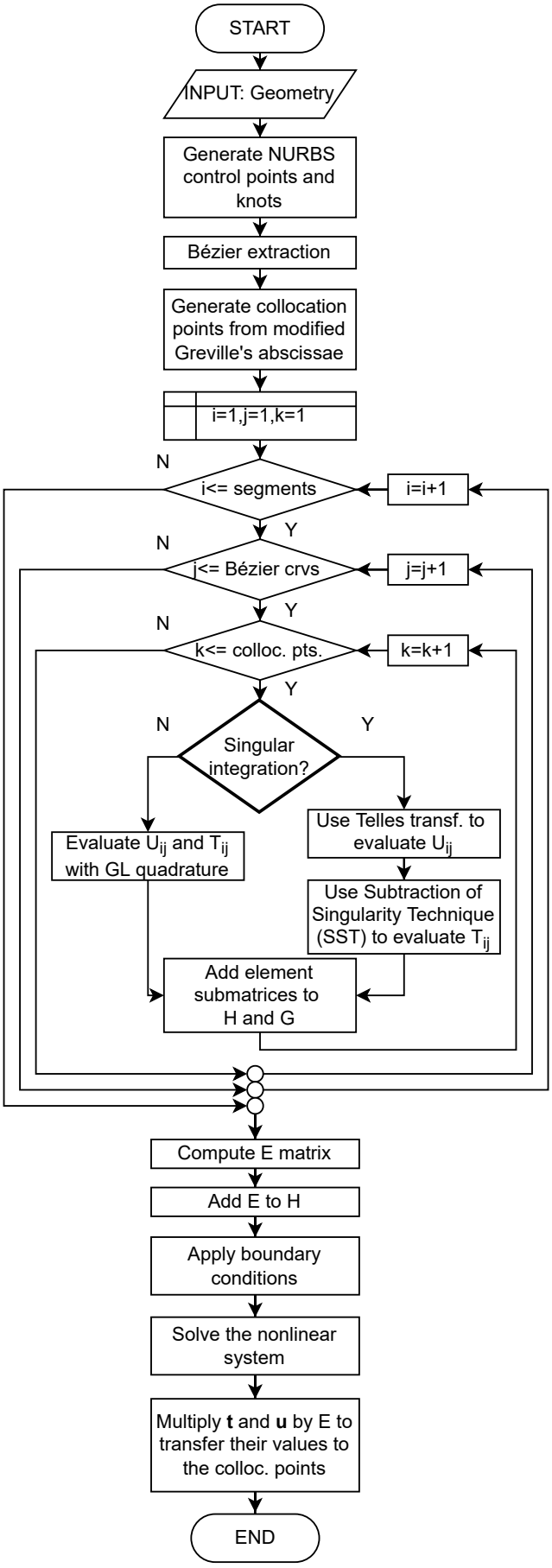

Figure 8.2 Procedure flowchart.

where $\mathbf{R}$ is the residual function. For this particular problem, we use them as defined in [140], i.e., $\mathbf{J} = \mathbf{A}^{-1}$ and $\mathbf{R} = \mathbf{A}\mathbf{x}_{k-1} - \mathbf{b}$. The process continues until the residual is smaller than a prespecified tolerance ε, defined as:

$$\varepsilon = \sqrt{(\mathbf{x}_k - \mathbf{x}_{k-1})^T (\mathbf{x}_k - \mathbf{x}_{k-1})} \tag{8.10}$$

Algorithm 1 Main code

Input Geometry, load, material properties

1: **for** i **do**12 ▷ Assemble matrices for bodies 1 and 2
2: Assemble G_i and H_i
3: Apply BC on non-contact region
4: Insert matrices A_i in A^{NL}
5: **for** i **do**1number of load steps
6: Compute the gap g_0 between node-pairs in contact zone.
7: Apply Newton-Raphson's method for solving $\mathbf{R} = \mathbf{A}\mathbf{x} - \mathbf{b}$
8: Vector $\Delta\mathbf{u}$ and $\Delta\mathbf{t}$ based on BCs and unknowns.
9: $\mathbf{u}_i = \mathbf{u}_{i-1} + \Delta\mathbf{u}$
10: $\mathbf{t}_i = \mathbf{t}_{i-1} + \Delta\mathbf{t}$

Algorithm 2 Newton-Raphson's method

Input $\mathbf{A}, \mathbf{b}, \mathbf{x}_0$

Initialize $\mathbf{x}_0$
while $R > \varepsilon$ **do**
    Assemble matrix $\mathbf{A}^{NL}$ and vector $\mathbf{b}^{NL}$
    Assemble matrix $\mathbf{A}$ and vector $\mathbf{b}$
    $\mathbf{R} = \mathbf{A}\mathbf{x} - \mathbf{b}$
    $\mathbf{d} = -\mathbf{A}^{-1}\mathbf{R}$
    $\mathbf{x} = \mathbf{x}_0 + \mathbf{d}$
    $\delta = \sqrt{(\mathbf{x}_k - \mathbf{x}_{k-1})^T(\mathbf{x}_k - \mathbf{x}_{k-1})}$
    $\mathbf{x}_0 = \mathbf{x}$
return $\mathbf{x}$

9 Results

9.1 Introduction

This chapter presents examples used for validating the code, comparing isogeometric formulation with both Standard BEM using quadratic elements and with analytical results for elastic problems. Furthermore, frictionless cases of contact problems are shown for one body in contact with a rigid half-plane and for two elastically-similar bodies. Lastly, fatigue life predictions are shown. The steps required to perform the analysis were shown in Fig. 8.2. Although similar to a standard BEM analysis, differences comprise:

1. The definition of elements is given by unique knot vector values.
2. NURBS basis functions are used instead of polynomial shape functions.
3. Collocation occurs at points defined by the modified Greville's abscissae.

9.1.1 Relative errors

In order to compare standard BEM and IGABEM accuracy, displacement and traction norms can be used for error estimation. These norms can be computed, respectively as:

$$\|\mathbf{u}\|_{L_2} = \sqrt{\int_\Gamma \sum_{i=1}^{Ne} (u_i)^2 d\Gamma} \tag{9.1}$$

and

$$\|\mathbf{t}\|_{L_2} = \sqrt{\int_\Gamma \sum_{i=1}^{Ne} (t_i)^2 d\Gamma}. \tag{9.2}$$

Hence, the relative error for $\|\mathbf{u}\|$ and $\|\mathbf{t}\|$ are, respectively:

$$\varepsilon_u = \frac{\|\mathbf{u} - \mathbf{u}^{\mathbf{exact}}\|_{L_2}}{\|\mathbf{u}^{\mathbf{exact}}\|_{L_2}} \tag{9.3}$$

$$\varepsilon_t = \frac{\|\mathbf{t} - \mathbf{t}^{\mathbf{exact}}\|_{L_2}}{\|\mathbf{t}^{\mathbf{exact}}\|_{L_2}}. \tag{9.4}$$

Mesh naming: For naming the different meshes for each method and for each problem, a name convention was used. We denote *standard* as *S*, *isogeometric* as *I*; *cylinder* as *C*, *infinite plate* as *P*, *beam* as *B*. For example, we use $SC-3$ to refer to the *third standard BEM* mesh for the *cylinder*, whereas $IP-5$ refers to the *fifth isogeometric BEM* mesh for *inifinite plate*.

9.2 Elastic problems

9.2.1 Pressurised cylinder

Thick-walled cylinders (in this work also referred as tubes) are commonly used in industry. In most of the cases, the cylinder has a constant wall thickness and is subjected to a uniform internal and/or external pressure. The isotropy assumption leads to axisymmetric deformation of the cylinder. A pressurized cylinder is the first example, with only a quarter of it being modelled (due to symmetry) as in Figs. 9.1 and 9.2. It is assumed under plane strain and 32 Gauss points are used. Geometric and material properties can be seen in Table 9.1.

Table 9.1 Geometric and material properties - tube.

Property	Symbol	Value
Inner Radius	R_a	50 mm
Outer Radius	R_b	100 mm
Young's Modulus	E	200 GPa
Poisson's ratio	ν	0.32
Pressure	P	100 N/mm

Given that this problem is axisymmetric, it is assumed that there are only radial displacements. The analytical solution for radial displacement u_r and boundary stresses σ_r and σ_θ are:

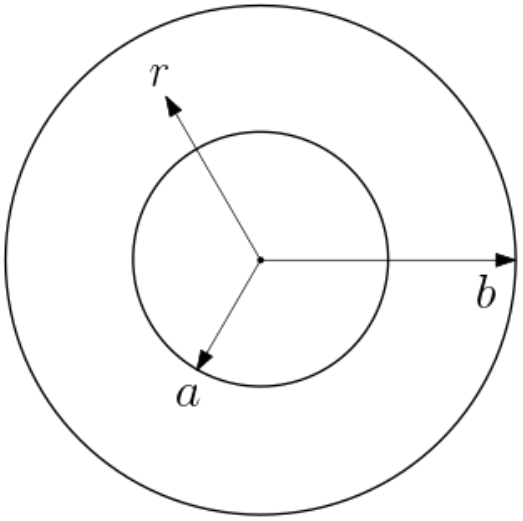

a) Radii of the cylinder.

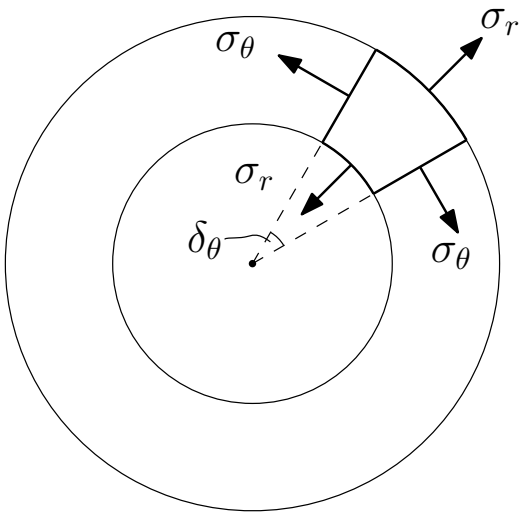

b) Internal stresses of cylinder.

Figure 9.1 Geometry of the cylinder.

$$u_r = \frac{(1+\nu)Pc^2}{2Eb^2}\left[(1-2\nu)r + \frac{b^2}{r}\right] \tag{9.5}$$

$$\sigma_r = \frac{a^2P}{b^2-a^2}\left(1-\frac{b^2}{r^2}\right) \tag{9.6}$$

$$\sigma_\theta = \frac{a^2P}{b^2-a^2}\left(1+\frac{b^2}{r^2}\right) \tag{9.7}$$

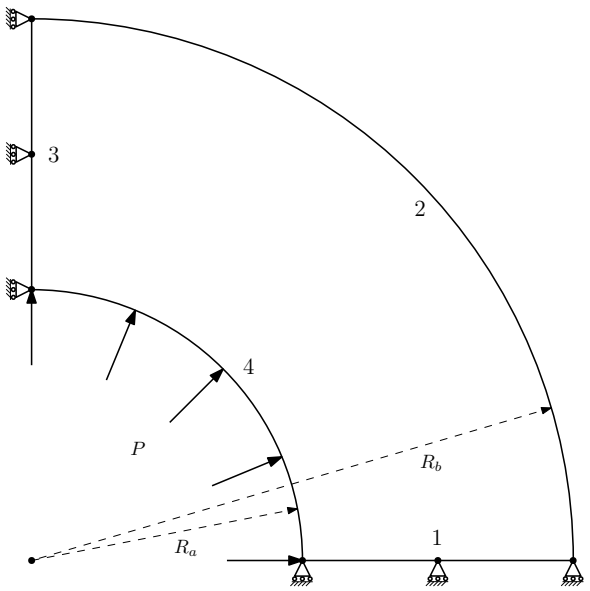

Figure 9.2 Boundary conditions of problem 1.

Lagrangian

For the standard lagrangian simulation, six different meshes were used (Table 9.2). They all used quadratic elements, with three nodes per element.

Table 9.2 Number of elements per segment for the 6 meshes - tube.

	Elem. per segment					
Mesh	1	2	3	4	**Total nodes**	**DOF**
SC-1	1	3	1	2	14	28
SC-2	2	6	2	4	28	56
SC-3	3	9	3	6	42	84
SC-4	4	12	4	8	56	112
SC-5	5	15	5	10	70	140
SC-6	10	30	10	20	140	280

Isogeometric

Isogeometric simulation, in turn, used 13 different meshes (Table 9.3). All of them used a quadratic NURBS $p = 2$, with increasing number of Bézier per segment.

Table 9.3 Number of elements per segment for the 13 meshes.

Mesh	**Bézier elem. per seg.**	**DOF**
IC-1	1	24
IC-2	2	32
IC-3	3	40
IC-4	4	48
IC-5	5	56
IC-6	10	96

Displacements and Stresses

The numerical results obtained for both displacements and stresses show good agreement with the analytical solutions. For this part of the study, only the finest mesh of each method was used, i.e., SC-6 and IC-6.

Displacements Displacements were measured for different locations over segment 1 and both methods are accurate compared to the analytical solution, as seen in Figure 9.3.

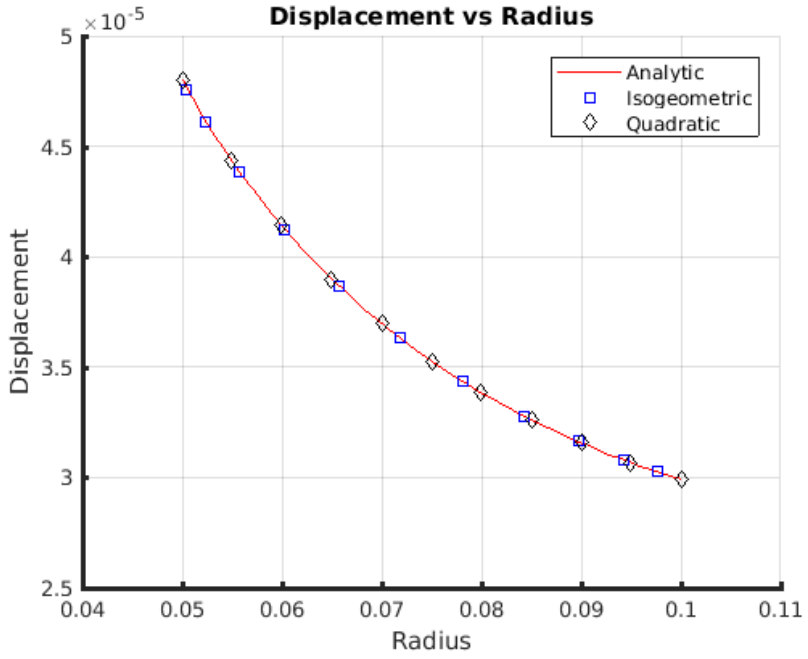

Figure 9.3 Displacements of the thick-walled tube discretization.

Stresses on the boudary Figures 9.4a and 9.4b show the results for boundary stresses along segment 1, using Standard BEM, while Fig. 9.5b illustrates the same for isogeometric BEM. Exact solutions for σ_r and σ_θ are those from Eqs. (9.6) and (9.7), respectively.

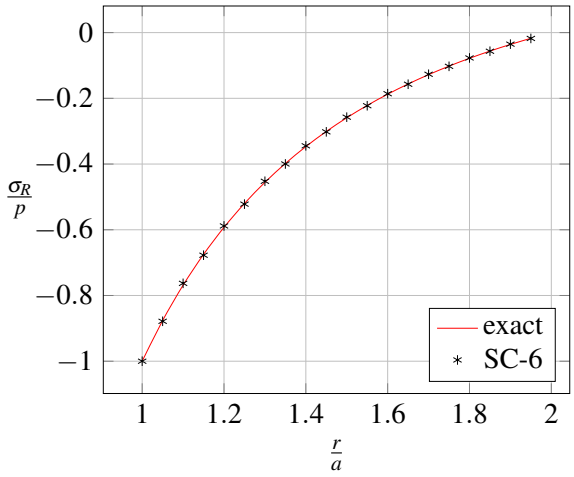

a) σ_R along segment 1.

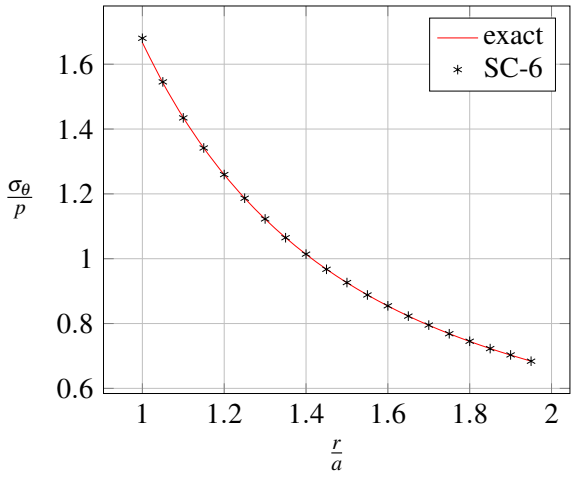

b) σ_θ along segment 1.

Figure 9.4 Boundary stress along segment 1 for standard BEM.

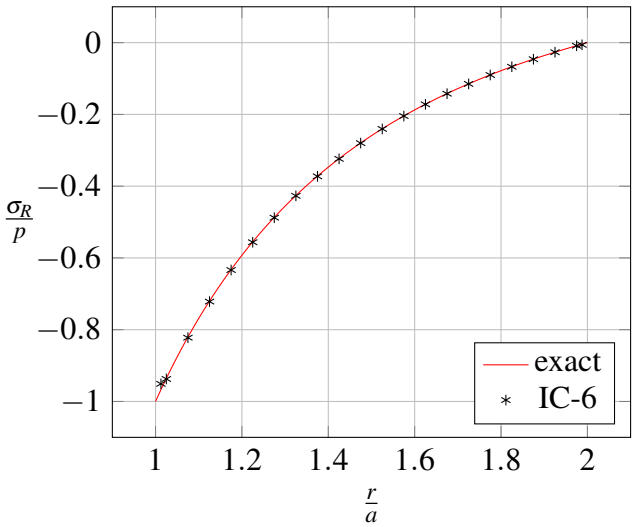

a) σ_R along segment 1.

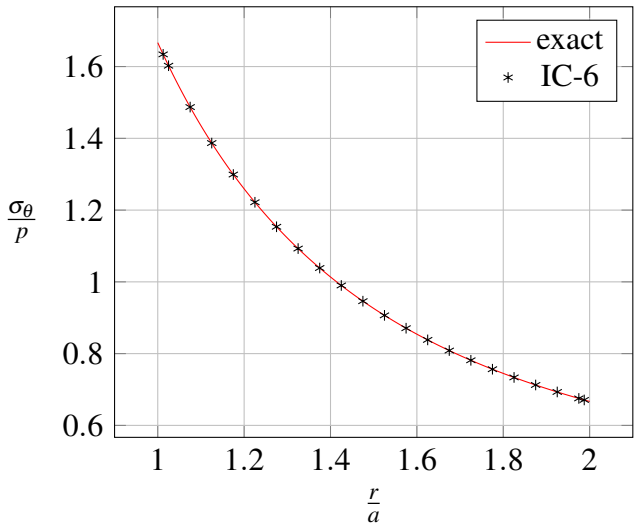

b) σ_θ along segment 1.

Figure 9.5 Boundary stress along segment 1 for IGABEM.

Stresses at internal points Stresses at internal points were also calculated for both Standard BEM and IGABEM. For comparing their results, three internal points were used (Table 9.4) and the results for stresses σ_{11}, σ_{22} and σ_{12} are in Table 9.5.

Table 9.4 Coordinates of internal points - cylinder.

Internal Point	x	y
1	0.0667	0.0333
2	0.0333	0.0667
3	0.0667	0.0667

Table 9.5 Stresses at internal points - cylinder.

	Standard			IGABEM		
Internal Point	σ_{11}	σ_{22}	σ_{12}	σ_{11}	σ_{22}	σ_{12}
1	-2.6672	69.3342	-48.0010	-2.6667	69.3336	-48.0002
2	69.3374	-2.6673	-48.0008	69.3336	-2.6667	-48.0002
3	33.3341	33.3342	-37.5009	33.3335	33.3335	-37.5001

A colour map with 154 internal points for the standard simulation is shown in Figure 9.6. Deformed configuration was also plotted as the black line.

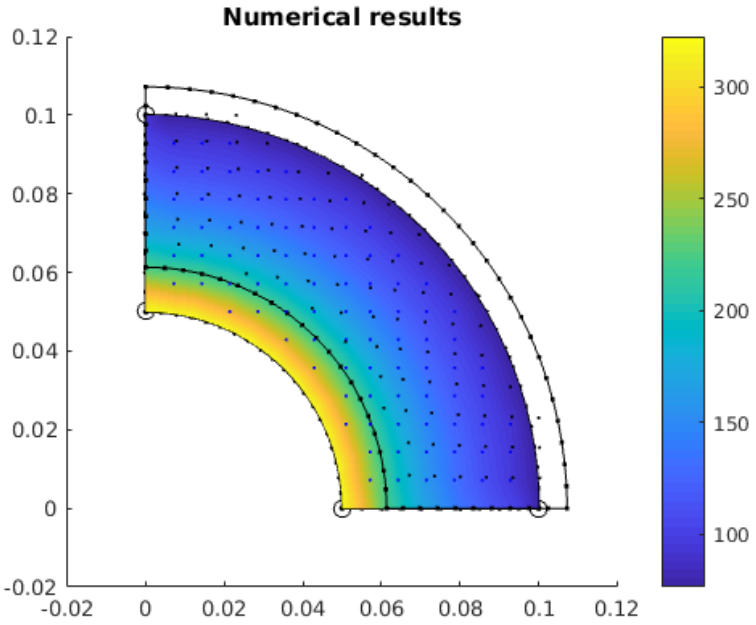

Figure 9.6 Stresses in tube - numerical results (standard).

Mesh convergence

The last comparison for this example is regarding error. A mesh convergence for IGABEM was performed for the cylinder, for radial displacements u_r and stresses σ_r and σ_θ. Results are shown in Figs. 9.7, 9.8 and 9.9.

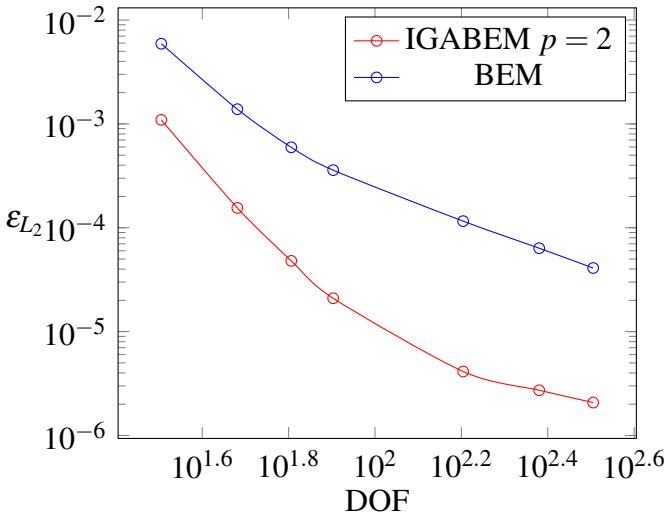

Figure 9.7 u_r relative errors vs degrees of freedom for tube.

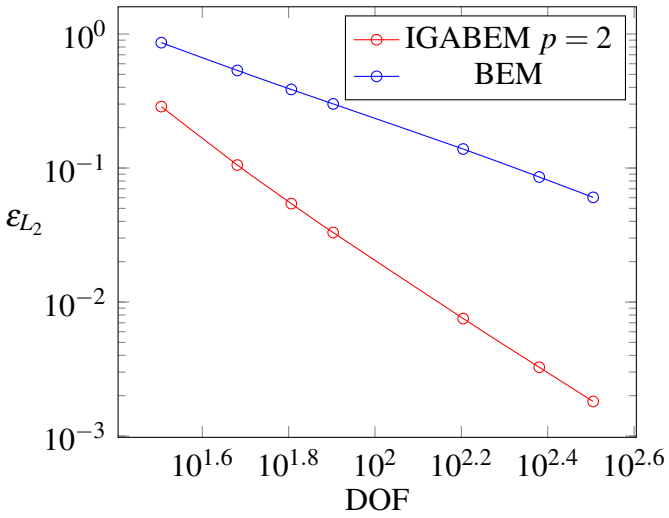

Figure 9.8 σ_R relative errors vs degrees of freedom for tube.

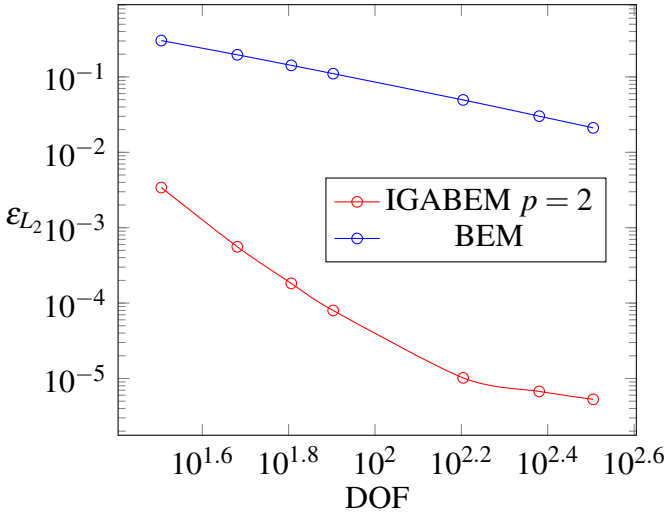

Figure 9.9 σ_θ relative errors vs degrees of freedom for tube.

9.2.2 Infinite plate with a hole

The second example of this part is an infinite plate with a circular hole, with a distributed tension P along x direction, as shown in Figure 9.10. Geometric and material properties are in Table 9.6. It is under plane-strain and 32 Gauss points are used for integration.

Table 9.6 Geometric and material properties - plate.

Property	Symbol	Value
Radius	R	50 mm
Young's Modulus	E	10^5 Pa
Poisson's ratio	ν	0.25
Distributed load	P	1 N/mm

One important difference between the tube in Example 1 and the plate in Example 2 is related to the stress state. While the former is considered under plane strain state, the latter is simulated as under plane stress state. Boundary elements for these cases are based on the plane strain approach but can be extended to plane stress if the elastic coefficients are replaced by the corresponding equivalent values. This means that, for plane stress, fundamental solutions can be obtained by substituting Poisson's ratio and Young's modulus as follows:

$$\nu^{'} = \frac{\nu}{1+\nu} \tag{9.8}$$

$$E^{'} = E\left[1 - \frac{\nu'^2}{(1+\nu')^2}\right] \tag{9.9}$$

So, after adjustment, mechanical properties of the plate become $E' = 179520$ and $\nu' = 0.2424$.

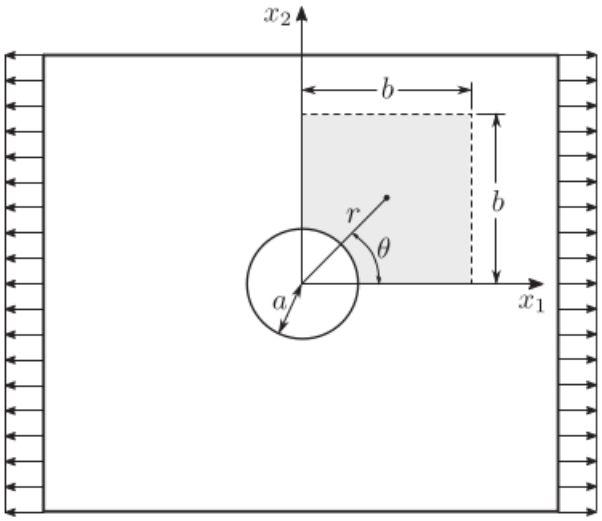

Figure 9.10 Representation of the plate.

Figure 9.11 illustrates the plate with more details and shows the boundary conditions with segment

numbers. The boundary conditions applied to segments 1 and 4 are known displacements, while segments 2 and 3 are known tractions. Lastly, segment 5 is a free surface with traction equal zero.

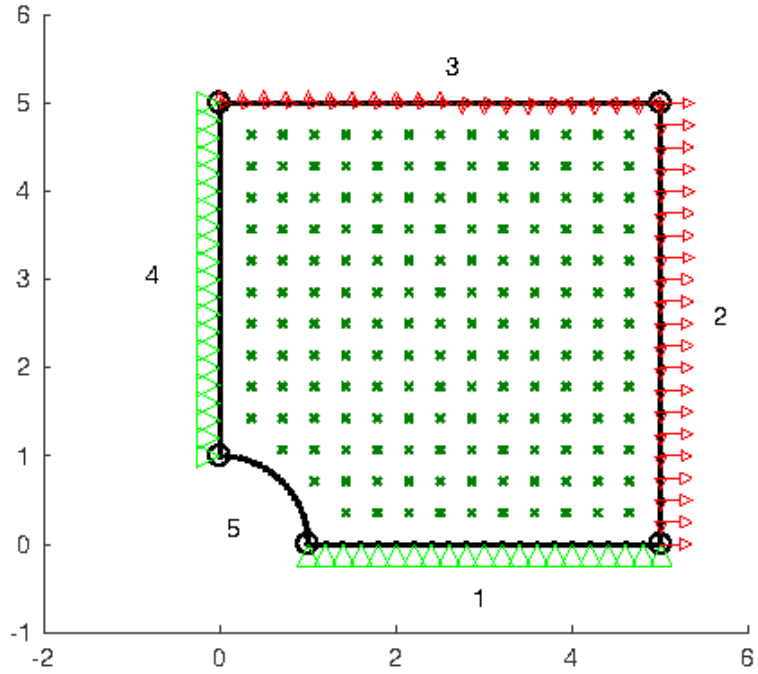

Figure 9.11 Detailed representation of plate with boundary conditions.

This problem has an analytical solution for stress field as follows:

$$\begin{bmatrix} \sigma_{11}(r,\theta) \\ \sigma_{22}(r,\theta) \\ \sigma_{12}(r,\theta) \end{bmatrix} = \begin{bmatrix} 1-\frac{a^2}{r^2}\left(\frac{3}{2}\cos(2\theta)+\cos(4\theta)+\frac{3a^4}{2r^4}\cos(4\theta)\right) \\ -\frac{a^2}{r^2}\left(\frac{1}{2}\cos(2\theta)-\cos(4\theta)-\frac{3a^4}{2r^4}\cos(4\theta)\right) \\ -\frac{a^2}{r^2}\left(\frac{1}{2}\sin(2\theta)+\sin(4\theta)+\frac{3a^4}{2r^4}\sin(4\theta)\right) \end{bmatrix}. \tag{9.10}$$

where r and θ are the usual polar coordinates, centered at the center of the hole. Exact solutions for displacement are given by:

$$\begin{bmatrix} u_1(r,\theta) \\ u_2(r,\theta) \end{bmatrix} = \begin{bmatrix} \frac{10a}{8G}\left\{\frac{r}{a}(\kappa+1)\cos(\theta)+\frac{2a}{r}\left[(1+\kappa)\cos(\theta)+\cos(3\theta)\right]-\frac{2a^3}{r^3}\cos(3\theta)\right\} \\ \frac{10a}{8G}\left\{\frac{r}{a}(\kappa-3)\sin(\theta)+\frac{2a}{r}\left[(1-\kappa)\sin(\theta)+\sin(3\theta)\right]-\frac{2a^3}{r^3}\sin(3\theta)\right\} \end{bmatrix}. \tag{9.11}$$

Lagrangian

Simulations for the infinite plate have results in good agreement with the exact solution. It is possible to see in Figure 9.12 that numerical and analytical results are close.

Table 9.7 Number of elements per segment for the 5 meshes - plate.

	Elem. per segment						
Mesh	1	2	3	4	5	**Total nodes**	**DOF**
SP-1	1	1	1	1	1	10	20
SP-2	2	2	2	2	2	20	40
SP-3	5	5	5	5	5	50	100
SP-4	10	10	10	10	10	100	200
SP-5	25	25	25	25	25	250	500

Isogeometric

As in the cylinder problem, 5 different meshes were also used for this problem (Table 9.8), with degree $p = 2$.

Table 9.8 Number of elements per segment for the 5 meshes.

Mesh	**Bézier elem. per seg.**	**DOF**
IP-1	1	28
IP-2	2	58
IP-3	3	78
IP-4	4	118
IP-5	5	138

Displacements and Stresses

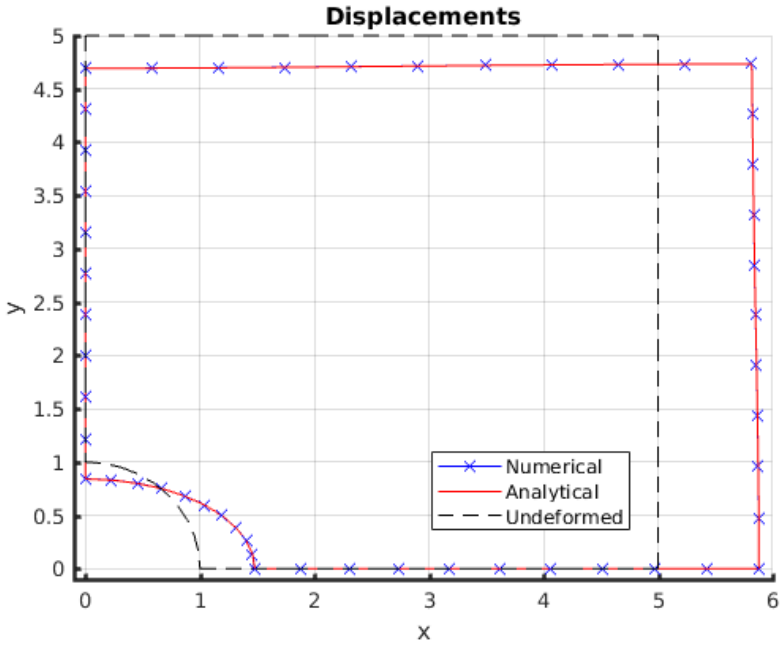

Figure 9.12 Displacements for the plate - Standard BEM.

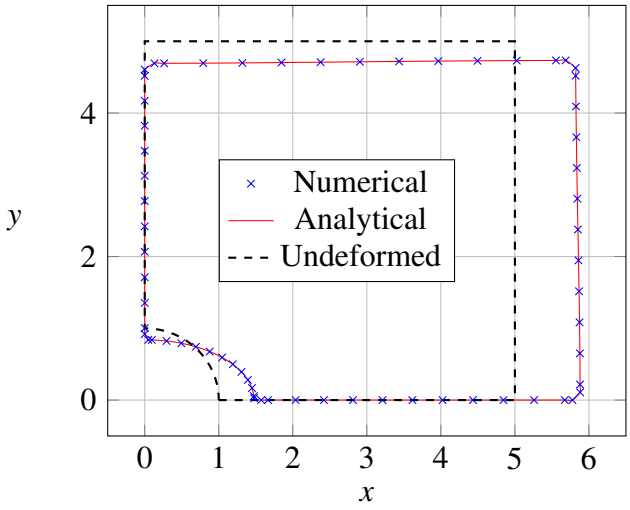

Figure 9.13 Displacements for the plate - IGABEM.

Displacements For this problem, tractions along segments 2 and 3 were calculated. The recovered tractions from IGABEM match very well the exact solutions, as can be seen in Figs. 9.14a, 9.14b, 9.15a and 9.15b.

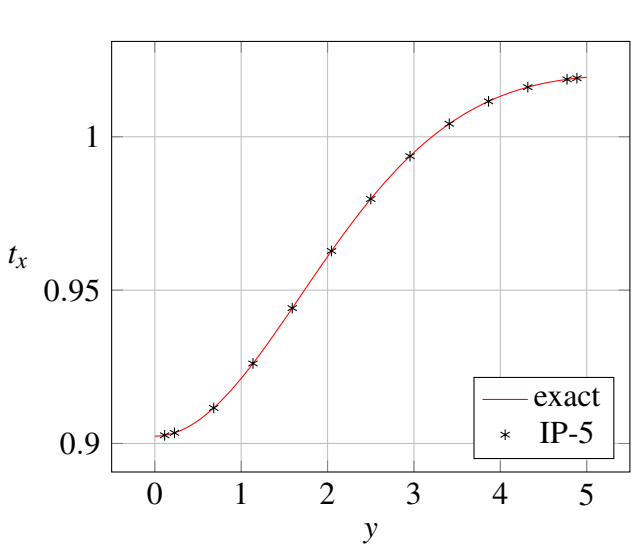

a) Tractions t_x.

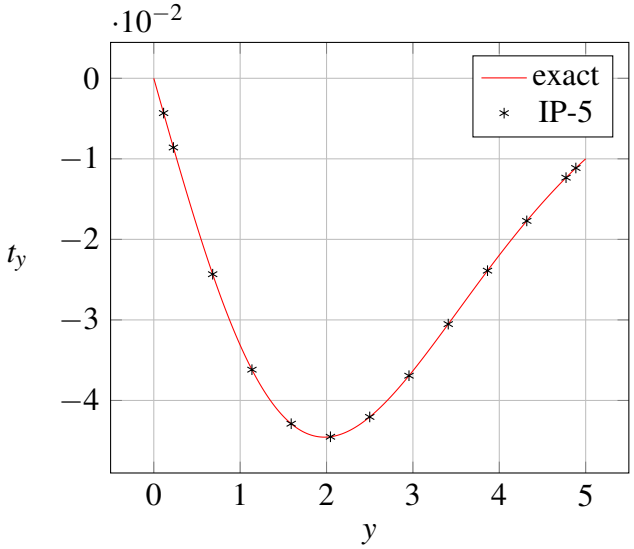

b) Tractions t_y.

Figure 9.14 Tractions along segment 2 for IGABEM

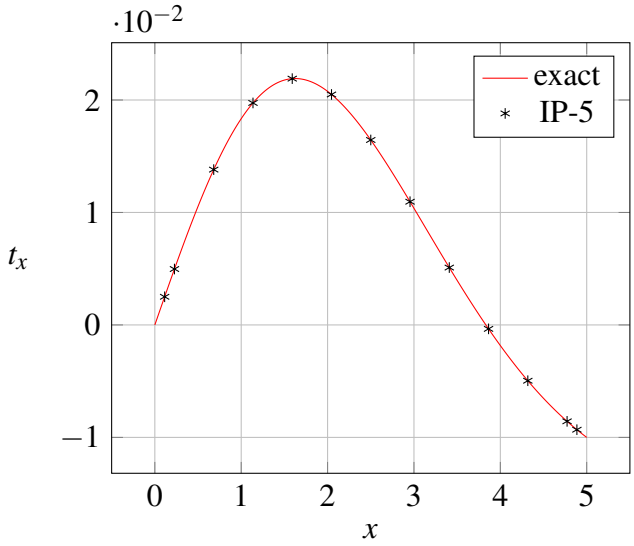

a) Tractions t_x.

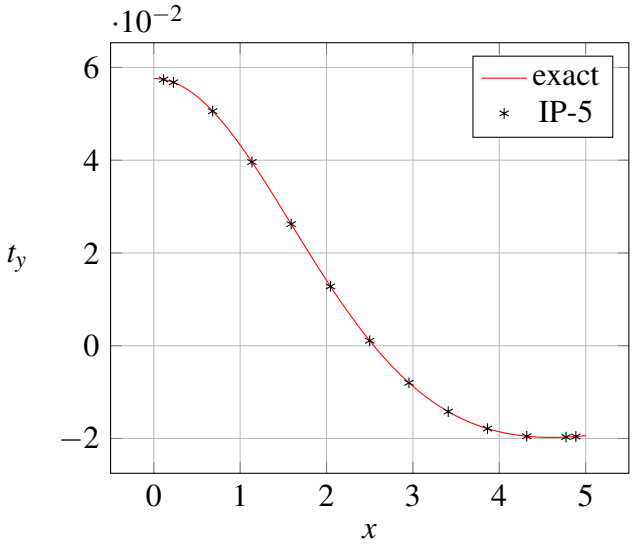

b) Tractions t_y.

Figure 9.15 Tractions along segment 3 for IGABEM

Stresses at internal points Stresses at internal points were also calculated for both Standard BEM and IGABEM. For comparing their results, three internal points were used (see Tab. 9.9) and the results for stresses σ_{11}, σ_{22} and σ_{12} are in Tab. 9.10.

Table 9.9 Coordinates of internal points - plate.

Internal Point	x	y
1	1.6667	1.6667
2	3.3333	1.6667
3	1.6667	3.3333
4	3.3333	3.3333

Table 9.10 Stresses at internal points - plate.

	Standard			**IGABEM**		
Internal Point	σ_{11}	σ_{22}	σ_{12}	σ_{11}	σ_{22}	σ_{12}
1	1.1314	-0.1314	-0.0900	1.1314	-0.1314	-0.0900
2	0.9532	-0.0396	-0.0905	0.9531	-0.0396	-0.0905
3	1.0828	0.0036	0.0329	1.0828	0.0036	0.0329
4	1.0420	-0.0420	-0.0225	1.0420	-0.0419	-0.0225

A colour map with 163 internal points for the standard simulation is shown in Figure 9.16. Deformed configuration was also plotted as the black line.

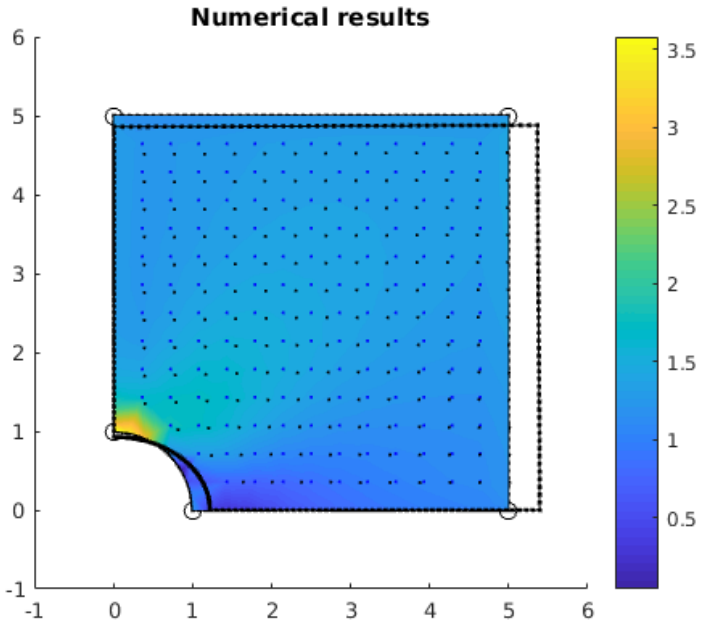

Figure 9.16 Stresses in plate - numerical results (standard).

9.2.3 Beam

In this example, consider a beam of dimensions $L \times D$ and unit depth, assumed to be in a plane stress state. As in the previous examples, 32 Gauss points are used for integration. Figure 9.17 shows the boundary condition for the cantilever beam. The parabolic traction, applied in the end of the beam is described by

$$t_2(y) = -\frac{P}{2I}\left(\frac{D^2}{4} - y^2\right), \tag{9.12}$$

where $I = D^3/12$ is the moment of inertia.

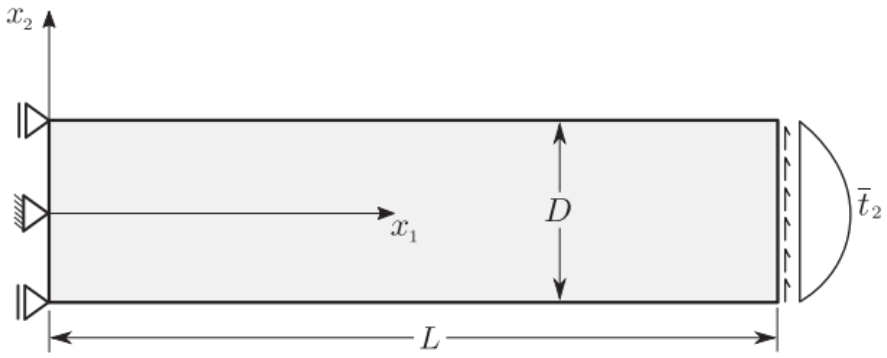

Figure 9.17 Cantilever beam [143].

Analytical solutions for displacements are:

$$u_1(x,y) = -\frac{Py}{6EI}\left[(6L-3x)x + (2+\nu)\left(y^2 - \frac{D^2}{4}\right)\right] \tag{9.13}$$

and

$$u_2(x,y) = \frac{P}{6EI}\left[(3\nu)y^2(L-x) + (4+5\nu)\frac{D^2x}{4} + (3L-x)x^2\right]. \tag{9.14}$$

For stresses, the solutions are given by:

$$\sigma_{xx}(x,y) = -\frac{P(L-x)y}{I}, \tag{9.15}$$

$$\tau_{xy}(x,y) = -\frac{P}{2I}\left(\frac{D^2}{4} - y^2\right), \tag{9.16}$$

and

$$\sigma_{yy} = 0. \tag{9.17}$$

Geometric and material properties are shown in Tab. 9.11, whilst the five meshes are defined in Tab. 9.12.

Lagrangian

Table 9.11 Geometric and material properties - beam.

Property	**Symbol**	**Value**
Length	L	48
Radius	D	12
Young's Modulus	E	3×10^7
Poisson's ratio	ν	0.3
Distributed load	P	1000

Table 9.12 Number of elements per segment for the 5 meshes - beam.

	Elem. per segment					
Mesh	1	2	3	4	**Total nodes**	**DOF**
SB-1	12	3	12	3	60	120
SB-2	16	4	16	4	80	160
SB-3	20	5	20	5	100	200
SB-4	40	10	40	10	200	400
SB-5	80	20	80	20	400	800

Isogeometric

Table 9.13 Number of elements per segment for the 5 meshes - beam.

Mesh	Bézier elem. per seg.	Collocation points	DOF
IB-1	1	12	24
IB-2	2	16	32
IB-3	3	20	40
IB-4	5	28	56
IB-5	10	48	96

Displacements Two sets of internal points were used for measuring the u_1 and u_2 displacements. The first set of points, illustrated in 9.18a, consists of 14 points distributed along the y-direction, with $x = L/2$ and $y \in [-D/2, D/2]$. The other set, 9.18b, consists of 16 evenly distributed points along the length of the beam, i.e. $x \in [0, L]$ and $y = 0$.

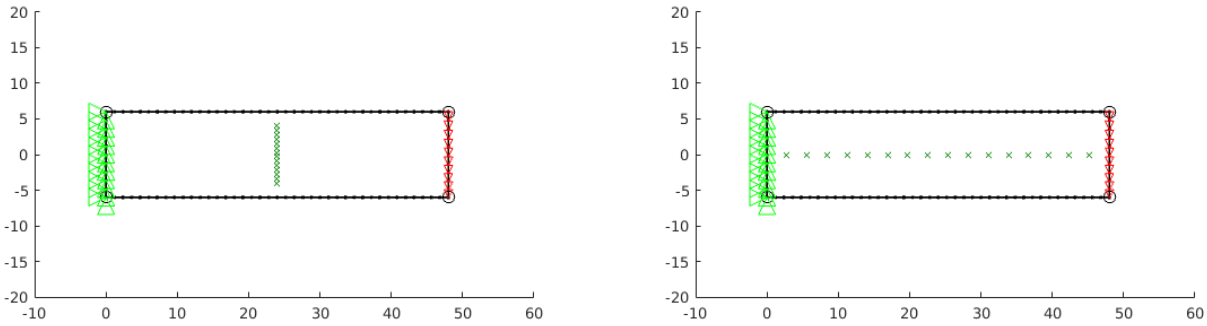

a) First set of internal points for the cantilever beam. **b)** Second set of internal points for the cantilever beam.

Figure 9.18 Two different sets of internal points.

For the lagrangian analysis, a mesh with 50 elements and 200 DOFs was used. Displacements were measured and showed good agreement with the exact solutions from Eqs. (9.13) and (9.14). Firstly, displacement in the x direction was measured and compared at the centre of the beam, i.e., for $x = L/2$. Then, the normalized result was plotted as seen in Fig. 9.19a. Those displacements were obtained from the first set of internal points, as in Fig. 9.18a. Secondly, displacements in the y direction were computed at $y = 0$ along the whole length ($x \in [0, L]$), using the second set of internal points (Fig.

9.18b). These displacements are depicted in Fig. 9.19b.

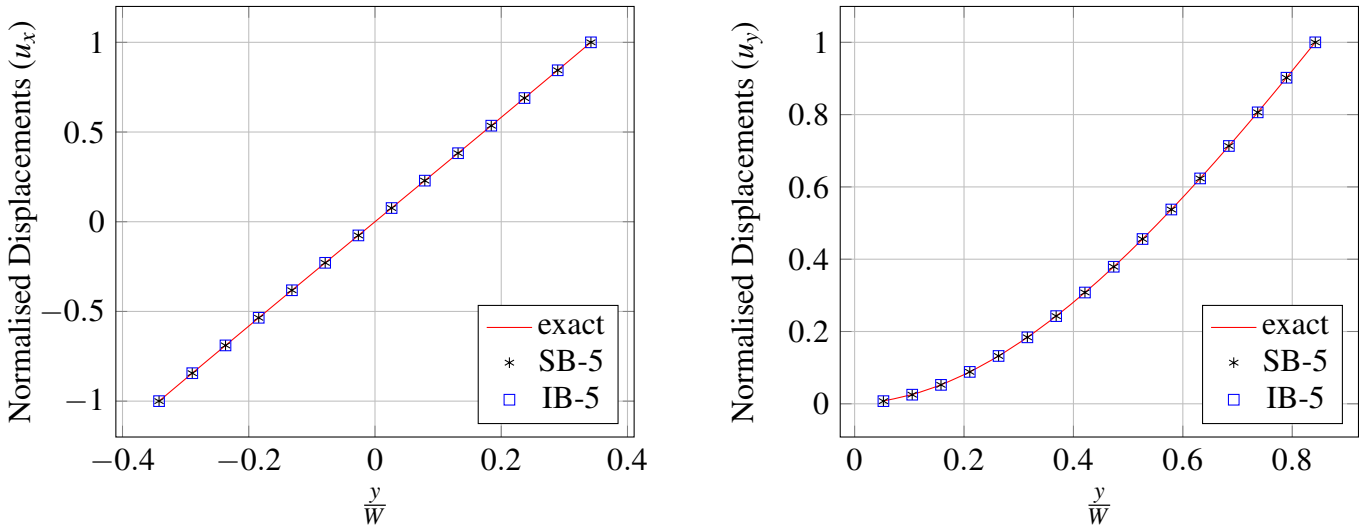

a) u_1 beam. **b)** u_2 beam.

Figure 9.19 Normalised displacements of the cantilever-beam for $x = \frac{L}{2}$

Stresses Afterwards, the stresses were numerically determined and then compared to analytical solutions in Eqs. (9.15), (9.16) and (9.17). Both stresses used the first set of internal points in Fig. 9.18a, meaning that they were determined for $x = L/2$ along the entire height of the beam.

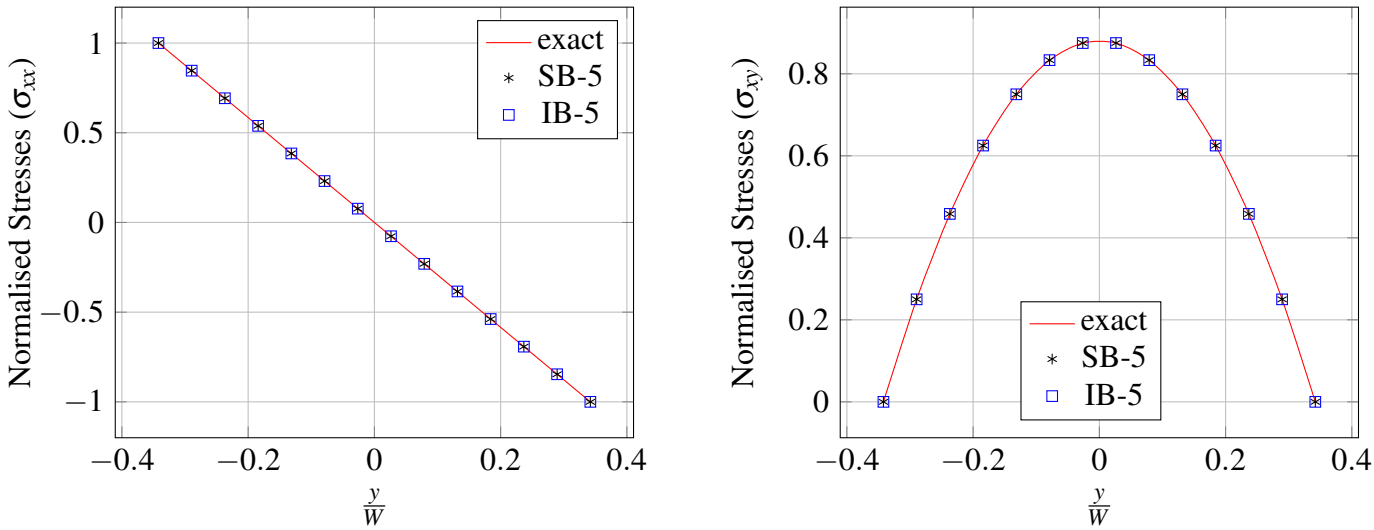

a) σ_{xx} **b)** σ_{xy}

Figure 9.20 Stress distribution for $x = L/2$ and $y \in [-D/2, D/2]$

9.2.4 Cavity

The last example for validating the IGABEM code in elasticity is a circular cavity under internal pressure in an infinite medium (Fig. 9.21). Once more, we compare the results from analytical solutions, Standard BEM and IGABEM. It is a plane strain problem and integration is performed with 32 Gauss points. Table 9.14 describes its geometry, internal points, material properties and load.

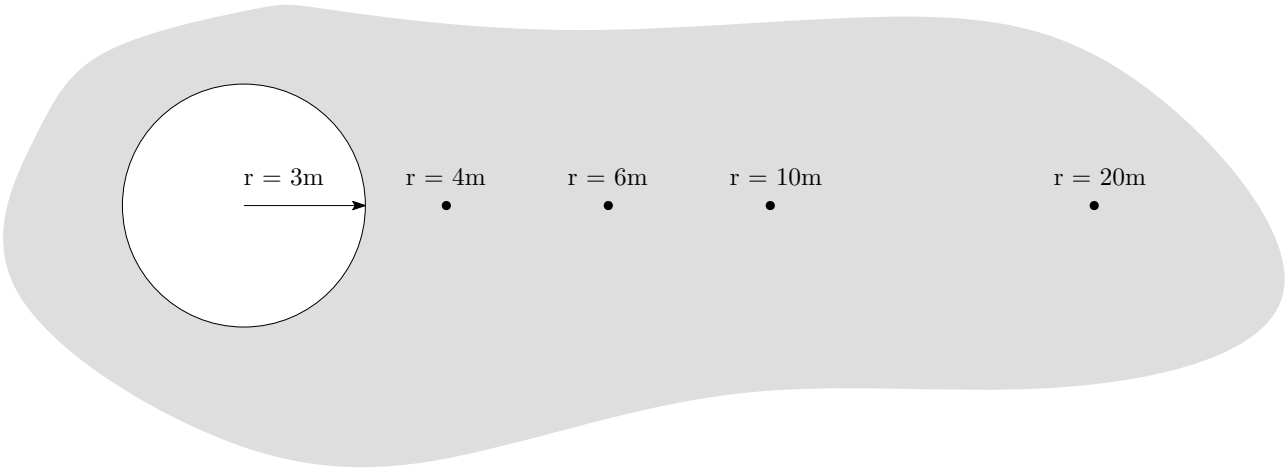

Figure 9.21 Circular cavity under internal pressure - internal points.

Exact solutions are known for this problem - radial stresses σ_r and radial displacements u_r are described in Eqs. (9.18) and 9.19, respectively.

$$\sigma_R = -\frac{pa^2}{r^2} \tag{9.18}$$

$$u_R = \frac{pa^2(1+\nu)}{Er} \tag{9.19}$$

Table 9.14 Geometric and material properties - cavity.

Property	Symbol	Value
Radius	R_a	3 m
Young's Modulus	E	207900 Pa
Poisson's ratio	ν	0.1
Pressure	P	100 Pa

Lagrangian

Table 9.15 Number of elements per segment - cavity.

	Elem. per segment					
Mesh	1	2	3	4	**Total nodes**	**DOF**
SC-1	1	1	1	1	8	16

Isogeometric

Table 9.16 Number of Bézier curves per segment - cavity.

Mesh	**Bézier curves per seg.**	**Collocation points**	**DOF**
IC-1	1	12	24

Displacements and Stresses at internal points

For this example, coarse meshes are used for both Standard BEM and IGABEM, because even with one element for each quarter of the circle, results are in good agreement with the analytical solutions. Numerical values from Standard BEM and IGABEM can be seen in Tabs. 9.17 and 9.18, respectively.

It is seen that even with a low number of DOFs (16 for standard BEM and 24 for IGABEM), errors are as low as 0.00099% for displacements and 0.00125% for stresses.

Table 9.17 Radial displacements on internal points - cavity.

R	**Analytical solution**	**Standard BEM**	**IGABEM**
4	1.1904761905e-03	1.1904761904e-03	1.1904879886e-03
6	7.9365079365e-04	7.9365079365e-04	7.9367493192e-04
10	4.7619047619e-04	4.7619047619e-04	4.7621101083e-04
20	2.3809523810e-04	2.3809523810e-04	2.3810692715e-04

Table 9.18 Radial stresses on internal points - cavity.

R	Analytical solution	Standard BEM	IGABEM
4	-56.25	-56.8674679629	-56.2492985883
6	-25.00	-24.9144213220	-25.0009752794
10	-9.00	-8.9298621781	-9.0003949020
20	-2.25	-2.2284373006	-2.2501103171

Our conclusion is that, as expected for infinite domains, both Standard BEM and IGABEM are accurate when comparing to the exact solutions. Some comparison with FEM, for instance, would be interesting in this case.

9.3 Contact problems

9.3.1 Cattaneo-Mindlin problem

The chosen configuration for the Cattaneo-Mindlin problem is depicted in Fig. 9.22. It consists of two elastically-similar bodies in frictional contact. The body is loaded with a normal force and a tangential force while restricted at its central node in the $x-$ direction in order to avoid gross slip and the system turning into a mechanism. The body 2 is fully restrained on its bottom. For this model, plane strain is assumed and integration is performed with 20 points. Parts of this section are reproductions of the research paper ***Analysis of 2D contact problems under cyclic loads using IGABEM with Bézier decomposition*** [144]. [1]

Firstly, a normal load is applied. Then, this load is maintained constant while a tangential load is cyclically applied. A depiction of the loading scheme is shown in Fig. 9.23.

[1] **© 2022 Elsevier Ltd. Reproduced with non-commercial purposes.**

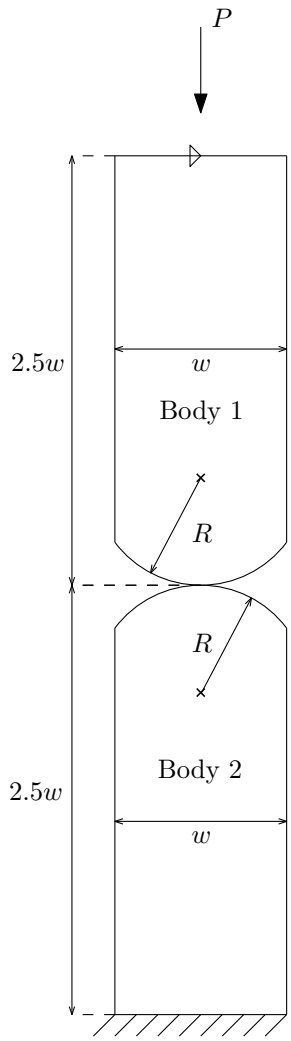

Figure 9.22 Cattaneo-Mindlin - problem configuration.

As the two bodies have similar geometries, they are discretised in the same fashion and can be thought as mirrored along the $x-$axis. Equivalent segments have the same number of elements, for example, the segments in contact are discretised in the same way.

To easily compare results from conventional BEM and IGABEM, the mesh is discretised in a way that both have the same number of node-pairs in the contact zone, i.e., $NP_c = 61$.

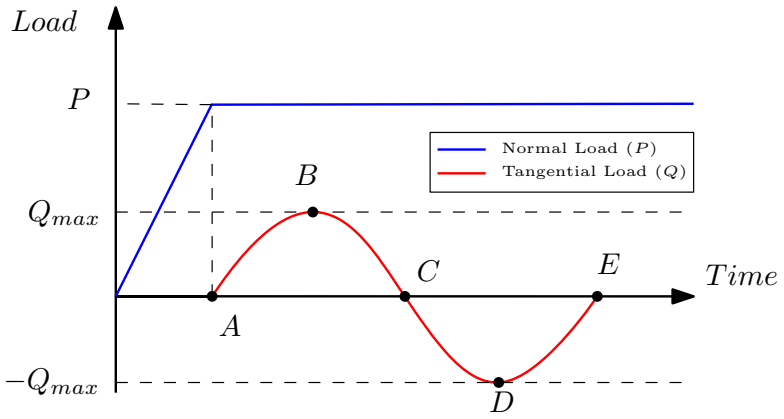

Figure 9.23 Cattaneo-Mindlin - loading scheme containing five steps (A-E).

In Figure 9.23, point *A* is when the normal load *P* reaches its final value, whereas point *B* is the moment when the maximum tangential load is applied. Afterwards, tangential load starts to decrease, passing through zero at point *C* and decreasing further. Point *D* is when the tangential load is in its minimum value and, finally, point *E* is when the tangential load reaches zero again. Geometric and material properties can be seen in Table 9.19.

Table 9.19 Cattaneo-Mindlin - Dimensions and material properties.

Property	**Symbol**	**Value**
Radius	R	70 mm
Length	w	6.5 mm
Young's Modulus	E	73.4 GPa
Poisson's ratio	ν	0.33
Pressure	P	100 N/mm
Friction coefficient	f	0.3

In this problem, both BEM and IGABEM have a finer mesh in segments that may be in contact. Figures 9.24a and 9.24b show the meshes for BEM and IGABEM.

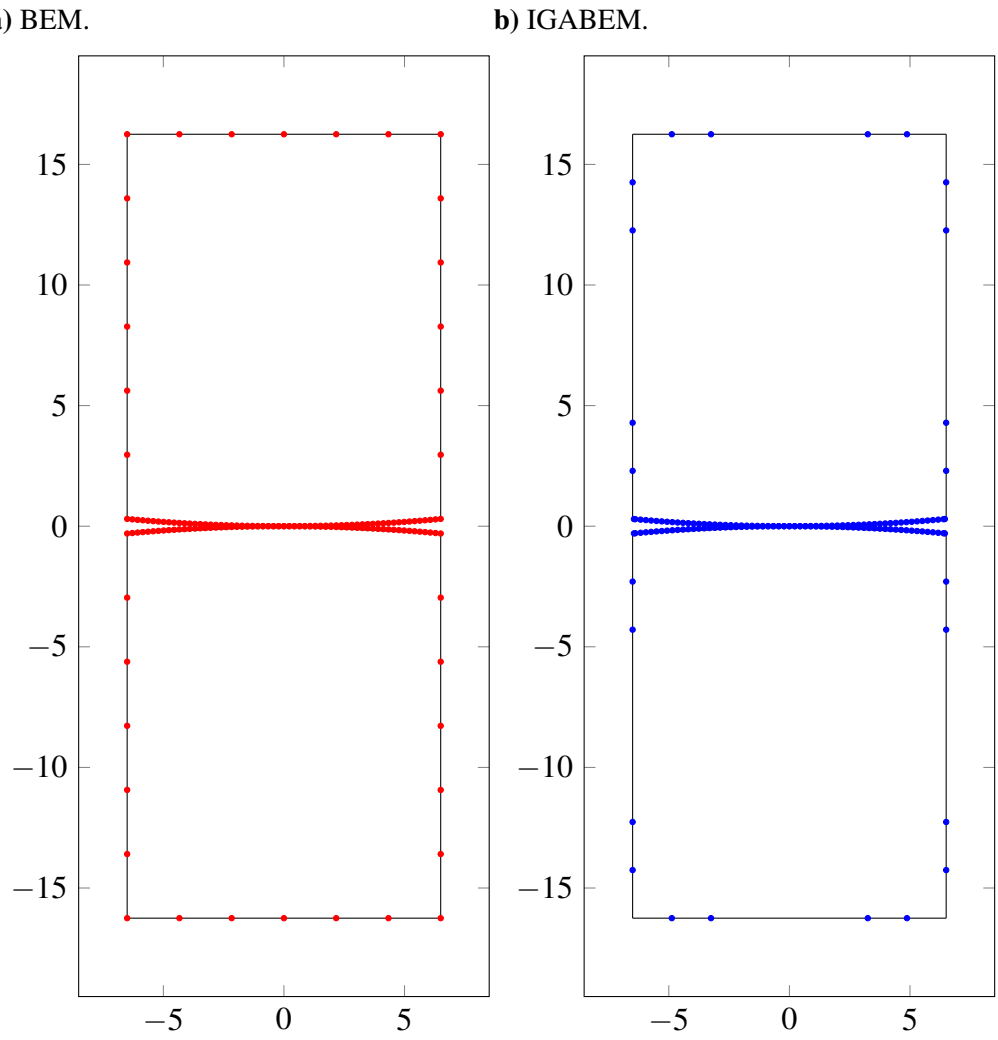

Figure 9.24 Cattaneo-Mindlin - meshes for 61 node-pairs.

Tractions

Figures. 9.25a- 9.25d compare the tractions of conventional BEM and IGABEM with the analytical solution for four out of five loading steps, B to E. Both normal and tangential tractions for BEM (t_n^{BEM} and t_t^{BEM}), IGABEM (t_n^{IGA} and t_t^{IGA}) and analytical solutions (t_n^A and t_t^A) are shown.

The vertical dimension of the two bodies is large enough ($2.5w$) to provide no tangential load in the first step as demanded by the analytical solution. So $\mathbf{t}_t \approx \mathbf{0}$ in the first step.

Displacements

Displacements fields in normal and tangential directions were measured and their results are presented in this section. Figures (9.26a-9.26d) compare the displacements for BEM and IGABEM for load steps 2 to 5.

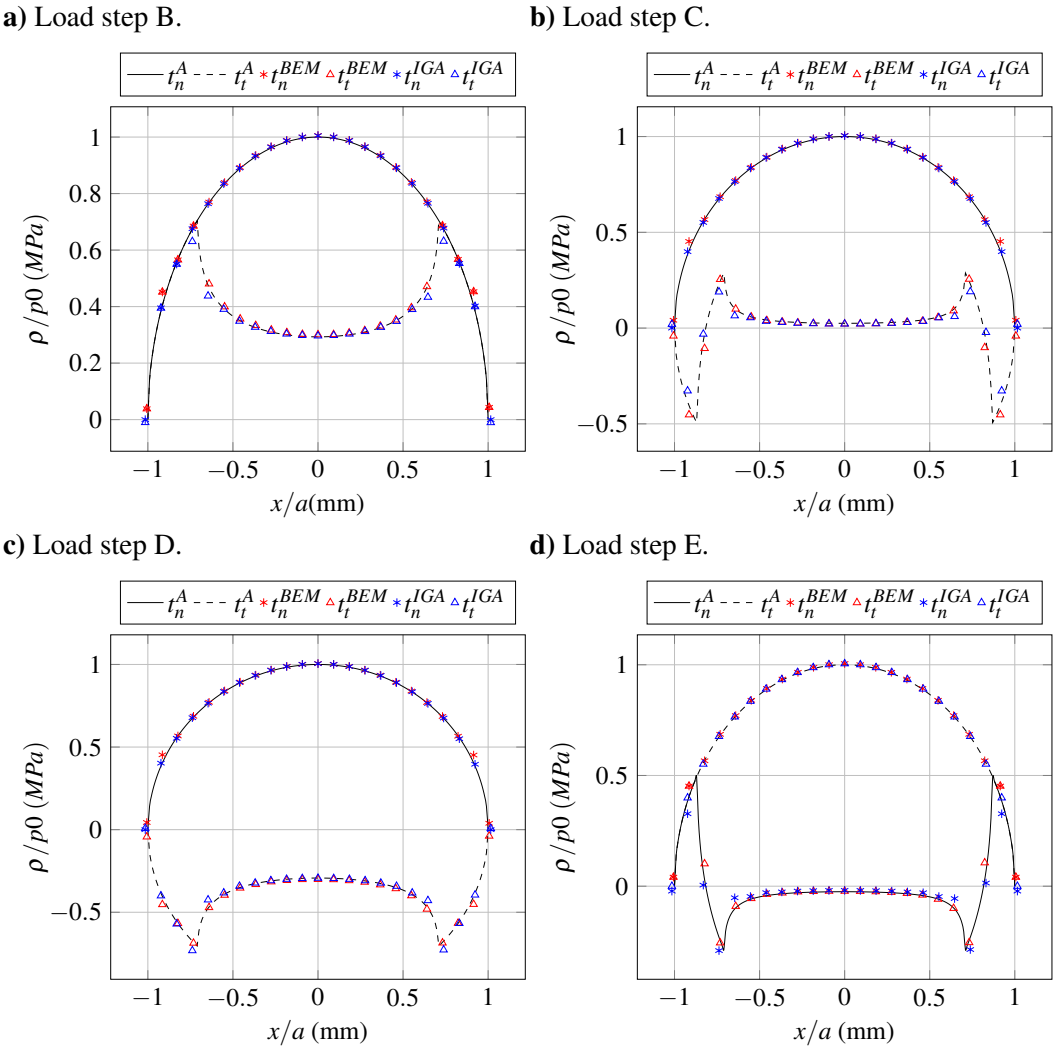

Figure 9.25 Cattaneo-Mindlin - normal (t_n) and tangential (t_t) tractions comparison of IGABEM, BEM and analytical results at four load steps (B-E).

Only the displacements of node-pairs within the contact zone are shown. A good agreement between the two methods is evident.

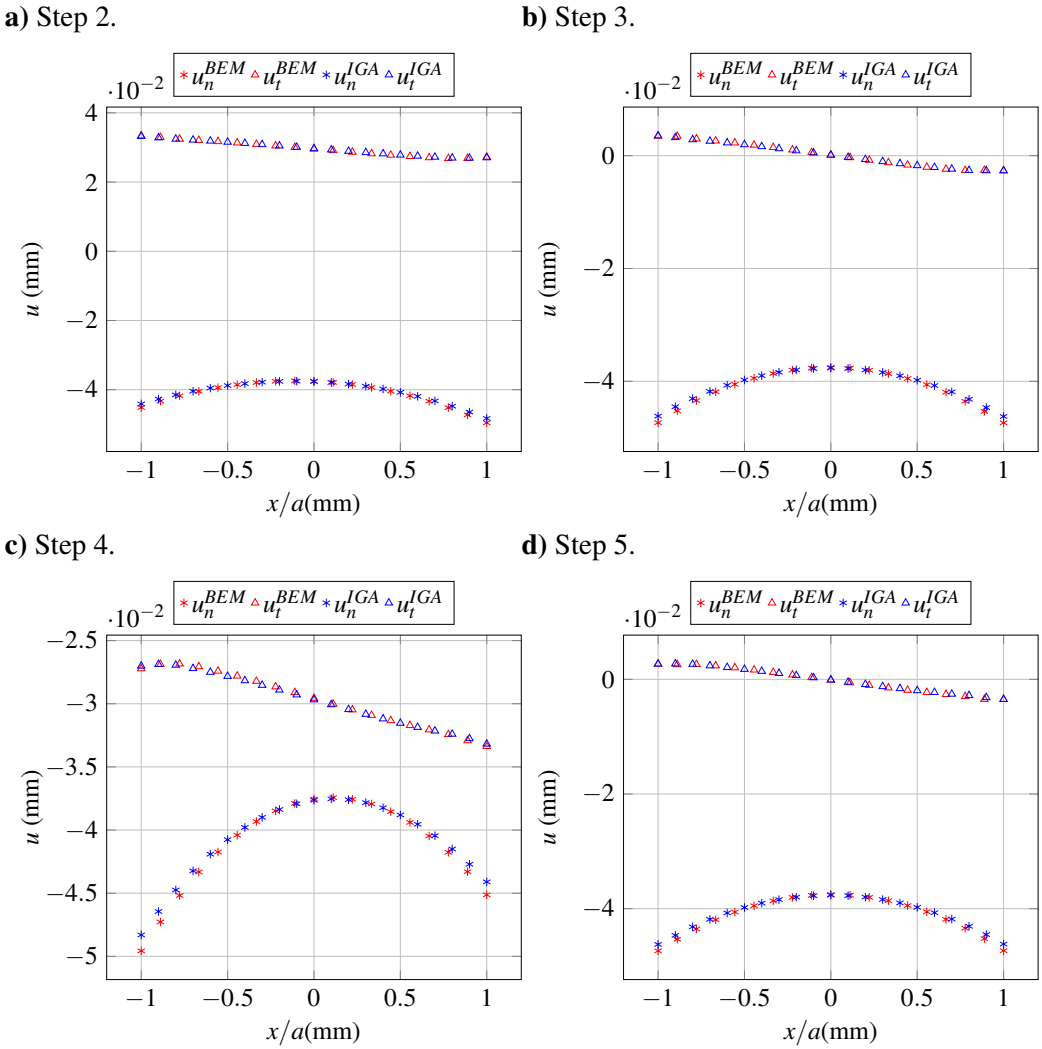

Figure 9.26 Cattaneo-Mindlin - IGABEM and BEM normal (u_n) and tangential (u_t) displacements fields over contact surface for load steps (B-E).

The results are in good agreement. The maximum error is 4.104 % for shear tractions localised in the frontier of the slip-stick region. In all other points, all curves are very close. Normal tractions remain the same during the load steps while tangential tractions change.

Peak pressure p_0 and contact half-width a comparison for different meshes

In this part, contact half-width (a) and peak pressure (p_0) are compared for five different meshes. For both BEM and IGABEM, the mesh remains the same in all but the contact surfaces. The first mesh has 21 node-pairs, the second has 41 and they get more refined up to 101 node-pairs.

Starting with the peak pressure comparison, Table 9.20 shows data for the first time step, for

each mesh. Analytical value for peak pressure is $p_0 = 698\ MPa$. Using the coarsest mesh, IGABEM outperforms BEM when describing the maximum normal pressure. For other meshes, BEM and IGABEM have almost similar errors and can be considered as equivalent. Also, the error does not seem to decrease with mesh refinement over the contact area, fluctuating around 0.2%.

As observed in Table 9.21 and Figure 9.28, the half-width (a) error is more affected by mesh refinement, as it starts around 45% and 42% with the coarse mesh and decreases to 1.21% and 0.14% for BEM and IGABEM, respectively.

This behaviour reveals an advantage of IGABEM over BEM for the contact half-width even with fewer degrees of freedom. Both are equivalent for modelling the maximum normal pressure.

Since Lagrange functions form polynomial shape functions, they cannot represent conic sections such as circular arcs, for example. NURBS, on the other hand, can exactly represent circular arcs. In the two examples, circular arcs are used for modelling the geometry. This fact makes IGABEM more accurate when describing the geometry.

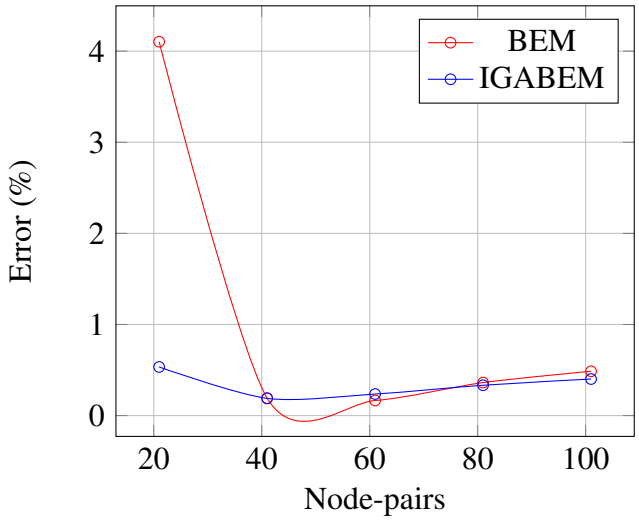

Figure 9.27 Cattaneo-Mindlin - load step (A) normal pressure error comparison for different meshes.

Table 9.20 Cattaneo-Mindlin - peak pressure (p_0) comparison of IGABEM, BEM and analytical results for different number of node-pairs.

Node-pairs	BEM	$\lvert\varepsilon_{BEM}(\%)\rvert$	DOFs BEM	IGA	$\lvert\varepsilon_{IGA}(\%)\rvert$	DOFs IGA
21	669.167	4.104	152	694.078	0.534	132
41	696.462	0.192	232	699.121	0.189	212
61	698.958	0.166	312	699.453	0.237	292
81	700.332	0.363	392	700.127	0.333	372
101	701.197	0.487	472	700.603	0.401	452
Analytical $p_0 = 697.8025\ MPa$						

Table 9.21 Cattaneo-Mindlin - contact half-width (a) comparison of IGABEM, BEM and analytical results for different number of node-pairs.

Node-pairs	BEM	$\lvert\varepsilon_{BEM}(\%)\rvert$	IGABEM	$\lvert\varepsilon_{IGABEM}(\%)\rvert$
21	0.651	45.116	0.686	42.186
41	0.976	17.675	1.002	15.505
61	1.085	8.525	1.104	6.913
81	1.139	3.954	1.154	2.672
101	1.172	1.214	1.184	0.143
Analytical $a = 1.1860\ mm$				

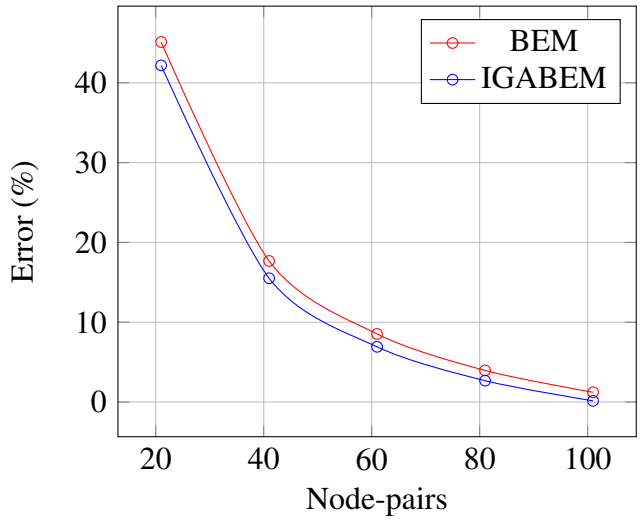

Figure 9.28 Cattaneo-Mindlin - contact half-width (a) error comparison for different meshes.

BEM reaches 4.1037% error for peak pressure even with coarsest mesh, while IGABEM reaches 0.5338% for the same number of degrees of freedom. This shows how accurate the IGABEM is for coarse mesh. The length of the contact area, on the other hand, seems to be highly affected by the number of node-pairs over the contact segments. This was expected as we are considering a node-to-node contact algorithm. With fewer node-pairs over the segment, the distance between them increases,

making it difficult to accurately determine the contact area. To improve the accuracy for the length of contact area with coarse mesh, the implementation of segment-to-segment contact algorithm is strongly recommended.

Newton-Raphson's Method error evolution

The generalised Newton method was successfully used for solving contact problems [97, 103, 140]. In this problem, it converged with less than 10 iterations for conventional and isogeometric BEM on all steps, considering $\varepsilon = 10^{-9}$.

Figures 9.30 and 9.29 present the error evolution for conventional BEM and IGABEM, respectively. As expected, the first load step demands more iterations to converge. IGABEM needed 8 iterations for convergence, while BEM needed 7.

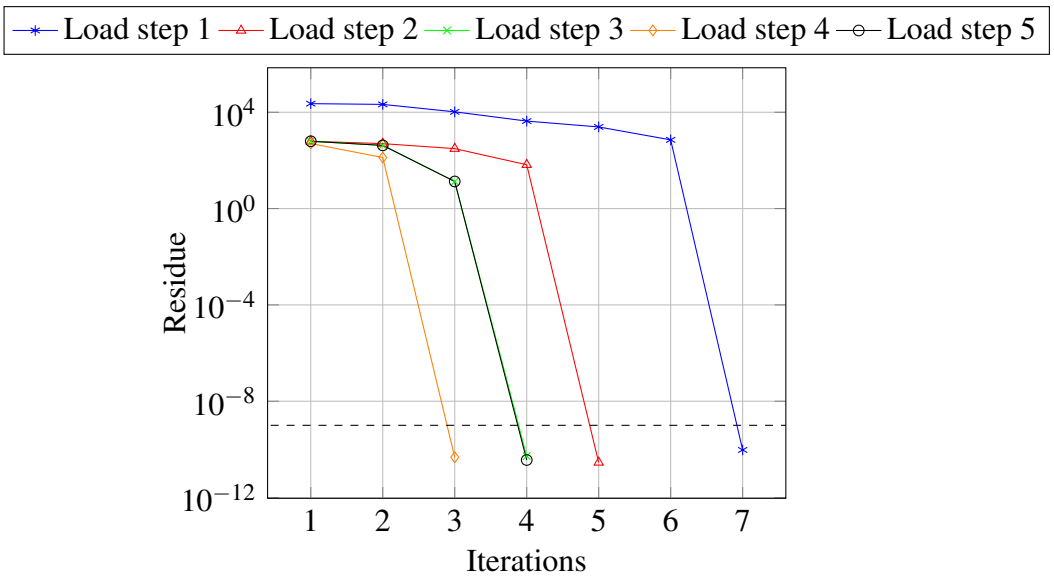

Figure 9.29 Cattaneo-Mindlin - Newton Method error evolution for conventional BEM.

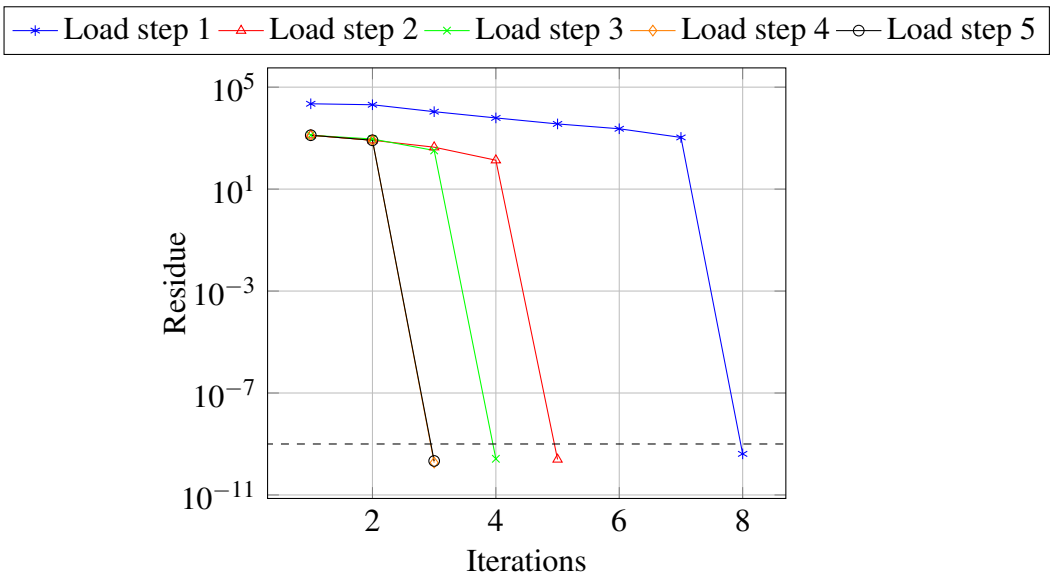

Figure 9.30 Cattaneo-Mindlin - Newton Method error evolution for IGABEM.

CPU time comparison

CPU time data presented in Table 9.22 shows that IGABEM incurs in higher computational cost, as expected. This is due to the basis functions being more complex than conventional Lagrangian polynomials. The data can be used to compare the amount of time needed for running the entire problem and for solving all Newton's method iterations as well.

BEM was faster and the ratio between BEM and IGABEM range from 41.17% for 21 node-pairs to 53.08% for 101 node-pairs. Nonetheless, the most time-consuming problem to run was solved in less than 9 seconds.

Table 9.22 Cattaneo-Mindlin - CPU time comparison.

	Newton Method		Entire problem	
Node pairs	**BEM**	**IGABEM**	**BEM**	**IGABEM**
21	0.0246	3.0479	2.1057	5.1151
41	0.0942	3.0593	2.7981	5.3816
61	0.2111	3.1950	3.2974	6.0469
81	0.2780	3.4878	3.8804	6.9831
101	0.4967	3.9759	4.4349	8.3559

9.3.2 Bulk stress problem

The bulk stress problem geometry is shown in Fig. 9.31. In this problem, tangential and bulk loads are in phase with each other. Geometry, material and load properties are in Tab. 9.23. This problem is considered under plane strain and integration is carried out with 20 Gauss points. Parts of this section are reproductions of the research paper ***Analysis of 2D contact problems under cyclic loads using IGABEM with Bézier decomposition*** [144]. [2]

Table 9.23 Bulk stress problem - geometric and material properties.

Property	**Symbol**	**Value**
Radius	R	70 mm
Width	w	6.5 mm
Young's Modulus	E	73.4 GPa
Poisson's ratio	ν	0.33
Friction coefficient	f	0.3
Pressure	P	100 N/mm
Tangential load	Q	15 N/mm
Bulk load	B	15 N/mm

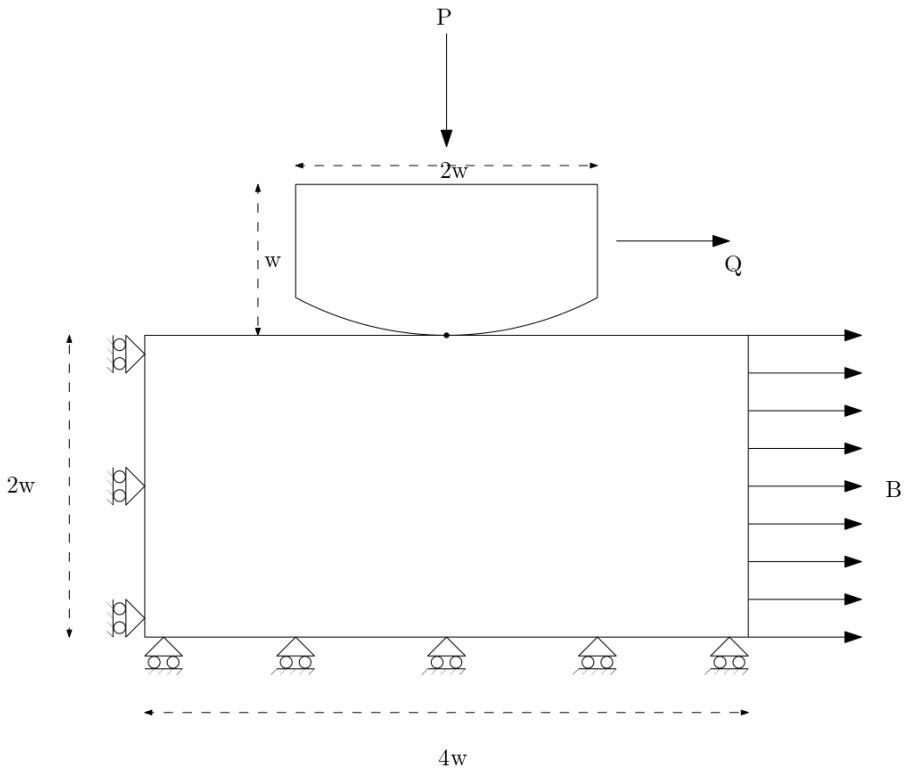

Figure 9.31 Bulk stress problem geometry.

This configuration has been chosen because it is commonly used for fretting fatigue experiments [122] , as shown in Fig. 9.32.

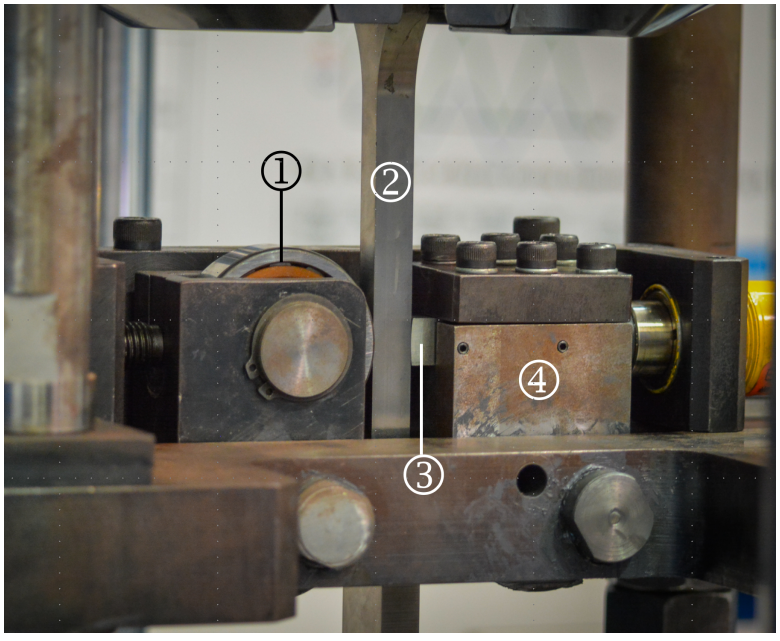

Figure 9.32 Detailed view of a fretting fatigue experimental setup. 1) roller, 2) dog-bone specimen, 3) cylindrical pad and 4) pad holder.

In this problem, both BEM and IGABEM have a finer mesh in segments that may be in contact and where the bulk load is applied. Figures (9.33a) and (9.33b) show meshes for BEM and IGABEM.

a) BEM. **b)** IGABEM.

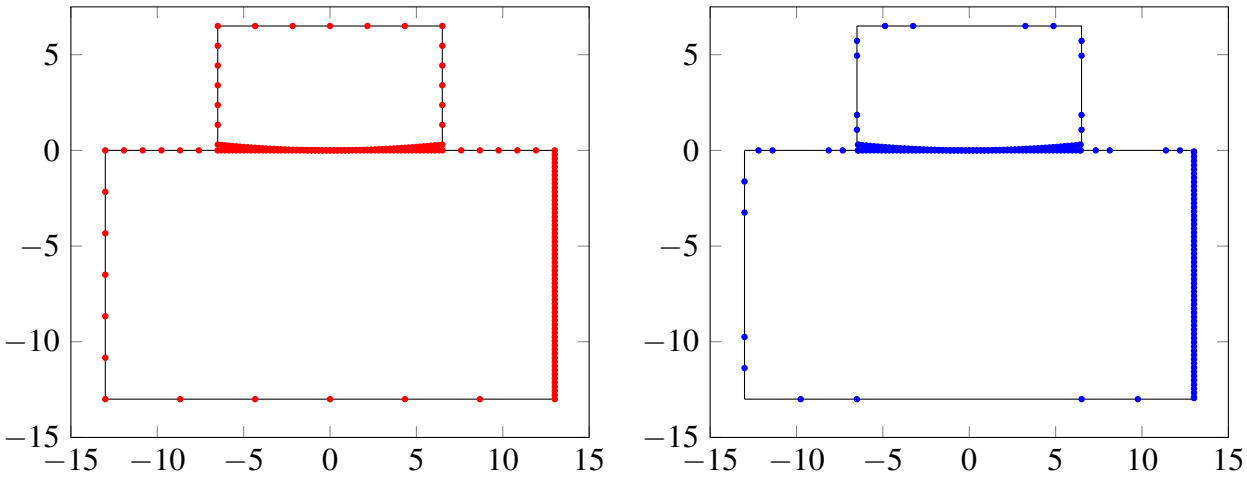

Figure 9.33 Bulk stress problem - meshes for 61 node-pairs.

Tractions

Figures (9.34a-9.34d) show the normal and tangential tractions for BEM, IGABEM and analytical results for steps B to E. There are 61 node-pairs over the contact segments but only those within the contact are shown. Both normal and tangential tractions for BEM (t_n^{BEM} and t_t^{BEM}), IGABEM (t_n^{IGA} and t_t^{IGA}) and analytical solutions (t_n^A and t_t^A) are shown.

Although BEM and IGABEM perform similarly, it is difficult for IGABEM to accurately represent the sharp edges on tangential traction t_x. This is because the NURBS used as basis functions for IGABEM are smooth as in Fig. 9.35.

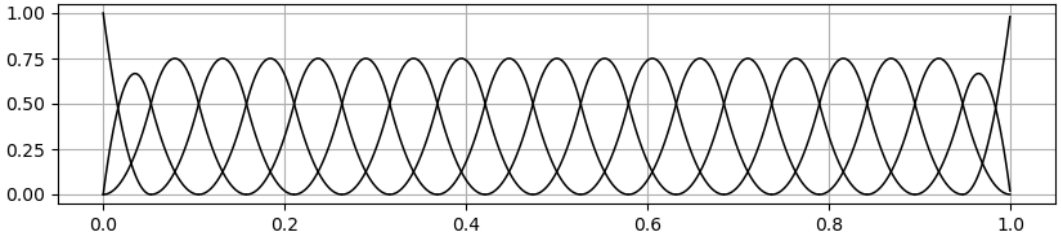

Figure 9.35 Bulk stress problem - NURBS basis functions for 21 contact node-pairs.

Displacements

Similarly to the previous example, figures (9.36a-9.36d) compare the displacements for BEM and IGABEM for load steps 2 to 5.

Only the displacements of node-pairs within the contact zone are shown. Both methods provide

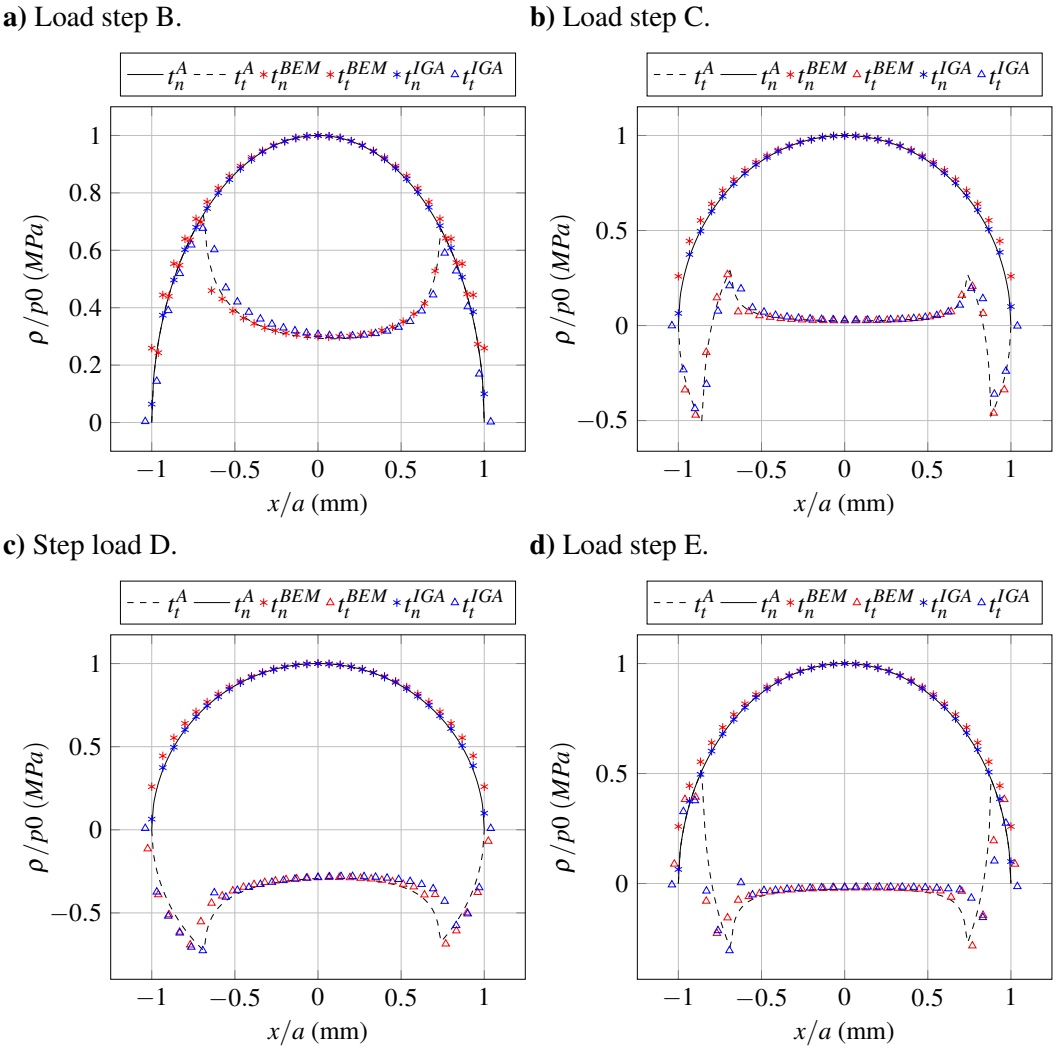

Figure 9.34 Bulk stress problem - normal (t_n) and tangential (t_t) tractions comparison of IGABEM, BEM and analytical results at four load steps (B-E).

similar results.

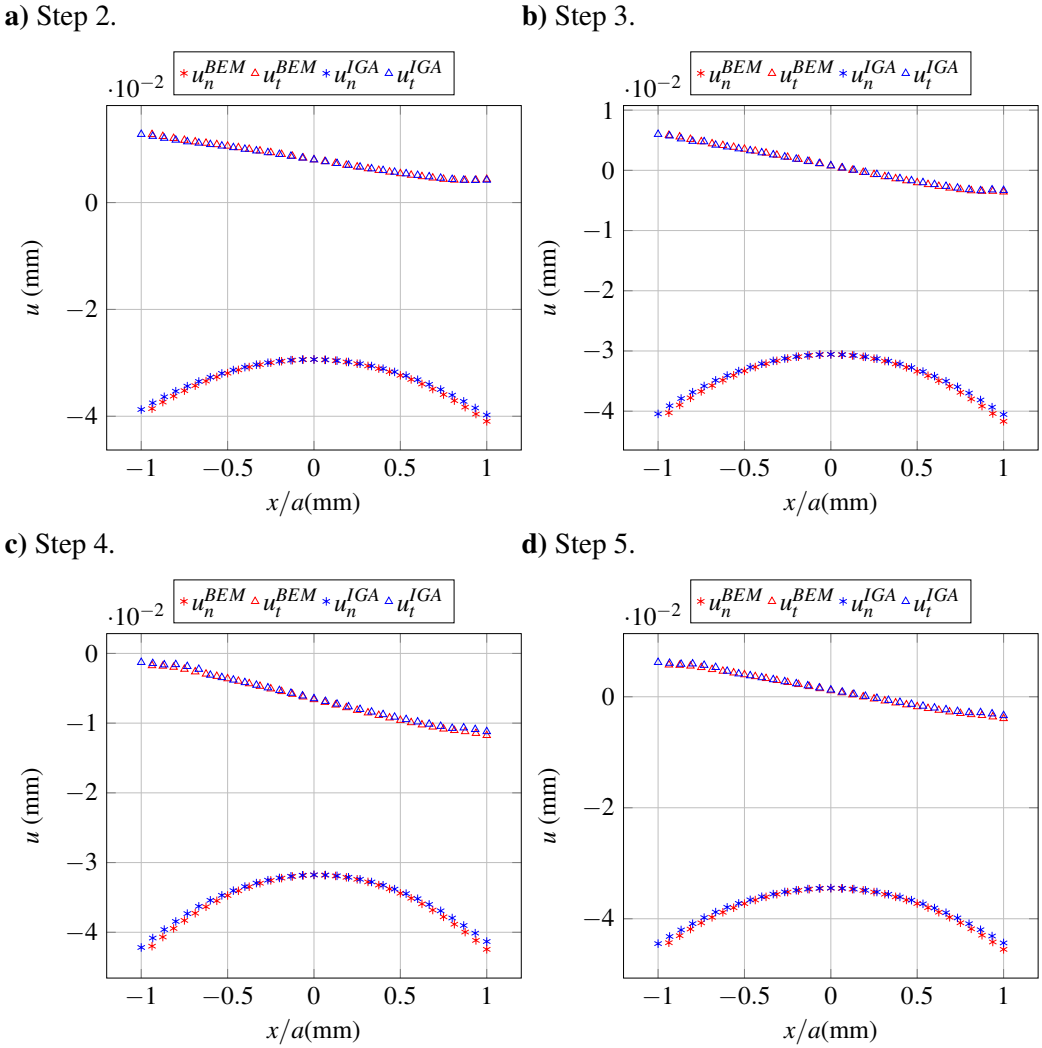

Figure 9.36 Bulk stress problem - IGABEM and BEM normal (u_n) and tangential (u_t) displacements fields over contact surface for load steps (B-E).

Peak pressure p_0 and contact half-width a comparison for different meshes.

Similarly to the previous example, peak pressure (p_0) and contact half-width (a) are compared for different meshes. Table 9.24 shows maximum normal pressure data for the first time step, for each mesh. The exact value of peak pressure is $p_0 = 486.92\ MPa$. Error *versus* DOFs are depicted in Figure 9.37. Noticeably, the errors for both methods are small (less than 1%) for all meshes. Except for the coarsest mesh, further refinement does not seem to have much influence on errors, as they start around 0.8 %, decrease and then fluctuate near 0.25 %.

The values of contact half-width, a, and the relative errors, ε, using the analytical solution as reference are listed in Tab. 9.25 and show that the relative error is quite similar for both methods.

The largest difference of 4.086% happens in the coarsest mesh, with IGABEM being more accurate. IGABEM outperforms BEM for all but the last case, when BEM is 0.201% more accurate.

Figure 9.38 presents the error for contact half-width (a) as being highest with the coarsest mesh (21 node-pairs) and then decreasing, increasing at 61 node-pairs and then decreasing even further. This behaviour, also observed by [97], is due to the node-to-node approach where the contact half-width is highly dependent on mesh refinement and on the location of the collocation points. In this study, for 41 node-pairs, a collocation point (at $x = 1.6700$ *mm*) gets closer to the exact value for the contact edge ($a = 1.6997$ *mm*) and still is inside the contact zone. When refined to 61 node-pairs, collocation points change and the closest collocation point (at 1.5455 *mm*) to the contact edge within the contact zone is not as close as with 41 node-pairs.

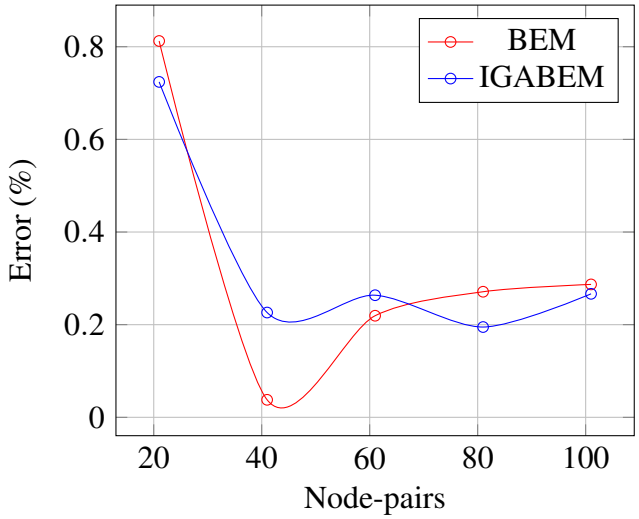

Figure 9.37 Bulk stress problem - load step 1 normal pressure error comparison for different meshes.

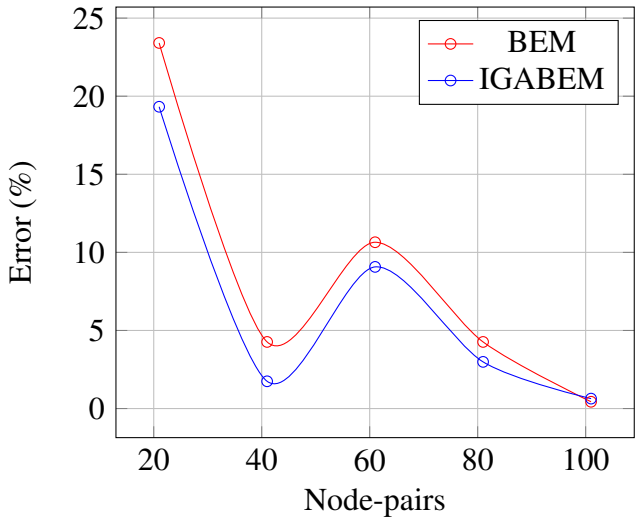

Figure 9.38 Bulk stress problem - contact half-width (a) error comparison for different meshes.

Table 9.24 Bulk stress problem - maximum normal pressure (t_Y) and peak pressure (p_0) comparison for different number of node-pairs.

Node-pairs	BEM	$\|\varepsilon_{BEM}(\%)\|$	DOFs BEM	IGA	$\|\varepsilon_{IGA}(\%)\|$	DOFs IGA
21	490.876	0.812	204	483.394	0.724	182
41	487.104	0.038	324	488.021	0.226	302
61	487.988	0.219	444	488.204	0.264	422
81	488.240	0.271	564	487.869	0.195	542
101	488.317	0.287	684	488.218	0.267	662
Analytical $p_0 = 486.9200\ MPa$						

Table 9.25 Bulk stress problem - contact half-width (a) for different number of node-pairs.

Node-pairs	BEM	$\|\varepsilon_{BEM}(\%)\|$	IGABEM	$\|\varepsilon_{IGABEM}(\%)\|$
21	1.302	23.410	1.371	19.324
41	1.627	4.266	1.670	1.745
61	1.518	10.649	1.546	9.071
81	1.627	4.266	1.649	2.989
101	1.692	0.435	1.711	0.636
Analytical $a = 1.6997\ mm$				

A similar scenario happens for this example. Both BEM and IGABEM show accurate results for peak pressure even with coarse meshes, with errors ranging from 0.812% to 0.038%.

Newton-Raphson's Method error

Figures 9.40 and 9.39 present the error evolution for conventional BEM and IGABEM, respectively. In this example, IGABEM converges in 8 iterations for the first step, while BEM converges in 11. This is not seen in example 1, where both needed the same number of iterations. After all steps, IGABEM needed 23 iterations, while BEM needed 29.

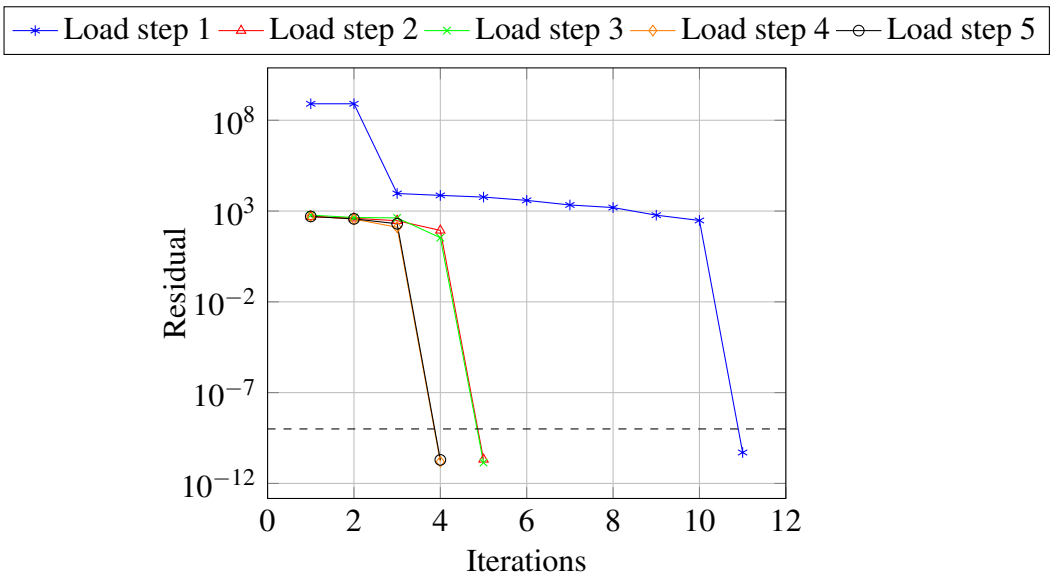

Figure 9.39 Bulk - Newton Method error evolution for conventional BEM.

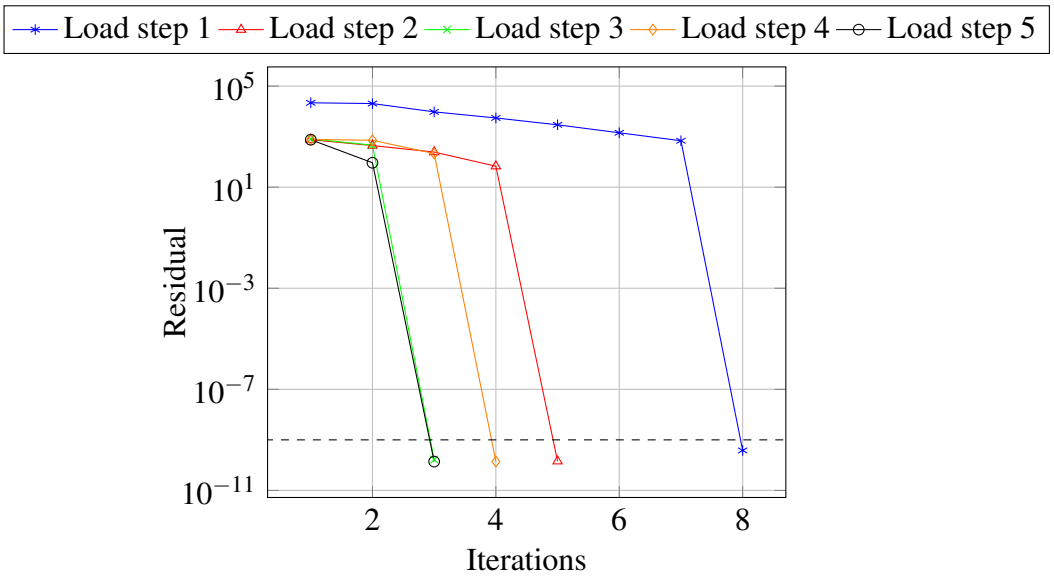

Figure 9.40 Bulk - Newton Method error evolution for IGABEM.

CPU time comparison

Similarly to the previous example, CPU time data presented in 9.26 shows that IGABEM has higher computational cost. Times for the Newton method iterations and for the entire problem are presented.

For this problem BEM was again faster and the ratio between BEM and IGABEM ranged from 33.05% for 21 node-pairs to 47.71% for 101 node-pairs. BEM and IGABEM codes took only 7.51 and 15.75 seconds, respectively, for running the entire problem.

Table 9.26 Bulk - CPU time comparison.

	Newton Method		Entire problem	
Node pairs	**BEM**	**IGABEM**	**BEM**	**IGABEM**
21	0.0635	2.9879	2.5296	7.6540
41	0.1614	3.1440	3.6625	8.2275
61	0.3188	3.5693	4.6125	10.4082
81	0.5772	3.9489	5.6883	11.9495
101	1.1958	4.8743	7.5147	15.7519

9.4 Fatigue life estimation

Parts of this section are reproductions of the research paper ***Numerical frameworks for fretting fatigue life analysis: Modeling, validation and experimental comparison*** [120]. [3]

Life evaluations results showing numerical estimation, N_{est}, versus experimental life, N_{exp}, are plotted in a log-log form and using factors, m, equal to 1, 2 and 4, as seen in Fig. 9.41. Its is important to emphasize that the reference line (m=1) is built from multiple data entries from experimental tests. Results are shown for life estimations using L_{eq}, L_{σ} and L_{τ}.

Overall, the results from the Titanium models have shown a higher accuracy. This is probably due to higher stiffness and the slightly lower friction coefficient, which leads to a more stable contact zone (higher normal pressure and lower friction force). The NTN-BEM and NTS-FEM results are almost identical in most scenarios, while the STS-FEM is better and the DMT-FEM is the best. Nevertheless, by employing L_{eq} all results falls precisely into the factor 1 reference line. In fact, the difference for the predictions of the aluminium life is so small that they become indistinguishable. For the Titanium, life estimations with NTN-BEM and NTS-FEM models are slightly higher (3.21% and 5.98%).

All numerical simulations have been carried-out in the same Workstation (02 Intel® Xeon® E5-2630 v3 with 8Cores at 3.2 GHz and 20Mb cache; and 196GB of available RAM). Herein, such a high-capacity computer is employed to make sure that a simulation would not consume all processing power available (bottleneck). It is important to emphasize that each framework can be run in a computer with significantly lower specifications.

The costs in terms of processor usage, RAM usage and computation time are listed in Table 9.27. The average processor usage, average memory bandwidth and computation time of a given simulation are retrieved from the resource monitor of the operating system using the system registry. To ensure a

[3] **© 2022 Elsevier Ltd. Reproduced with non-commercial purposes.**

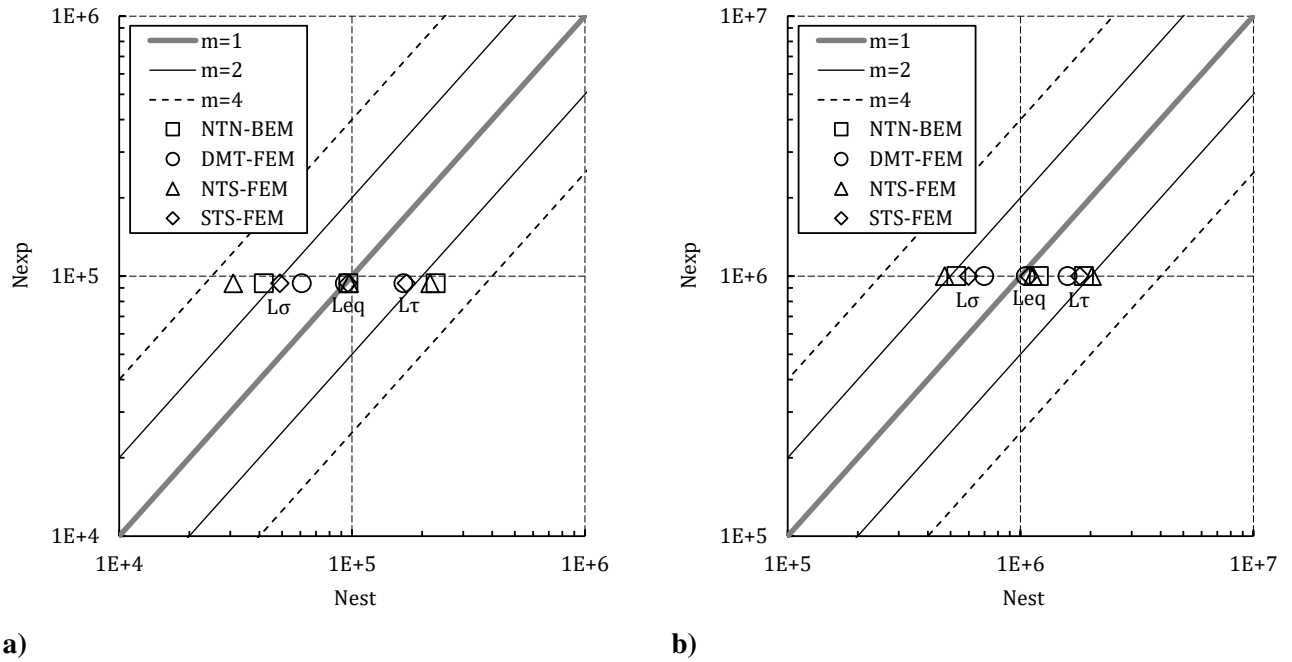

Figure 9.41 Life predictions and comparison to experimental data: a) Aluminium; b) Titanium.

stable and uniform computational environment, all background processes are ended before the start of a simulation. Moreover, each simulation is run individually and only the resources consumed in their processing (.exe) are measured. The steps of construction of the stress load history, identification of the critical plane, computation of τ_a, and the maximum normal stress, $\sigma_{n,max}$, and life estimation are carried-out separately using a MATLAB code and they require a similar cost for all frameworks: in average, 276s of computing time, using 15.2% processor capacity and 406MB of RAM.

The materials have shown no significant influence on the performance results. Nevertheless, a comparison of the frameworks show drastic differences. For instance, the NTN-BEM framework shows

Table 9.27 Performance parameters for each framework and material configuration.

Framework	Parameter	Al7050-T7451	Ti-6Al-4V
NTN-BEM	Processor usage (%)	13.3	14.1
	RAM usage (MB)	773.3	833.5
	Computation time (s)	178.0	177.0
NTS-FEM	Processor usage (%)	25.7	24.3
	RAM usage (MB)	334.2	328.7
	Computation time (s)	131.0	127.0
STS-FEM	Processor usage (%)	23.7	24.8
	RAM usage (MB)	341.7	346.0
	Computation time (s)	133	131
DMT-FEM	Processor usage (%)	32.6	34.1
	RAM usage (MB)	501.3	509.7
	Computation time (s)	128.0	126.0

the lowest processor usage, but the highest RAM usage. For that matter, they will be used as reference. The NTS and STS frameworks show a similar performance. They both require a processor usage of two times that of the NTN-BEM, approximately 51% of the RAM usage and a 26% less time. The DMT-FEM method shows the highest processor usage (+42%), but the lowest time (-61%) while requiring 37% of the RAM used by the NTN-BEM. When using a computer powerful enough, most users neglect the processing cost as long its lower than what is available. In fact, the highest level of processor usage observed in this study is close to one-third of the total capacity available. However, when compared, the NTN-BEM shows a process usage less than half (14.1%) of the DMT-FEM (34.1%). This means that one could run a numerical model with a much more refined mesh using the NTN-BEM while achieving a better representation of the problem and maintaining a lower comparative cost. Nevertheless, the implementation of NTN-BEM in MATLAB required considerably more RAM which can become much worse when using a more refined mesh.

10 Conclusion and final remarks

This work presented an isogeometric formulation for modelling elasticity and contact problems in two-dimensional domains. They were also compared to analytical and BEM solutions. Furthermore, for fretting fatigue life prediction, boundary elements results were compared with finite elements, where their stress histories were used as an input for the Fatemi-Socie failure criterion.

Isogeometric analysis allows more accurate computation of stress and strain than standard BEM. Using NURBS instead of polynomials as a basis for approximation of geometry and unknown fields presents advantages such as higher results accuracy and less time invested by engineers due to a simplification or even elimination of meshing.

Despite being harder to implement, IGABEM can be adapted to regular BEM codes if Bézier decomposition is used. Bézier decomposition is achieved by inserting repeated knots in the knot vector until they reach a multiplicity equal to the curve's degree.

The examples make clear that the proposed approach is more accurate when compared to quadratic elements, even with a coarser mesh. For the pressurised cylinder, IGABEM had a smaller error than BEM considering the same of DOFs. Radial displacements errors u_r were 3 times smaller in IGABEM considering the coarsest mesh, whereas 33 times with the finest one. When it comes to σ_θ error, IGABEM was 89 times more accurate with the coarsest mesh.

The proposed method also showed good agreement on the infinite plate with a hole and on the beam. BEM presented a good accuracy as well, as seen on the figures comparing numerical results and analytical results. In these examples, it is noticeable that the isogeometric method can use coarser meshes and still perform well.

Section 9.3 showed somepresented several contact problems, starting with a cylinder to cylinder contact. This model had normal and tangential loads applied as depicted in 9.23. BEM and IGABEM behaved similarly for this case, with the latter being more accurate in terms of contact peak pressure using 21 node pairs (4.104% versus 0.534% error). IGABEM was also closer to the analytical solutions

for contact half-width in every scenario (from 21 to 101 node pairs).

A second contact problem was modelled as a specimen under a fretting rig configuration. BEM was again faster to compute than IGABEM in this case, but they used 29 and 23 iterations for convergence, respectively. The isogeometric approach was more accurate in terms of contact peak-pressure and contact half-width. In some cases, BEM had a slighter better t_x agreement with analytical solutions. This happened because NURBS used in IGABEM are smooth and presented some difficulties in representing sharp edges.

Section 9.4 presented fatigue life estimation using the stress history obtained from different methods, namely NTN-BEM, NTS-FEM, STS-FEM, and DMT-FEM. After obtaining the stress history using these frameworks, a code was used to determine the shear stress amplitude and the maximum normal stress of aluminium and titanium specimens. BEM was the most affordable method in terms of processor usage (13.7% on average), whereas NTS-FEM used 25%, STS-FEM used 24.3%, and DMT-FEM, 33.4%. RAM usage, on the other hand, was costlier in BEM. It needed 803.4 Mb on average, against 331.5, 343.9, and 505.5 Mb for NTS-FEM, STS-FEM, and DMT-FEM, respectively. All methods presented a good representation of normal, shear, and bulk stress. Furthermore, life estimation using a calibrated L-N curve showed good agreement with experimental data, as all N_{est} were within $m = 4$ error band and most were within $m = 2$. Results using an equivalent critical distance, L_{eq}, have demonstrated that a precise estimation can be obtained.

10.1 Recommendations for future work

Some alternatives for future work based on this thesis arise, such as studying enriched formulations or knot repetition on contact edges. These could increase even further the method's accuracy, as some sharp edges were difficult to obtain using NURBS. Another possible continuation is to model anisotropic materials, as some components are cast as a single-crystal, and they are anisotropic. Expanding the code to model three-dimensional problems is also a suggestion, as the isogeometric approach has the advantage of linking CAD and analysis. 3D models are more complex and demand a considerable amount of time for meshing and remeshing. Therefore, it would be a significant contribution. Furthermore, adding a surface-to-surface or dual mortar method would be a great contribution, as it would provide more accuracy for more complex problems.

References

[1] M. P. SZOLWINSKI and T. N. FARRIS. “Mechanics of fretting fatigue crack formation”. In: *Wear* 198.1-2 (1996), pp. 93–107. DOI: 10.1016/0043-1648(96)06937-2.

[2] J. A. ARAÚJO and D. NOWELL. “Analysis of pad size effects in fretting fatigue using short crack arrest methodologies”. In: *International Journal of Fatigue* 21.9 (1999), pp. 947–956. DOI: 10.1016/S0142-1123(99)00077-8.

[3] D. ZHANG, K. CHEN, X. JIA, D. WANG, S. WANG, Y. LUO and S. GE. “Bending fatigue behaviour of bearing ropes working around pulleys of different materials”. In: *Engineering Failure Analysis* 33 (Oct. 2013), pp. 37–47. DOI: 10.1016/j.engfailanal.2013.04.018.

[4] J. ZHANG, D. WANG, D. ZHANG, S. GE and D. WANG. “Dynamic torsional characteristics of mine hoisting rope and its internal spiral components”. In: *Tribology International* 109 (May 2017), pp. 182–191. DOI: 10.1016/j.triboint.2016.12.037.

[5] K. KUMAR, D. GOYAL and S. S. BANWAIT. “Effect of Key Parameters on Fretting Behaviour of Wire Rope: A Review”. In: *Archives of Computational Methods in Engineering* 27.2 (Feb. 2019), pp. 549–561. DOI: 10.1007/s11831-019-09326-y.

[6] R. OSKOUEI and R. IBRAHIM. “Improving fretting fatigue behaviour of Al 7075-T6 bolted plates using electroless Ni–P coatings”. In: *International Journal of Fatigue* 44 (Nov. 2012), pp. 157–167. DOI: 10.1016/j.ijfatigue.2012.05.003.

[7] D. LI, D. BOTTO, C. XU and M. GOLA. “Fretting wear of bolted joint interfaces”. In: *Wear* 458-459 (Oct. 2020), p. 203411. DOI: 10.1016/j.wear.2020.203411.

[8] C. WANG, C. LI, Y. LING and M. A. WAHAB. “Investigation on fretting fatigue crack initiation in heterogenous materials using a hybrid of multiscale homogenization and direct

numerical simulation". In: *Tribology International* 169 (May 2022), p. 107470. DOI: 10.1016/j.triboint.2022.107470.

[9] C. RUIZ, P. H. B. BODDINGTON and K. C. CHEN. "An investigation of fatigue and fretting in a dovetail joint". In: *Experimental Mechanics* 24.3 (1984), pp. 208–217. DOI: 10.1007/BF02323167.

[10] J.-J. CHEN, L. LIU, S.-X. LI, S.-R. YU and Y.-N. HE. "Experimental and numerical investigation on crack initiation of fretting fatigue of dovetail". In: *Fatigue &amp Fracture of Engineering Materials &amp Structures* 41.6 (Feb. 2018), pp. 1426–1436. DOI: 10.1111/ffe.12787.

[11] B. YANG, J. HUO, Q. GAO and R. REN. "Research on factors affecting fretting fatigue life of high-temperature dovetail tenon". In: *Fatigue &amp Fracture of Engineering Materials &amp Structures* 45.4 (Jan. 2022), pp. 1126–1144. DOI: 10.1111/ffe.13654.

[12] Y. WANG, L. WU, S. LIU, M. LI and Y. CUI. "Fretting fatigue optimization of piston skirt top surface of marine diesel engine". In: *PROCEEDINGS OF THE INSTITUTION OF MECHANICAL ENGINEERS PART C-JOURNAL OF MECHANICAL ENGINEERING SCIENCE* 233.4 (2019), pp. 1453–1469. DOI: 10.1177/0954406218771723.

[13] Y. WANG, L. WU, S. LIU, M. LI, X. MENG and Y. CUI. "Numerical Study on Fretting Wear of Mating Surface Between Piston Crown and Skirt in Heavy Duty Diesel Engine". In: *Journal of Engineering for Gas Turbines and Power* 141.8 (Apr. 2019). DOI: 10.1115/1.4043274.

[14] M. AZADI and M. S. A. PARAST. "Data analysis of high-cycle fatigue testing on piston aluminum-silicon alloys under various conditions: Wear, lubrication, corrosion, nano-particles, heat-treating, and stress". In: *Data in Brief* 41 (Apr. 2022), p. 107984. DOI: 10.1016/j.dib.2022.107984.

[15] C. R. AZEVEDO, A. M. HENRIQUES, A. R. PULINO FILHO, J. L. FERREIRA and J. A. ARAÚJO. "Fretting fatigue in overhead conductors: Rig design and failure analysis of a Grosbeak aluminium cable steel reinforced conductor". In: *Engineering Failure Analysis* 16.1 (2009), pp. 136–151. DOI: 10.1016/j.engfailanal.2008.01.003.

[16] E. R. COSTA, J. A. ARAÚJO, L. A. C. M. VELOSO, C. R. M. SILVA and J. L. A. FERREIRA. "Development of controlled heating for fatigue test in overhead conductors at high temperature". In: *Journal of the Brazilian Society of Mechanical Sciences and Engineering* 42.7 (July 2020). DOI: 10.1007/s40430-020-02466-4.

[17] A. OMRANI, S. LANGLOIS, P. V. DYKE, S. LALONDE, S. S. KARGANROUDI and L. DIENG. "Fretting fatigue life assessment of overhead conductors using a clamp/conductor numerical model and biaxial fretting fatigue tests on individual wires". In: *Fatigue &amp Fracture of Engineering Materials &amp Structures* 44.6 (Mar. 2021), pp. 1498–1514. DOI: 10.1111/ffe.13444.

[18] E. C. B. CÃMARA, R. B. KALOMBO, J. L. FERREIRA, J. A. ARAÚJO and R. C. S. F. JÚNIOR. "Estimating fatigue behavior of a family of aluminum overhead conductors using ANNs". In: *Fatigue &amp Fracture of Engineering Materials &amp Structures* 44.4 (Jan. 2021), pp. 983–996. DOI: 10.1111/ffe.13408.

[19] M. ZHU, Z. CAI, W. LI, H. YU and Z. ZHOU. "Fretting in prosthetic devices related to human body". In: *Tribology International* 42.9 (Sept. 2009), pp. 1360–1364. DOI: 10.1016/j.triboint.2009.04.007.

[20] S. MARTELLI, F. TADDEI, E. SCHILEO, L. CRISTOFOLINI, N. RUSHTON and M. VICECONTI. "Biomechanical robustness of a new proximal epiphyseal hip replacement to patient variability and surgical uncertainties: A FE study". In: *Medical Engineering &amp Physics* 34.2 (Mar. 2012), pp. 161–171. DOI: 10.1016/j.medengphy.2011.07.006.

[21] R. ENGLISH, A. ASHKANFAR and G. ROTHWELL. "A computational approach to fretting wear prediction at the head–stem taper junction of total hip replacements". In: *Wear* 338-339 (Sept. 2015), pp. 210–220. DOI: 10.1016/j.wear.2015.06.016.

[22] A. FADEL, D. ROSA, L. MURÇA, J. FEREIRA and J. ARAÚJO. "Effect of high mean tensile stress on the fretting fatigue life of an Ibis steel reinforced aluminium conductor". In: *International Journal of Fatigue* 42 (Sept. 2012), pp. 24–34. DOI: 10.1016/j.ijfatigue.2011.03.007.

[23] J. BUREK, R. BABIARZ, J. BUK, P. SUŁKOWICZ and K. KRUPA. “The Accuracy of Finishing WEDM of Inconel 718 Turbine Disc Fir Tree Slots”. In: *Materials* 14.3 (Jan. 2021), p. 562. DOI: 10.3390/ma14030562.

[24] S. NABOULSI and S. MALL. “Fretting fatigue crack initiation behavior using process volume approach and finite element analysis”. In: *Tribology International* 36.2 (2003), pp. 121–131. DOI: 10.1016/S0301-679X(02)00139-1.

[25] A. WÖHLER. “Versuche über die Festigkeit der Eisenbahnwagenachsen”. In: *Zeitschrift für Bauwesen* 10.1860 (1860), pp. 160–161.

[26] A. WÖHLER. *Über die festigkeitsversuche mit eisen und stahl*. Ernst and Korn, 1870.

[27] E. M. EDEN, W. N. ROSE and P. L. CUNNINGHAM. “The Endurance of Metals: Experiments on Rotating Beams at University College, London”. In: *Proceedings of the Institution of Mechanical Engineers* 81.1 (June 1911), pp. 839–974. DOI: 10.1243/pime_proc_1911_081_017_02.

[28] G. A. TOMLINSON. “The rusting of steel surfaces in contact”. In: *Proceedings of the Royal Society of London. Series A, Containing Papers of a Mathematical and Physical Character* 115.771 (July 1927), pp. 472–483. DOI: 10.1098/rspa.1927.0104.

[29] E. J. WARLOW-DAVIES. “Fretting Corrosion and Fatigue Strength: Brief Results of Preliminary Experiments”. In: *Proceedings of the Institution of Mechanical Engineers* 146.1 (June 1941), pp. 32–38. DOI: 10.1243/pime_proc_1941_146_012_02.

[30] J. MCDOWELL, H. UHLIG, W. TIERNEY, A. MCCLELLAN and O. J. HORGER. “FRETTING CORROSION”. In: *Anti-Corrosion Methods and Materials* 1.7 (July 1954), pp. 247–252. DOI: 10.1108/eb018966.

[31] A. J. FENNER and J. E. FIELD. “La fatigue dans les conditions de frottement”. In: *Revue de Métallurgie* 55.5 (May 1958), pp. 475–485. DOI: 10.1051/metal/195855050475.

[32] K. L. JOHNSON. “Surface interaction between elastically loaded bodies under tangential forces”. In: *Proceedings of the Royal Society of London. Series A. Mathematical and Physical Sciences* 230.1183 (July 1955), pp. 531–548. DOI: 10.1098/rspa.1955.0149.

[33] C. CATTANEO. “Sul contatto di due corpi elastici: distribuzione locale degli sforzi. I, II, III”. In: *Atti della Accademia Nazionale dei Lincei, Rendiconti, VI. Serie* 27 (Jan. 1938).

[34] R. MINDLIN. “Compliance of Elastic Bodies in Contact”. In: *Journal of Applied Mechanics* 16 (Jan. 1949), pp. 259–268. DOI: 10.1007/978-1-4613-8865-4_24.

[35] R. B. WATERHOUSE. *Fretting corrosion*. English. Oxford; New York: Pergamon Press, 1972.

[36] R. B. WATERHOUSE. *Fretting fatigue*. Applied Science Publ., 1981.

[37] D. HILLS and D. NOWELL. *Mechanics of Fretting Fatigue*. 1994.

[38] D. HILLS, D. NOWELL and A. SACKFIELD. *Mechanics of Elastic Contacts*. 1993, p. 488. DOI: 10.1016/b978-0-7506-0540-3.50016-7.

[39] J. A. ARAÚJO. “On the Initiation and Arrest of the Fretting Fatigue Cracks”. PhD thesis. University of Oxford, 2000.

[40] C. PETIOT, L. VINCENT, K. D. VAN, N. MAOUCHE, J. FOULQUIER and B. JOURNET. “An analysis of fretting-fatigue failure combined with numerical calculations to predict crack nucleation”. In: *Wear* 181-183 (Feb. 1995), pp. 101–111. DOI: 10.1016/0043-1648(94)07026-1.

[41] V. K. DANG. “Sur la résistance à la fatigue des métaux”. In: (1971).

[42] Y. LIU. *Fast Multipole Boundary Element Method: Theory and Applications in Engineering*. Cambridge University Press, 2009, p. 255.

[43] Z. CHEN, H. XIAO, X. YANG and C. SU. “Taylor series multipole boundary element-mathematical programming method for 3D multi-bodies elastic contact problems”. In: December 2009 (2010), pp. 135–173. DOI: 10.1002/nme.

[44] T. TRAUB. *A Kernel Interpolation Based Fast Multipole Method for Elastodynamic Problems*. 2016.

[45] S. LI, J. TREVELYAN, W. ZHANG and D. WANG. “Accelerating isogeometric boundary element analysis for 3-dimensional elastostatics problems through black-box fast multipole method with proper generalized decomposition”. In: *International Journal for Numerical Methods in Engineering* 114.9 (2018), pp. 975–998. DOI: 10.1002/nme.5773.

[46] M. BEBENDORF. “Numerische Mathematik Approximation of boundary element matrices”. In: *Numerische Mathematik* 86 (2000), pp. 565–589. DOI: 10.1007/PL00005410.

[47] V. MALLARDO, M. ALIABADI, A. BRANCATI and V. MARANT. “An accelerated BEM for simulation of noise control in the aircraft cabin”. In: *Aerospace Science and Technology* 23.1 (Dec. 2012), pp. 418–428. DOI: 10.1016/j.ast.2011.10.001.

[48] L. S. CAMPOS, E. L. ALBUQUERQUE and L. C. WROBEL. “An ACA accelerated isogeometric boundary element analysis of potential problems with non-uniform boundary conditions”. In: *Engineering Analysis with Boundary Elements* 80.February (2017), pp. 108–115. DOI: 10.1016/j.enganabound.2017.04.004.

[49] T. V. GORTSAS, S. V. TSINOPOULOS, D. RODOPOULOS and D. POLYZOS. “Strain gradient elasticity and size effects in the bending of fiber composite plates”. In: *International Journal of Solids and Structures* 143 (June 2018), pp. 103–112. DOI: 10.1016/j.ijsolstr.2018.02.035.

[50] Z. YAO, X. ZHENG, H. YUAN and J. FENG. “Research progress of high-performance BEM and investigation on convergence of GMRES in local stress analysis of slender real thin-plate beams”. In: *Engineering Computations* 36.8 (Oct. 2019), pp. 2530–2556. DOI: 10.1108/ec-10-2018-0477.

[51] G. GOMES and A. C. MIRANDA. “Analysis of crack growth problems using the object-oriented program bemcracker2D”. In: *Frattura ed Integrita Strutturale* 12.45 (2018), pp. 67–85. DOI: 10.3221/IGF-ESIS.45.06.

[52] T. A. OLIVEIRA, G. GOMES and F. EVANGELISTA. “Multiscale aircraft fuselage fatigue analysis by the dual boundary element method”. In: *Engineering Analysis with Boundary Elements* 104.March (2019), pp. 107–119. DOI: 10.1016/j.enganabound.2019.03.032.

[53] B. GILVEY, J. TREVELYAN and G. HATTORI. “Singular enrichment functions for Helmholtz scattering at corner locations using the boundary element method”. In: *International Journal for Numerical Methods in Engineering* 121.3 (2020), pp. 519–533. DOI: 10.1002/nme.6232.

[54] F. LIANG and Z. SONG. “BEM analysis of the interaction factor for vertically loaded dissimilar piles in saturated poroelastic soil”. In: *Computers and Geotechnics* 62 (2014), pp. 223–231. DOI: 10.1016/j.compgeo.2014.07.016.

[55] S. M. ALEYNIKOV. *Spatial contact problems in geotechnics*. Springer, 2010.

[56] T. J. R. HUGHES, J. COTTRELL and Y. BAZILEVS. “Isogeometric analysis: CAD, finite elements, NURBS, exact geometry and mesh refinement”. In: *Computer Methods in Applied Mechanics and Engineering* 194.39-41 (Oct. 2005), pp. 4135–4195. DOI: 10.1016/J.CMA.2004.10.008.

[57] J. A. COTTRELL, T. J. HUGHES and Y. BAZILEVS. *Isogeometric analysis: toward integration of CAD and FEA*. John Wiley & Sons, 2009.

[58] R. N. SIMPSON, S. P. BORDAS, J. TREVELYAN and T. RABCZUK. “A two-dimensional Isogeometric Boundary Element Method for elastostatic analysis”. In: *Computer Methods in Applied Mechanics and Engineering* 209-212 (2012), pp. 87–100. DOI: 10.1016/j.cma.2011.08.008.

[59] R. N. SIMPSON, S. P. BORDAS, H. LIAN and J. TREVELYAN. “An isogeometric boundary element method for elastostatic analysis: 2D implementation aspects”. In: *Computers and Structures* 118 (2013), pp. 2–12. DOI: 10.1016/j.compstruc.2012.12.021.

[60] J. J. S. P. CABRAL, L. C. WROBEL and C. A. BREBBIA. “A BEM formulation using B-splines: I-uniform blending functions”. In: *Engineering Analysis with Boundary Elements* 7.3 (1990), pp. 136–144. DOI: 10.1016/0955-7997(90)90037-A.

[61] J. J. S. P. CABRAL, L. C. WROBEL and C. A. BREBBIA. “A BEM formulation using B-splines: II-multiple knots and non-uniform blending functions”. In: *Engineering Analysis with Boundary Elements* 8.1 (1991), pp. 51–55. DOI: 10.1016/0955-7997(91)90036-S.

[62] I. TEMIZER, P. WRIGGERS and T. J. R. HUGHES. “Contact treatment in isogeometric analysis with NURBS”. In: *Computer Methods in Applied Mechanics and Engineering* 200.9-12 (2011), pp. 1100–1112. DOI: 10.1016/j.cma.2010.11.020.

[63] I. TEMIZER, P. WRIGGERS and T. J. R. HUGHES. “Three-dimensional mortar-based frictional contact treatment in isogeometric analysis with NURBS”. In: *Computer Methods in Applied Mechanics and Engineering* 209-212 (2012), pp. 115–128. DOI: 10.1016/j.cma.2011.10.014.

[64] J. LU. “Isogeometric contact analysis: Geometric basis and formulation for frictionless contact”. In: *Computer Methods in Applied Mechanics and Engineering* 200.5-8 (2011), pp. 726–741. DOI: 10.1016/j.cma.2010.10.001.

[65] J. KIENDL, K. U. BLETZINGER, J. LINHARD and R. WÜCHNER. “Isogeometric shell analysis with Kirchhoff-Love elements”. In: *Computer Methods in Applied Mechanics and Engineering* 198.49-52 (2009), pp. 3902–3914. DOI: 10.1016/j.cma.2009.08.013.

[66] J. KIENDL, Y. BAZILEVS, M. C. HSU, R. WÜCHNER and K. U. BLETZINGER. “The bending strip method for isogeometric analysis of Kirchhoff-Love shell structures comprised of multiple patches”. In: *Computer Methods in Applied Mechanics and Engineering* 199.37-40 (2010), pp. 2403–2416. DOI: 10.1016/j.cma.2010.03.029.

[67] D. J. BENSON, S. HARTMANN, Y. BAZILEVS, M. C. HSU and T. J. HUGHES. “Blended isogeometric shells”. In: *Computer Methods in Applied Mechanics and Engineering* 255.November (2013), pp. 133–146. DOI: 10.1016/j.cma.2012.11.020.

[68] X. DENG, A. KOROBENKO, J. YAN and Y. BAZILEVS. “Isogeometric analysis of continuum damage in rotation-free composite shells”. In: *Computer Methods in Applied Mechanics and Engineering* 284 (2015), pp. 349–372. DOI: 10.1016/j.cma.2014.09.015.

[69] Y. SUN, J. TREVELYAN, G. HATTORI and C. LU. “Discontinuous isogeometric boundary element (IGABEM) formulations in 3D automotive acoustics”. In: *Engineering Analysis with Boundary Elements* 105.September 2018 (2019), pp. 303–311. DOI: 10.1016/j.enganabound.2019.04.011.

[70] F. L. SUN, C. Y. DONG, Y. H. WU and Y. P. GONG. “Fast direct isogeometric boundary element method for 3D potential problems based on HODLR matrix”. In: *Applied Mathematics and Computation* 359 (2019), pp. 17–33. DOI: 10.1016/j.amc.2019.04.030.

[71] S. H. SUN, T. T. YU, T. T. NGUYEN, E. ATROSHCHENKO and T. Q. BUI. “Structural shape optimization by IGABEM and particle swarm optimization algorithm”. In: *Engineering Analysis with Boundary Elements* 88.May 2017 (2018), pp. 26–40. DOI: 10.1016/j.enganabound.2017.12.007.

[72] H. L. OLIVEIRA, H. de CASTRO E ANDRADE and E. D. LEONEL. “An isogeometric boundary element approach for topology optimization using the level set method”. In: *Applied Mathematical Modelling* 84 (Aug. 2020), pp. 536–553. DOI: 10.1016/j.apm.2020.03.047.

[73] A. R. NETO and E. D. LEONEL. “Nonlinear IGABEM formulations for the mechanical modelling of 3D reinforced structures”. In: *Applied Mathematical Modelling* 102 (Feb. 2022), pp. 62–100. DOI: 10.1016/j.apm.2021.09.006.

[74] F. L. SUN, C. Y. DONG and H. S. YANG. “Isogeometric boundary element method for crack propagation based on Bézier extraction of NURBS”. In: *Engineering Analysis with Boundary Elements* 99.September 2018 (2019), pp. 76–88. DOI: 10.1016/j.enganabound.2018.11.010.

[75] R. P. REED, J. H. SMITH and B. W. CHRIST. *The economic effects of fracture in the United States*. Tech. rep. 1983. DOI: 10.6028/nbs.sp.647p1.

[76] S. NABOULSI and J. CALCATERRA. “Fretting fatigue investigation of dovetail”. In: *11th International Conference on Fracture 2005, ICF11* 4 (2005), pp. 2746–2751.

[77] T. M. O. S. HORTÊNCIO. “Ensaios de Fadiga sob Condições de Fretting com o cabo CAA 397,5 MCM - IBIS.” In: (2009).

[78] S. V. C. GUTIÉRREZ, J. C. J. CORREA, A. DOMINGUEZ-GONZALEZ and R. A. GÓMEZ-LOENZO. “An Application of Isogeometric Analysis and Boundary Integral Element Method for Solving Nonlinear Contact Problems”. In: *Applied Sciences* 10.7 (Mar. 2020), p. 2345. DOI: 10.3390/app10072345.

[79] C. SOMIGLIANA. “Sopra l’equilibrio di un corpo elastico isotropo”. In: *Il Nuovo Cimento* 17 (1885), pp. 140–148.

[80] E. BETTI. “Teoria dell elasticita”. In: *Nuovo cimento* 11 (1872), pp. 7–10.

[81] N. I. MUSKHELISHVILI. *Some Basic Problems of the Mathematical Theory of Elasticity*. Noordhoff, 1953.

[82] T. A. CRUSE. "Numerical solutions in three dimensional elastostatics". In: *International Journal of Solids and Structures* 5.12 (1969), pp. 1259–1274. DOI: 10.1016/0020-7683(69)90071-7.

[83] F. J. RIZZO. "An integral equation approach to boundary value problems of classical elastostatics". In: *Quarterly of applied mathematics* 25.1 (1967), pp. 83–95.

[84] T. A. CRUSE and J. L. SWEDLOW. *Interactive program for analysis and design problems in advanced composite technology*. Tech. rep. Carnegie-Mellon University, 1971.

[85] P. C. RICCARDELLA. "An implementation of the boundary-integral technique for planar problems of elasticity and elasto-plasticity". PhD thesis. Carnegie-Mellon University, 1973.

[86] J. C. LACHAT. "A further development of the boundary integral technique for elastostatics". PhD thesis. University of Southampton, 1975.

[87] J. C. LACHAT and J. O. WATSON. "Effective numerical treatment of boundary integral equations: A formulation for three-dimensional elastostatics". In: *International Journal for Numerical Methods in Engineering1* 10 (1976), pp. 991–1005.

[88] J. T. KATSIKADELIS. *The Boundary Element Method for Engineers and Scientists*. Second Edi. 2016, p. 447.

[89] I. M. HUTCHINGS. "Leonardo da Vinci's studies of friction". In: *Wear* 360-361 (2016), pp. 51–66. DOI: 10.1016/j.wear.2016.04.019.

[90] G. AMONTONS. "De la résistance causée dans les machines, tant par les frottemens des parties qui les composent, que par la roideur des Cordes qu'on y employe, et la manière de calculer l'un et l'autre." In: *Mém. Math. Phys. Hist. Acad. R. Sci* (1699), pp. 206–227.

[91] C. COULOMB. "Théorie des machines simples, en ayant regard au frottement de leurs parties et à la roideur des cordages." In: *Mém. Math. Phys. Hist. Acad. R. Sci* (1779), pp. 161–331.

[92] H. HERTZ. "H. Hertz, Über die Berührung fester elastischer Körper, Journal für die reine und angewandte Mathematik 92, 156-171 (1881)". In: *Journal für die reine und angewandte Mathematik* 171.92 (1881), pp. 156–171.

[93] K. L. JOHNSON. *Contact Mechanics*. 1985, p. 452.

[94] URL: https://www.northernarchitecture.us/steel-construction/info-eey.html.

[95] K. W. MAN, M. H. ALIABADI and D. P. ROOKE. "Bem frictional contact analysis: Load incremental technique". In: *Computers and Structures* 47.6 (1993), pp. 893–905. DOI: 10.1016/0045-7949(93)90294-N.

[96] K. W. MAN, M. H. ALIABADI and D. P. ROOKE. "BEM frictional contact analysis: Modelling considerations". In: *Engineering Analysis with Boundary Elements* (1993). DOI: 10.1016/0955-7997(93)90081-U.

[97] B. M. CAVALCANTE, M. H. SHATERZADEH-YAZDI, P. SOLLERO, E. L. ALBUQUERQUE and T. DOCA. "Analysis of a Cattaneo-Mindlin problem using the boundary element method". In: *Tribology International* 108.September 2016 (2017), pp. 194–201. DOI: 10.1016/j.triboint.2016.09.024.

[98] C. G. PANAGIOTOPOULOS, V. MANTIČ, I. G. GARCÍA and E. GRACIANI. "Boundary integral formulation of frictionless contact problems based on an energetic approach and its numerical implementation by the collocation BEM". In: *Frontiers in Built Environment* 4.November (2018), pp. 1–20. DOI: 10.3389/fbuil.2018.00056.

[99] G. K. SFANTOS and M. H. ALIABADI. "A boundary element sensitivity formulation for contact problems using the implicit differentiation method". In: *Engineering Analysis with Boundary Elements* 30.1 (2006), pp. 22–30. DOI: 10.1016/j.enganabound.2005.08.004.

[100] G. K. SFANTOS and M. H. ALIABADI. "Application of BEM and optimization technique to wear problems". In: *International Journal of Solids and Structures* 43.11-12 (2006), pp. 3626–3642. DOI: 10.1016/j.ijsolstr.2005.09.004.

[101] G. K. SFANTOS and M. H. ALIABADI. "Wear simulation using an incremental sliding Boundary Element Method". In: *Wear* 260.9-10 (2006), pp. 1119–1128. DOI: 10.1016/j.wear.2005.07.020.

[102] G. K. SFANTOS and M. H. ALIABADI. “A boundary element formulation for three-dimensional sliding wear simulation”. In: *Wear* 262.5-6 (2007), pp. 672–683. DOI: 10.1016/j.wear.2006.08.008.

[103] L. RODRÍGUEZ-TEMBLEQUE, R. ABASCAL and M. H. ALIABADI. “A boundary elements formulation for 3D fretting-wear problems”. In: *Engineering Analysis with Boundary Elements* 35.7 (2011), pp. 935–943. DOI: 10.1016/j.enganabound.2011.03.002.

[104] L. RODRÍGUEZ-TEMBLEQUE, R. ABASCAL and M. H. ALIABADI. “Anisotropic wear framework for 3D contact and rolling problems”. In: *Computer Methods in Applied Mechanics and Engineering* 241-244 (2012), pp. 1–19. DOI: 10.1016/j.cma.2012.05.025.

[105] A. A. FADEL. “Avaliação do Efeito de Tracionamento em Elevados Níveis de EDS Sobre a Reistência em Fadiga do Condutor IBIS (CAA 397,5 MCM)”. In: *Enm.Td-005/2010* (2010), p. 185.

[106] P. ALART and A. CURNIER. “A mixed formulation for frictional contact problems prone to Newton like solution methods”. In: *Computer Methods in Applied Mechanics and Engineering* 92.3 (1991), pp. 353–375. DOI: 10.1016/0045-7825(91)90022-X.

[107] J. WANG, H. XU, T. SU, Y. ZHANG, Z. GUO, H. MAO and Y. ZHANG. “Fretting fatigue experiment and analysis of AlSi9Cu2Mg alloy”. In: *Materials* 9.12 (2016), pp. 1–13. DOI: 10.3390/ma9120984.

[108] H. A. FADAG, S. MALL and V. K. JAIN. “A finite element analysis of fretting fatigue crack growth behavior in Ti-6Al-4V”. In: *Engineering Fracture Mechanics* 75.6 (2008), pp. 1384–1399. DOI: 10.1016/j.engfracmech.2007.07.003.

[109] N. E. FROST and C. E. PHILLIPS. “Studies in the formation and propagation of cracks in fatigue specimens”. In: 1956.

[110] G. R. IRWIN. “Analysis of stresses and strains near the end of a crack traversing a plate”. In: (1957).

[111] T. L. ANDERSON. *Fracture mechanics: fundamentals and applications*. CRC press, 2017.

[112] K. MILLS and J. R. DAVIS. *ASM Handbook, Volume 12-Fractography*. ASM International, 1987.

[113] C. A and S. A. “Multiaxial high-cycle fatigue criterion for hard metals”. In: *International Journal of Fatigue* 23.2 (2001), pp. 135–145. DOI: 10.1016/s0142-1123(00)00075-x.

[114] J. ARAÚJO, A. DANTAS, F. CASTRO, E. MAMIYA and J. FERREIRA. “On the characterization of the critical plane with a simple and fast alternative measure of the shear stress amplitude in multiaxial fatigue”. In: *International Journal of Fatigue* 33.8 (Aug. 2011), pp. 1092–1100. DOI: 10.1016/j.ijfatigue.2011.01.002.

[115] T. GAILLIEGUE. “Effects of phase angle between the fretting load and the bulk load on the life of the AL7050 T7451 and ASTM 743 CA6NM”. PhD thesis. Universidade de Brasilia, 2018.

[116] I. V. PAPADOPOULOS. “A new criterion of fatigue strength for out-of-phase bending and torsion of hard metals”. In: *International Journal of Fatigue* 16.6 (1994), pp. 377–384.

[117] A. BERNASCONI. “Efficient algorithms for calculation of shear stress amplitude and amplitude of the second invariant of the stress deviator in fatigue criteria applications”. In: *International journal of fatigue* 24.6 (2002), pp. 649–657.

[118] J. ARAÚJO, L. SUSMEL, M. PIRES and F. CASTRO. “A multiaxial stress-based critical distance methodology to estimate fretting fatigue life”. In: *Tribology International* 108 (Apr. 2017), pp. 2–6. DOI: 10.1016/j.triboint.2016.07.028.

[119] K. SMITH, T. TOPPER and P. WATSON. “A stress-strain function for the fatigue of metals (stress-strain function for metal fatigue including mean stress effect)”. In: 5 (Jan. 1970), pp. 767–778.

[120] T. DOCA, F. LOYOLA and E. ALBUQUERQUE. “Numerical frameworks for fretting fatigue life analysis: Modeling, validation and experimental comparison”. In: *Theoretical and Applied Fracture Mechanics* (July 2022), p. 103479. DOI: 10.1016/j.tafmec.2022.103479.

[121] A. FATEMI and D. F. SOCIE. “A CRITICAL PLANE APPROACH TO MULTIAXIAL FATIGUE DAMAGE INCLUDING OUT-OF-PHASE LOADING”. In: *Fatigue &amp Fracture of Engineering Materials and Structures* 11.3 (Mar. 1988), pp. 149–165. DOI: 10.1111/j.1460-2695.1988.tb01169.x.

[122] T. GAILLIEGUE, T. DOCA, J. A. ARAÚJO and J. L. FERREIRA. “Fretting life of the Al7050-T7451 under out-of-phase loads: Numerical and experimental analysis”. In: *Theoretical and Applied Fracture Mechanics* 106.December 2019 (2020), p. 102492. DOI: 10.1016/j.tafmec.2020.102492.

[123] B. FERRY, J. A. ARAÚJO, S. POMMIER and K. DEMMOU. “Life of a Ti–6Al–4V alloy under fretting fatigue: Study of new nonlocal parameters”. In: *Tribology International* 108 (Apr. 2017), pp. 23–31. DOI: 10.1016/j.triboint.2016.11.003.

[124] I. FREDHOLM. “Sur Une Classe D’Équations Fonctionnelles”. In: *Acta mathematica* 27 (1903), pp. 365–390.

[125] S. G. MIKHLIN. *Integral equations and their applications to certain problems in mechanics, mathematical physics and technology*. Pergamon, 1957.

[126] C. A. BREBBIA and J. DOMINGUEZ. “Boundary element methods for potential problems”. In: *Applied Mathematical Modelling* 1.7 (1977), pp. 372–378. DOI: 10.1016/0307-904X(77)90046-4.

[127] W. S. HALL. *The Boundary Element Method*. Springer Science & Business Media, 2012.

[128] M. H. ALIABADI. “The boundary element method. Volume 2: Applications in solids and structures (Aliabadi, M.H.)” In: *Bautechnik* 80.2 (2003), pp. 138–139. DOI: 10.1002/bate.200301300.

[129] C. A. BREBBIA and J. DOMINGUEZ. *Boundary elements: an introductory course*. WIT press, 1994.

[130] M. GUIGGIANI and P. CASALINI. “Direct Computation of Cauchy Principal Value”. In: *International Journal for Numerical Methods in Engineering* 24.9 (1987).

[131] L. PIEGL and W. TILLER. *The NURBS book*. 2nd. Springer-Verlag Berlin Heidelberg, 1997. DOI: 10.5860/choice.35-0952.

[132] G. BEER, B. MARUSSIG and C. DUENSER. *The Isogeometric Boundary Element Method*. Springer, 2019.

[133] M. J. BORDEN, M. A. SCOTT, J. A. EVANS and T. J. HUGHES. “Isogeometric finite element data structures based on Bézier extraction of NURBS”. In: *International Journal for Numerical Methods in Engineering* 87.1-5 (July 2011), pp. 15–47. DOI: 10.1002/nme.2968.

[134] M. A. SCOTT, M. J. BORDEN, C. V. VERHOOSEL, T. W. SEDERBERG and T. J. R. HUGHES. “Isogeometric finite element data structures based on Bézier extraction of T-splines”. In: *Int. J. Numer. Meth. Engng* 88 (2011), pp. 12–156. DOI: 10.1002/nme.

[135] J. C. TELLES. “A self-adaptive co-ordinate transformation for efficient numerical evaluation of general boundary element integrals”. In: *International Journal for Numerical Methods in Engineering* 24.5 (1987), pp. 959–973. DOI: 10.1002/nme.1620240509.

[136] M. GUIGGIANI and P. CASALINI. “elements”. In: 13.2 (1989), pp. 365–368.

[137] M. GUIGGIANI. “Formulation and numerical treatment of boundary integral equations with hypersingular kernels”. In: *Singular integrals in boundary element methods* January 1998 (1998).

[138] L. S. CAMPOS. “Método dos elementos de contorno isogeométricos acelerado pela aproximação cruzada adaptativa”. PhD thesis. Universidade de Brasília, 2016.

[139] Y. J. WANG and D. J. BENSON. “Multi-patch nonsingular isogeometric boundary element analysis in 3D”. In: *Computer Methods in Applied Mechanics and Engineering* 293 (2015), pp. 71–91. DOI: 10.1016/j.cma.2015.03.016.

[140] L. RODRÍGUEZ-TEMBLEQUE and R. ABASCAL. “A FEM-BEM fast methodology for 3D frictional contact problems”. In: *Computers and Structures* 88.15-16 (2010), pp. 924–937. DOI: 10.1016/j.compstruc.2010.04.010.

[141] L. RODRÍGUEZ-TEMBLEQUE, F. GARCÍA-SÁNCHEZ and A. SÁEZ. “Crack-face frictional contact modelling in cracked piezoelectric materials”. In: *Computational Mechanics* (2019). DOI: 10.1007/s00466-019-01743-x.

[142] L. RODRÍGUEZ-TEMBLEQUE. “FORMULACION NUMERICA DE LA INTERACCION MECANICA ENTRE SUPERFICIES DE SOLIDOS 3D”. PhD thesis. UNIVERSIDAD DE SEVILLA, 2009.

[143] T. S. OLIVEIRA and A. PORTELA. “Weak-form collocation – A local meshless method in linear elasticity”. In: *Engineering Analysis with Boundary Elements* 73.April (2016), pp. 144–160. DOI: 10.1016/j.enganabound.2016.09.010.

[144] F. M. LOYOLA, T. DOCA, L. S. CAMPOS, J. TREVELYAN and E. L. ALBUQUERQUE. “Analysis of 2D contact problems under cyclic loads using IGABEM with Bézier decomposition”. In: *Engineering Analysis with Boundary Elements* 139 (2022), pp. 246–263.